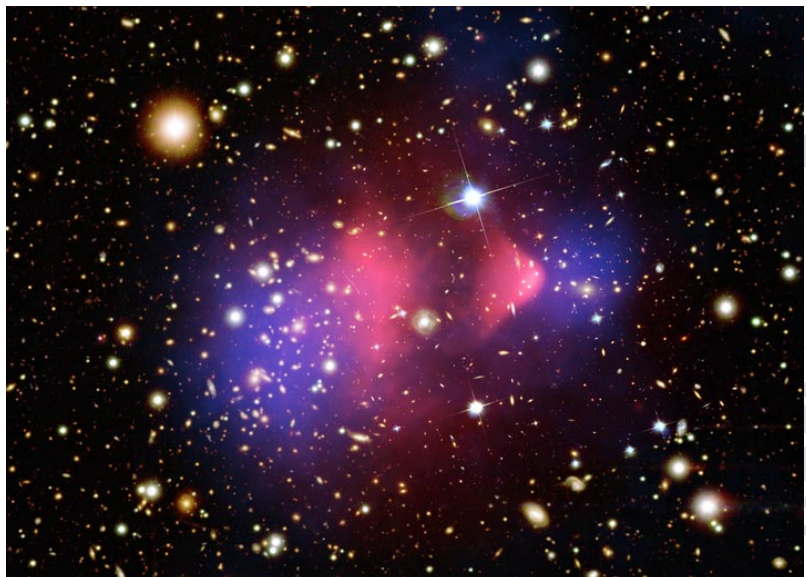


# GALAXY CLUSTER COSMOLOGY

Ph.D. Thesis in Astrophysics



**Sebastian Bocquet**

Munich, May 2015

Title page image: <http://chandra.harvard.edu/photo/2006/1e0657>  
Credit: X-ray: NASA/CXC/CfA/Markевич et al.; Optical: NASA/STScI; Magellan/U.Arizona/.Cowe et al.;  
Lensing Map: NASA/STScI; ESO WFI; Magellan/U.Arizona/Clowe et al.

# GALAXY CLUSTER COSMOLOGY

## Dissertation

at the Faculty of Physics  
of the Ludwig-Maximilians-Universität München

submitted by

**Sebastian Bocquet**

from Munich, Germany

Munich, May 2015

First evaluator: Prof. Dr. Joseph J. Mohr  
Second evaluator: Prof. Dr. Eiichiro Komatsu

Date of the oral exam: June 26, 2015

*In memoriam Dr. Basti Haag*



# Zusammenfassung

Galaxienhaufen (englisch galaxy cluster) sind einige der größten Objekte in unserem Universum. Sie bestehen aus einigen Dutzend bis hin zu Tausenden von Galaxien und wurden, wie ihr Name bereits nahelegt, zunächst als Überdichten in der projizierten Anzahldichte von Galaxien in den 1960er Jahren entdeckt (z.B. Abell 1958; Zwicky et al. 1968). Allerdings weiß man heute, dass Galaxien nur etwa 1% der Gesamtmasse eines Galaxienhaufens ausmachen. Intergalaktisches Gas macht mit etwa 9% der Gesamtmasse den Großteil gewöhnlicher Materie aus, und der Rest, also 90%, ist dunkle Materie. Diese drei Komponenten eines Galaxienhaufens können durch verschiedene Methoden beobachtet werden. Die Galaxien selbst werden optisch beobachtet, und das intergalaktische Gas anhand anderer, spezieller Methoden. Die dunkle Materie wiederum kann per Definition nicht direkt beobachtet werden. Allerdings bestimmen Messungen des schwachen Gravitationslinseneffekts die Gesamtmasse eines Galaxienhaufens, sodass auch die dunkle Materie untersucht werden kann.

Auf der Titelseite dieser Dissertation ist der berühmte “bullet cluster” abgebildet, dessen innere Struktur anhand der drei erwähnten Beobachtungsarten aufgelöst werden konnte: Der eigentliche Galaxienhaufen befindet sich in der linken Bildhälfte, in der auch viele rotverschobene Galaxien zu erkennen sind. Rechts davon befindet sich der “bullet”, ein kleinerer Galaxienhaufen, der den größeren bereits von links nach rechts durchquert hat. Die blaue Farbe zeigt die anhand des schwachen Gravitationslinseneffekts gemessene Verteilung der dunklen Materie, welche in zwei Komponenten aufgeteilt ist. Die rote Farbe zeigt die Verteilung des heißen Gases, welches in Röntgenbeobachtungen sichtbar gemacht wurde. Deutlich ist zu erkennen, dass das Gas aufgrund von Druckkräften in der Nähe des Begegnungsortes beider Haufen geblieben ist, während Galaxien und dunkle Materie fast ungehindert durcheinander durchdringen konnten.

Galaxienhaufen sind zweifelsohne sehr interessante Objekte, die unter vielerlei astrophysikalischer Gesichtspunkten untersucht werden. Des weiteren sind Galaxienhaufen jedoch auch dazu geeignet die Kosmologie, also die Entwicklung des Universums, zu studieren. So ist etwa die Bildung von Galaxienhaufen eng mit der kosmischen Materieverteilung verbunden, sodass selbst eine mäßig genaue Messung ihrer Anzahldichte präzise Bestimmungen kosmologischer Parameter ermöglicht. Des Weiteren hängt die Anzahldichte sowohl von der kosmischen Expansion ab, welche die Dichte verringert, als auch von der kosmischen Strukturbildung, bzw. von deren Wachstumsrate. Diese zweifache Abhängigkeit macht Kosmologie mit Galaxienhaufen besonders interessant. Durch Galaxienhaufen gemessene kosmologische Parameter zeigen andere Abhängigkeiten und Entartungen auf als die anderer Methoden. So sind etwa einige der Entartungen in Ergebnissen von Galaxienhaufen fast senkrecht zu den Entartungen durch Messungen der kosmischen Hintergrundstrahlung, und die Kombination beider Methoden ist daher besonders interessant. Solche kombinierten Messungen sind höchstwahrscheinlich der Schlüssel zum Verständnis der beschleunigten Expansion.

Allerdings müssen, um Galaxienhaufen in der Kosmologie benutzen zu können, einige Schwierigkeiten überwunden werden. Der forderndste Teil ist dabei eine genaue und verlässliche Bestimmung der Masse von Galaxienhaufen, welche ja wie bereits erwähnt nicht direkt gemessen werden kann, sondern vielmehr anhand von Beobachtungen abgeleitet werden muss. Des Weiteren muss das zugrunde liegende Modell, welches die Daten mit den grundlegenden kosmologischen Parametern verbindet, genau bekannt und bestimmt sein.

Mit dieser Dissertation möchte ich mich einigen dieser Herausforderungen stellen, zu ihrer Überwindung beitragen und neue Ergebnisse vorstellen. Zunächst aber soll in einer Einleitung das kosmologische Grundgerüst, und speziell die allgemeine Relativität vorgestellt werden, sowie die Entstehung und Entwicklung von Galaxienhaufen. Im Anschluss werden wir auf die Verwendung von Galaxienhaufen zum Studium der Kosmologie eingehen sowie auf die wichtigsten Beobachtungsmethoden. Die Einleitung möchte ich schließlich mit einigen technischen Aspekten der verwendeten numerischen Methoden beschließen. Im Hauptteil dieser

Dissertation stelle ich eine Reihe von wissenschaftlichen Arbeiten im Bereich der Galaxienhaufen-Kosmologie vor, an denen ich im Laufe meiner Doktorarbeit gearbeitet habe.

In der ersten hier vorgestellten Arbeit benutzen wir den Galaxienhaufen-Katalog des South Pole Telescope (SPT), und richten unser Augenmerk auf Massenkalibrierung und Kosmologie. Das SPT ist ein am geographischen Südpol arbeitendes Millimeter-Wellen Teleskop, das es uns erlaubt, einen sauber selektierten Katalog an Galaxienhaufen zu erstellen, der auch die am meist rotverschobenen Galaxienhaufen beinhaltet. Als Ausgangspunkt dienen uns die vorhergehenden Bemühungen der collaboration, Röntgen-Daten für einen Teil des Katalogs zu beschaffen und im Rahmen einer kosmologischen Untersuchung zu nutzen. Wir haben nun spektrokopische Messungen hinzugefügt, die zum großen Teil ebenfalls von der SPT collaboration beschafft wurden. Die vorgestellte Arbeit hat zwei wichtige Ziele: 1) eine Methode zu entwickeln, um den SPT Katalog mit den beiden zusätzlichen Röntgen- und spektroskopischen Messungen auszuwerten, und 2) verschiedene Datenkombinationen in kosmologischer Hinsicht zu analysieren. Eines der zentralen Ergebnisse ist der Vergleich der typischen Galaxienhaufenmassen, die wir bei Verwendung der verschiedenen Daten erhalten. So ist etwa die Massenskala, die wir bei Benutzung der Röntgendifferenz messen, um ca. 44% niedriger als wenn *Planck*-Daten hinzugezogen werden. Die Kalibrierung anhand spektroskopischer Geschwindigkeitsdispersionen liegt in etwa dazwischen. Im Kosmologie-Teil führen wir schließlich einen interessanten Test durch, in dem wir sowohl die Zustandsgleichung der dunklen Energie – durch den Parameter  $w$  beschrieben – als auch die Rate der Strukturbildung, die wir mit einem phänomenologischen Modell parametrisieren, betrachten. Die Ergebnisse bestätigen, dass das Standard  $\Lambda$ CDM-Modell die Daten korrekt beschreibt.

Die zweite Arbeit beschäftigt sich mit zwei Massen-Observablen: das vom SPT gemessene Signal des Sunyaev-Zel'dovich Effekts und die optische “richness”  $\lambda$ , die mit dem redMaPPer Algorithmus in den “science verification” Daten der Dark Energy Survey (DES) gemessen wurde. Zunächst werden beide Kataloge kombiniert, wobei für jede Detektion durch SPT bis zu einem Signal-Rausch-Verhältnis von  $\xi > 4.5$  auch optische Entsprechungen gefunden werden. Der Überlapp zwischen beiden Himmelsdurchmusterungen führt zu einem kombinierten Katalog mit 25 Galaxienhaufen für den wir zeigen konnten, das zufällige Paarungen mit hoher Wahrscheinlichkeit ausgeschlossen sind. Wir wenden dann die abundance-matching Methode für den SPT Katalog mit einem kosmologischen Referenzmodell an, um die richness-Massen Relation zu bestimmen, wobei unsere Ergebnisse gut mit der Literatur übereinstimmen. Des weiteren untersuchen wir die typischen Versetzungen zwischen den von SPT und redMaPPer bestimmten Zentren der Galaxienhaufen. Diese Arbeit nutzt erste Daten der überlappenden SPT und DES surveys, und zeigt, dass bessere Ergebnisse und weiter reichende Untersuchungen mit dem Fortschritt des DES Programms möglich sein werden.

Seit der Veröffentlichung der ersten hier vorgestellten Arbeit wurde der vollständige,  $2500 \text{ deg}^2$  umfassende SPT Katalog publiziert. Ich stelle hier eine kosmologische Auswertung dieses vollständigen SPT Katalogs vor, in der ich insbesondere die Strukturbildung, wie auch im ersten SPT Projekt, untersuche. Die besseren Daten führen dabei zu sehr viel genaueren Messungen, und diese Arbeit stellt die derzeit besten Messungen der Strukturbildung anhand von Galaxienhaufen vor. Des weiteren zeigt sich, dass der zusätzliche Freiheitsgrad des Zustands der dunklen Energie  $w$  unsere Messung der kosmischen Wachstumsrate kaum schwächt. Unsere Daten zeigen keine Anzeichen einer Abweichung vom  $\Lambda$ CDM-Modell oder der allgemeinen Relativität.

In der vierten, theoretischeren Arbeit schließlich benutzen wir große numerischen Simulationen, um die Halo-Massenfunktion (HMF) zu bestimmen. Die HMF ist zentraler Bestandteil jeder kosmologischen Arbeit mit Galaxienhaufen, da sie das Bindeglied zwischen berechneter und beobachteter Anzahldichte in Abhängigkeit von Masse und Rotverschiebung darstellt. Die gewöhnlich verwendeten HMF wurden anhand von  $N$ -Teilchen Simulationen unter Vernachlässigung von möglichen baryonischen Effekten kalibriert. Wir gehen hier einen Schritt weiter und arbeiten mit den größten hydrodynamischen Simulationen, die derzeit verfügbar sind. Wir bestätigen dabei, dass baryonische Effekte in der Tat jenseits von  $\gtrsim 10^{14} M_\odot$  vernachlässigbar sind. Allerdings zeigen wir auch, dass diese Effekte für künftige Missionen wie eROSITA relevant sein werden, und dass deren Vernachlässigung dann zu Messabweichungen führen würden, die so groß wie der gesamte Messfehler wären. Wir stellen Fit-Funktionen der HMF für verschiedene Massendefinitionen vor.

Ich werde diese Dissertation mit einer Zusammenfassung beschließen und einige interessante aktuelle und künftige Projekte vorstellen.

# Abstract

Galaxy clusters are some of the largest astrophysical objects in the Universe. They contain a few tens up to several thousands of galaxies. As their name suggests, they were first discovered as overdensities of projected galaxies in the 1960s (e.g., Abell 1958; Zwicky et al. 1968). However, galaxies only represent a tiny contribution to the total mass of a cluster, typically of order 1%. Intergalactic gas, the so called intracluster medium (ICM) contributes about 9% of the total mass. The rest of the mass is in the form of dark matter. Given their composition, galaxy clusters can be observed through different techniques. In optical observations, only the galaxies are visible. Several techniques allow us to observe the ICM. Finally, the dark matter component is not directly observable. However, the shear due to weak gravitational lensing is sensitive to the total mass of a cluster, and it is therefore possible to also learn about the dark matter component.

The title figure of this thesis shows the well-known “bullet cluster”. It became famous because three different measurement techniques were employed to learn about its structure: The main cluster is located in the left part of the image and hosts a large number of galaxies as seen in the optical. To its right is the “bullet”, a smaller cluster that passed through the main cluster from left to right. The blue shading indicates the total mass distribution measured through the weak gravitational lensing technique. It clearly exhibits two separate structures. In red is the hot ICM gas as observed in the X-ray. The gas has stayed closer to the point of encounter of both clusters because of pressure forces, whereas the galaxies and the dark matter behave as pressure-less particles and simply passed through another.

However, besides being interesting objects to be studied from an astrophysical point of view, galaxy clusters are also suitable as cosmological probes and can help in improving our understanding of the Universe. The formation of galaxy clusters is directly linked to the distribution of matter in the Universe in a very sensitive way. Therefore, even a moderately precise measurement of the abundance of these objects as a function of their mass and redshift can lead to competitive cosmological constraints. Furthermore, the abundance of clusters depends both on the expansion history of the Universe – diluting their number density – as well as on the rate at which cosmic structure evolves and grows; this dual sensitivity makes galaxy cluster studies particularly interesting. In the space of cosmological parameters, results from galaxy clusters exhibit parameter degeneracies that are different than degeneracies from other cosmological probes. In particular, these degeneracies are approximately orthogonal to those from measurements of the cosmic microwave background anisotropies, which makes the combination of both probes a very powerful tool. Such joint analyses are of prime importance to understanding the accelerated expansion of the Universe.

To fully exploit galaxy cluster data, several challenges must be overcome. The most important one is determining reliable cluster masses. Because the cluster mass is not a direct observable, it needs to be estimated through one or more of the various techniques mentioned above. Another obviously important ingredient is robust modeling of the abundance of clusters as a function of the cosmological parameters of interest.

In this thesis, I will try to address some of the challenges of cluster cosmology and present some new results. First of all, I will start by introducing the basic framework of General Relativity needed to understand the evolution of our Universe. I will then discuss the formation of galaxy clusters and motivate their use as cosmological probes. Then, I will summarize the principle techniques employed to observe galaxy clusters and measure the relevant quantities for cosmological studies. Finally, I will discuss some of the technical aspects of the analysis techniques employed. After this introduction, I will present a series of scientific studies in the area of galaxy cluster cosmology that I pursued as part of my thesis work.

The first project I present is an analysis of the SPT cluster sample, focusing on cosmology and mass calibration. The SPT is a millimeter-wavelength telescope located at the South Geographic Pole. The telescope

has been performing a multi-wavelength, high angular resolution survey of the CMB. One of the main goals has been enabling the extraction of a sample of cleanly selected galaxy clusters that extends out to the highest redshifts where clusters exist. This work builds upon a previous study that the collaboration conducted using a subsample of the total survey, supplemented with X-ray observations for a subset of clusters. In the present study, we added further follow-up data from optical spectroscopy measurements that were obtained mostly by the SPT collaboration. This study has two main aspects: 1) establish a formalism that allows to combine the SPT sample with two kinds of follow-up data from X-ray and spectroscopic observations, 2) conduct a cosmological analysis, considering different data combinations. One of the key results is the comparison of the cluster mass scale that we obtain for different data combinations. For example, the mass scale preferred by the X-ray calibration is about 44% lower than the scale we obtain when adding *Planck* data to the fits. The calibration from velocity dispersions is between both. In terms of cosmology, we perform an interesting test where we allow both for a varying dark energy equation of state parameter  $w$  and deviations from standard growth of structure, parametrized by a phenomenological model. We find no evidence for departures from the standard  $\Lambda$ CDM model and growth according to General Relativity.

The second study focuses on two mass observables: The Sunyaev-Zel'dovich effect signal as extracted from the SPT survey maps, and optical cluster properties defined by the richness  $\lambda$ , as measured with the redMaPPer algorithm in the Dark Energy Survey (DES) science verification data. In a first stage, we cross-match the SPT and DES catalogs and find optical counterparts for each SPT detection down to a signal-to-noise of  $\xi > 4.5$ . Given the overlap between both surveys, our sample comprises 25 objects for which we show that false random associations can be excluded with high confidence. We then perform the abundance-matching technique against a fixed reference cosmology for the SPT sample, and simultaneously determine the parameters of the richness-mass relation. Our results agree with previous analyses. We also study the offset distribution between SPT and redMaPPer cluster centers. This study takes advantage of the overlap between the SPT and DES surveys, and indicates that better constraints and more detailed analyses will be possible as the DES survey progresses.

Since the publication of the first paper, the cluster data of the full  $2500 \text{ deg}^2$  SPT survey have been published. I present a cosmological analysis of the full SPT sample, in which I constrain the growth of structure as in the first project. However, the improved dataset lead to vastly improved constraints; in this paper we present the tightest constraints on cosmic growth from clusters to date. Another key result is that allowing for the dark energy equation of state parameter to vary as an additional free parameter does only mildly degrade our constraints on the growth rate. We find no evidence of tension with the  $\Lambda$ CDM model and the growth rate as predicted by General Relativity.

Finally, in a fourth and more theoretical study, we work on large numerical simulations to calibrate the halo mass function (HMF). The HMF is a key piece to every cluster cosmology test, as it predicts the number of clusters as a function of their mass and redshift. The commonly used HMFs are calibrated against  $N$ -body simulations under the assumption that baryonic effects can be neglected. We improve on these studies by using the largest hydrodynamic simulations available to date. We confirm that baryonic effects are indeed subdominant for massive clusters  $\gtrsim 10^{14} M_\odot$ . However, for future surveys that extend to lower masses such as eROSITA, neglecting these effects could lead to biases in the results that are of the same order as the expected overall uncertainties. We present fitting formulae for the HMF for different cluster mass definitions.

A final chapter contains the conclusions and some discussion of future topics of particular interest.

# Contents

<b>Zusammenfassung</b>	<b>v</b>
<b>Abstract</b>	<b>vii</b>
<b>1 Introduction</b>	<b>1</b>
1.1 Cosmology and Galaxy Clusters . . . . .	1
1.2 Galaxy Cluster Astrophysics . . . . .	11
1.3 Parameter Estimation . . . . .	14
1.4 Conclusions and Outlook . . . . .	16
<b>Mass Calibration and Cosmology</b>	
<b>2 Mass Calibration and Cosmological Analysis of SPT-SZ Galaxy Clusters</b>	<b>21</b>
<b>S. Bocquet, A. Saro, J. Mohr, et al. 2015</b>	
<i>The Astrophysical Journal (APJ)</i> , 799, 214	
<b>3 Optical properties of SPT selected clusters</b>	<b>47</b>
A. Saro, <b>S. Bocquet</b> , et al. 2015	
to be submitted to <i>Monthly Notices of the Royal Astronomical Society (MNRAS)</i>	
<b>4 Growth of Structure Measured with SPT-SZ Galaxy Clusters</b>	<b>67</b>
<b>S. Bocquet</b> et al., in preparation	
to be submitted to <i>The Astrophysical Journal Letters (APJL)</i>	
<b>Calibration of the Cluster Mass Function</b>	
<b>5 Baryons and the halo mass function</b>	<b>77</b>
<b>S. Bocquet, A. Saro, K. Dolag, and J. J. Mohr 2015</b>	
submitted to <i>Monthly Notices of the Royal Astronomical Society (MNRAS)</i> , ArXiv:1502.07357	
<b>6 Final remarks</b>	<b>95</b>
6.1 Summary . . . . .	95
6.2 Discussion and Outlook . . . . .	97
<b>Bibliography</b>	<b>99</b>
<b>List of scientific publications and talks</b>	<b>107</b>
<b>Acknowledgments</b>	<b>109</b>



# Chapter 1

## Introduction

This thesis is dedicated to galaxy cluster analyses in a cosmological context. It therefore covers different topics including galaxy cluster observations and astrophysics, cosmology, statistical methods, numerical simulations, and development of analysis tools. The work conducted in this thesis is at the exciting intersection between theory and observations. Although each scientific study presented here covers slightly different aspects, they are all related to the question of how to use current and future cluster data to constrain cosmology in a robust and statistically correct way. Obviously, these requirements can only be met if one fully understands what kind of observations is needed to measured the relevant cluster properties and how the cluster sample was constructed. Furthermore, one needs to apply reliable and well-tested analysis methods. Finally, a profound knowledge of the tested theory is required to draw meaningful conclusions.

The work presented in this thesis was conducted with the goal to contribute some new analysis methods and results to the field of cluster cosmology. Furthermore, this thesis hopefully provides a useful overview and introduction to this field. To start with, I review the basic ingredients needed to understand the relevance of the studies conducted for this thesis. While this overview is certainly not extensive, it should provide the reader with the necessary background knowledge for appreciating the presented work. In the following, I discuss the fundaments of cosmology and show how galaxy clusters are deeply linked to key properties of our Universe. After this theoretical part, I highlight some of the astrophysical methods used to observe galaxy clusters. Finally, in a somewhat more technical section, I describe practical aspects of parameter fitting in up to  $\sim 30$  dimensions. I conclude with a summary and outlook that set the stage for the main part of this thesis.

### 1.1 Cosmology and Galaxy Clusters

#### 1.1.1 The homogeneous Universe

With his theory of General Relativity, Albert Einstein formulated the description of space-time:

$$G_{\mu\nu} + \Lambda g_{\mu\nu} = \frac{8\pi G}{c^4} T_{\mu\nu}. \quad (1.1)$$

These are a set of coupled, nonlinear equations that can only be exactly solved under further, simplifying assumptions. The cosmological principle states that the Universe is homogeneous and isotropic. While this is certainly not true on terrestrial scales or in the solar system or even the Milky Way, it is a good approximation on very large scales  $\gtrsim 100$  Mpc. The application of the cosmological principle leads to the Friedmann-Lemaître-Robertson-Walker metric

$$ds^2 = c^2 dt^2 - a(t)^2 d\chi^2 \quad (1.2)$$

with the speed of light  $c$ , the scale factor  $a(t)$ , and the 3-dimensional spatial, time-independent metric  $d\chi$ . The spatial metric has the form

$$d\chi^2 = \frac{dr^2}{1 - kr^2} + r^2 d\Omega^2 \quad (1.3)$$

with unitless distance  $r$ , the curvature of space  $k$  and the solid angle  $\Omega$ . The curvature  $k$  takes values  $-1, 0, 1$  for negative, zero, and positive curvature. Still under the assumption of the cosmological principle, one can now solve Einstein's equation, and – after some arithmetic – obtain the Friedmann equations

$$H^2 \equiv \left(\frac{\dot{a}}{a}\right)^2 = \frac{8\pi G}{3}\rho - \frac{kc^2}{a^2} \quad (1.4)$$

and

$$\dot{H} + H^2 = \frac{4\pi G}{3}\left(\rho + \frac{3p}{c^2}\right). \quad (1.5)$$

Here,  $\rho$  is the mass (energy) density, and  $p$  is the pressure. These expressions appear in the Friedmann equations as they correspond to the trace of the stress-energy tensor  $T_{\mu\nu}$  in Einstein's equation. A useful reformulation of the above equations is

$$\dot{\rho} = -3H\left(\rho + \frac{p}{c^2}\right), \quad (1.6)$$

which allows to describe the evolution of density over time. Note that the cosmological constant  $\Lambda$  has been absorbed into  $\rho$  and  $p$ .

For perfect fluids with equation of state  $p = w\rho c^2$ , one can exactly solve the Friedmann equations. Further assuming spatial flatness ( $k = 0$ ), the density of the fluid evolves depending on its equation of state parameter  $w$  as

$$\rho(t) \propto a^{-3(1+w)}. \quad (1.7)$$

In the following, we will consider ordinary matter (effectively pressure-less dust,  $w = 0$ ), radiation (relativistic,  $w = 1/3$ ), and dark energy ( $w = -1$ ). It follows from Equation 1.7 that the comoving dark energy density is constant,  $\dot{\rho}_{\text{DE}} = 0$ .

In Equation 1.4, the curvature, the density, and the Hubble constant are related to each other. It is convenient to define the critical density

$$\rho_c \equiv \frac{3H^2}{8\pi G} \quad (1.8)$$

which defines the density at which the curvature vanishes,  $k = 0$ . One can further define the density parameter  $\Omega_X \equiv \rho_X/\rho_{\text{crit}}$  for each type of energy component X. With this definition, the first Friedmann equation is re-expressed as

$$\frac{H^2}{H_0^2} = \Omega_r a^{-4} + \Omega_m a^{-3} + \Omega_k a^{-2} + \Omega_\Lambda a^{-3(1+w)}, \quad (1.9)$$

where the subscript zero means “today”, and where the density parameters refer to their present values:  $\Omega_r$  the radiation density,  $\Omega_m$  the matter density,  $\Omega_k$  the curvature density ( $\Omega_k \equiv 1 - \Omega_r - \Omega_m - \Omega_\Lambda$ ), and  $\Omega_\Lambda$  the dark energy density. It is useful to express the above equation in terms of the cosmological redshift. Light emitted from a very distant object with wavelength  $\lambda_{\text{em}}$  is observed at longer wavelength  $\lambda_{\text{obs}}$  on Earth because space between the emitter and us has expanded since photon emission. The redshift is defined as

$$z \equiv \frac{\lambda_{\text{obs}} - \lambda_{\text{em}}}{\lambda_{\text{em}}} \quad (1.10)$$

and can directly be related to the scale factor via  $1 + z = a(t_0)/a(t_e)$ , where  $t_e$  stand for the time of emission. We can now restate equation 1.9 as a function of redshift. In the late Universe, it follows from equation 1.7 that the radiation component has redshifted away and can be neglected. Still assuming spatial flatness, we can write down

$$E^2(z) \equiv \frac{H^2}{H_0^2} = \Omega_m(1+z)^3 + \Omega_\Lambda(1+z)^{3(1+w)}, \quad (1.11)$$

and conclude the description of the homogeneous Universe.

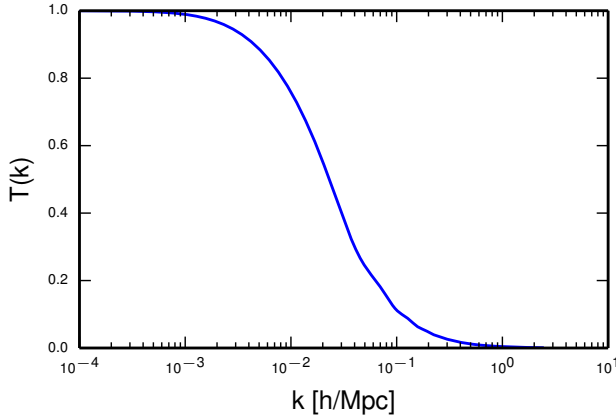


Figure 1.1 The total matter transfer function (CDM+baryons+neutrinos) at redshift 0 as calculated by CAMB. The BAO wiggles are visible around  $k \sim 0.1 h/\text{Mpc}$ .

### 1.1.2 The inhomogeneous Universe

Looking at the world around us, it is obvious that the Universe is not homogeneous. In fact, everything we observe – starting with ourselves – is definitely neither homogeneous nor isotropic. In this section we will review the basic description of small cosmological inhomogeneities and create a link to the formation of galaxy clusters. Indeed, their formation is deeply linked to the fundamental level of inhomogeneity in the Universe which makes them such a powerful and interesting probe of cosmology.

We define perturbations as  $\delta \equiv \rho/\bar{\rho} - 1$ , with the mean density  $\bar{\rho}$ . They evolve according to the continuity, Euler and Poisson equations, which for small perturbations  $|\delta| < 1$  can be combined to give

$$\ddot{\delta} + 2H\dot{\delta} + \left(\frac{k}{a}\right)^2 \frac{\delta P}{\rho} - \frac{3}{2} H^2 \Omega_m(t) \delta = 0, \quad (1.12)$$

with pressure fluctuations  $\delta P$ . For cold dark matter (no pressure) this equation has a growing solution

$$\delta(t) \propto D(z) = H(z) \int_z^\infty \frac{dz'(1+z')}{H^3(z')} \cdot \quad (1.13)$$

This expression is also referred to as the growth factor  $D(z)$ .

After the era of inflation, the primordial fluctuations were Gaussian, scale-free, and adiabatic. Different  $k$ -modes are independent meaning that they evolve independently as  $D(z)$ . The matter power spectrum – the mean Fourier transform of the spatial correlation function – can then be written as a function of wavenumber  $k$  as

$$P_{\text{primordial}}(k) = A_0 k^{n_s} \quad (1.14)$$

with an initial normalization  $A_0$  and the scalar spectral index  $n_s$ . We will come back to the normalization later. The scalar spectral index is slightly smaller than unity (e.g., Planck Collaboration et al. 2015a), meaning that there is more power on large scales than on small scales. The exact value of  $n_s$  is sensitive to the processes that end inflation and therefore carries information about inflation itself. However, for this work, it is sufficient to consider  $n_s$  as a phenomenological parameter.

As the primordial Universe evolves, several effects need to be accounted for that ultimately render the matter power spectrum scale-dependent. The evolution of the matter power spectrum is captured as

$$P(k, z) = P_{\text{primordial}}(k) D(z)^2 T(k, z)^2 \quad (1.15)$$

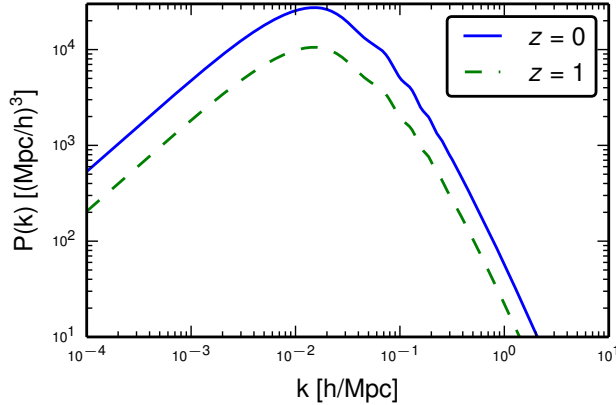


Figure 1.2 The matter power spectrum as calculated by CAMB. The overall offset between both spectra corresponds to the structure growth between redshift 1 and 0. The BAO wiggles are visible around  $k \sim 0.1 h/\text{Mpc}$ .

with the linear growth rate  $D$  as described above. The transfer function  $T$  describes how the shape of the initial power spectrum is altered due to different physical processes, including interactions between baryons and photons. In principle, the transfer function is obtained by solving Equation 1.12 for each matter species and accounting for their couplings. Indeed, there are approximate expressions for the transfer function (e.g., Eisenstein & Hu 1998, 1999). However, the exact solution for the transfer function cannot be obtained analytically, especially due to the complicated (de-)coupling between baryons and photons which implies solving the multi-species Boltzmann equation. Numerical codes such as CAMB<sup>1</sup> or CLASS<sup>2</sup> take a few seconds to provide accurate transfer functions. The transfer function at redshift  $z = 0$  is shown in Figure 1.1.

Discussing some key features is quite instructive. The most important scale is the horizon scale at matter-radiation equality  $k_{\text{eq}} \sim 0.01 \text{ Mpc}^{-1}$ . At early times, before matter-radiation equality, and on large, super-horizon scales, dark matter, baryons, and radiation evolve together and perturbations can grow according to  $D(z)$ ; the transfer function is  $T = 1$ . However, perturbations on sub-horizon scales grow only logarithmically with time until matter-radiation equality (Mészáros effect, Meszaros 1974). Shorter modes entered the horizon earlier than longer modes, and thus have had more logarithmic growth by the end of radiation domination. Together, these effects lead to the characteristic, bent shape of the transfer function that suppresses the power on small scales. Note that after matter-radiation equality, perturbations grow uniformly on all scales. The transfer function further exhibits some wiggles at intermediate wave numbers. These are the baryon acoustic oscillations (BAO), which correspond to standing waves in the baryon-photon plasma before recombination. When both species were coupled, baryons get gravitationally attracted to the gravitational wells formed by the dark matter, while the pressure in the radiation component goes in the opposite direction. At recombination, these oscillations cease, and the distribution of baryonic matter is fixed. The corresponding length scale evolves according to the background expansion, and can now be used as a standard ruler for measuring the geometry of the Universe (for a review, see e.g., Weinberg et al. 2013).

Figure 1.2 shows the total matter power spectrum at redshift  $z = 0$ . The shape of the large-scale end  $k < k_{\text{eq}}$  simply corresponds to the primordial power spectrum multiplied with the growth factor (remember that the transfer function is equal to unity on these scales, c.f. figure 1.1). As anticipated, the maximum of the power spectrum is directly linked to the horizon at matter-radiation equality, and arises due to the product of the primordial power spectrum ( $P \propto k$ ) with the square of the transfer function with its characteristic suppression for  $k > k_{\text{eq}}$ . The BAO features are visible at  $k \sim 0.1 h/\text{Mpc}$  and at larger wavenumber, the power spectrum drops

<sup>1</sup><http://camb.info>

<sup>2</sup><http://class-code.net>

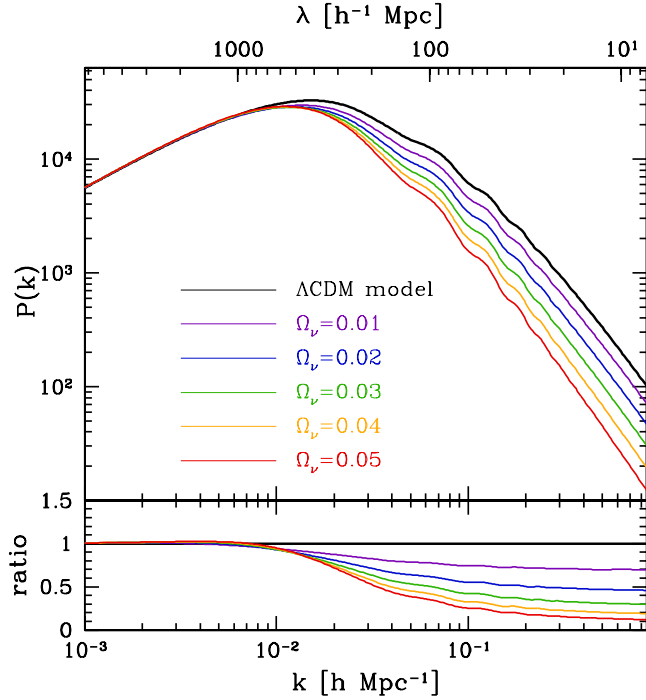


Figure 1.3 Impact of massive neutrinos on the matter power spectrum (figure taken from Park et al. 2012).

as  $P \propto P_{\text{primordial}} T^2 \sim k^{-3}$ . The dimensionless power spectrum  $\Delta^2(k) \equiv k^3 P(k)/2\pi^2$  measures the contribution of perturbations at wavenumber  $k$ . It increases as  $\Delta^2(k) \propto k^4$  at low  $k$ , and becomes approximately constant for large  $k$ . This implies that the smallest scales become non-linear first; we have hierarchical, bottom-up structure formation.

Several practical purposes and measurements require the computation of the variance of the fluctuations on a particular filtering scale. A common choice is  $\sigma(M)$ , where the scale is chosen as the sphere of radius  $R$  encompassing the mass  $M = 4\pi/3 \rho_m R^3$ , with the mean matter density  $\rho_m$ . The variance of the matter power spectrum  $P(k, z)$  then is

$$\sigma^2(M, z) \equiv \frac{1}{2\pi^2} \int P(k, z) \hat{W}^2(kR) k^2 dk, \quad (1.16)$$

with the Fourier transform  $\hat{W}$  of the real-space top-hat window function of radius  $R$ . We will come back to the variance  $\sigma$  when predicting the number density of galaxy clusters from the power spectrum.

So far, we have assumed massless neutrinos. However, the confirmation of neutrino oscillations directly implies that at least one neutrino has a non-zero mass (for a review, see e.g., Gonzalez-Garcia et al. 2012). While a thorough discussion of neutrino physics would be beyond the scope of this introduction, we briefly discuss how the neutrino masses affect the matter power spectrum. Because they are very light, neutrinos still travel at high velocities close to the speed of light. Therefore, they are also called hot dark matter (HDM). However, because of their high velocities, neutrinos tend to free stream out of the gravitational potential wells formed by (cold) dark matter and baryons. This leads to a decrease of power of those scales, as just discussed for WDM. Figure 1.3 shows this effect for a range of different neutrino densities  $\Omega_\nu$ , which is directly related to the sum of neutrino masses via  $\sum m_\nu = 94 \text{ eV } \Omega_\nu h^2$ . Note how the suppression of power on intermediate and small scales increases with increasing neutrino mass. Conversely, this means that one can learn about the sum of neutrino masses if one is able to measure the amount of this suppression. In fact, we will apply this technique later in this thesis to constrain  $\sum m_\nu$ .

### 1.1.3 The Cosmological Parameters

Having reviewed the basic theoretical ingredients, it is time to summarize the cosmological parameters that are of interest for this thesis. Obviously, the set of free parameters depends on the model we choose to adopt. Let us start with the spatially flat  $\Lambda$ CDM model (CDM and cosmological constant  $\Lambda$ ) which is described by 6 parameters:

- $\Omega_m$ : total matter
- $\Omega_b$ : ordinary matter (baryons)
- $H_0$ : Hubble constant
- $A_s$ : normalization of the power spectrum
- $n_s$ : tilt of the primordial power spectrum
- $\tau$ : reionization optical depth

The parameter  $\tau$  only is relevant when analyzing the cosmic microwave background, which will briefly be described in the following section. Because of the assumption of spatial flatness the dark energy density parameter is not a free parameter but is directly linked to the matter density as  $\Omega_\Lambda = 1 - \Omega_m$ . Further note that the normalization of the power spectrum can be defined in two ways: 1) directly normalize  $P(k)$  at some scale, or 2) use the variance  $\sigma(M)$  from Equation 1.16. In the latter case, the common choice is  $\sigma_8$ , where the radius of the top-hat filter is  $8 h^{-1} \text{Mpc}$ . Another common choice is to replace the Hubble parameter by the CMB acoustic scale  $\theta_{\text{MC}}$  since both are related quantities that can be converted to each other.

An obvious generalization of the flat  $\Lambda$ CDM model is to relax the assumption of spatial flatness and to consider  $\Omega_\Lambda$  as a free parameter. The curvature density is zero to within  $\pm 0.005$  (Planck Collaboration et al. 2015a) and throughout the rest of this thesis we will assume spatial flatness. The following list provides an overview of further extensions that are relevant for this thesis:

- $w$ : The standard assumption about the dark energy equation of state parameter  $w = -1$  is relaxed.
- $\sum m_\nu$ : The sum of the neutrino masses is allowed to vary.
- $\gamma$ : The growth factor of matter fluctuations in the late Universe is assumed to evolve according to some model that is parametrized by  $\gamma$ .

All these extensions can either be considered as one-parameter extensions to the base-line model, or one analyzes combinations of two or more. Of course there are many more extensions to the  $\Lambda$ CDM model considered in the literature such as an altered number of relativistic species  $N_{\text{eff}}$ , a running of the spectral index, evolution of  $w$ , and tensor perturbations, just to name a few of them.

We will now review how the cosmological parameters can be constrained. Before focusing on the formation of galaxy clusters and their use as a cosmological probe, we will briefly review other standard cosmological probes. We will be referring to these in the main body of this thesis.

### 1.1.4 The Cosmic Microwave Background

In the early, hot Universe photons, electrons and baryons are tightly coupled to form a hot plasma. As the Universe expands and cools down to temperatures below  $\sim 3000$  K, electrons and protons *recombine* to form hydrogen. At this point, which corresponds to an age of the Universe of about 380,000 years, photons do not interact with the neutral atoms any more and travel freely. Today, this omnipresent radiation can be detected with microwave receivers, and provides a direct image of the early Universe. During their way to us, the photons' energy has decreased due to the expansion of the Universe, and today the cosmic microwave background

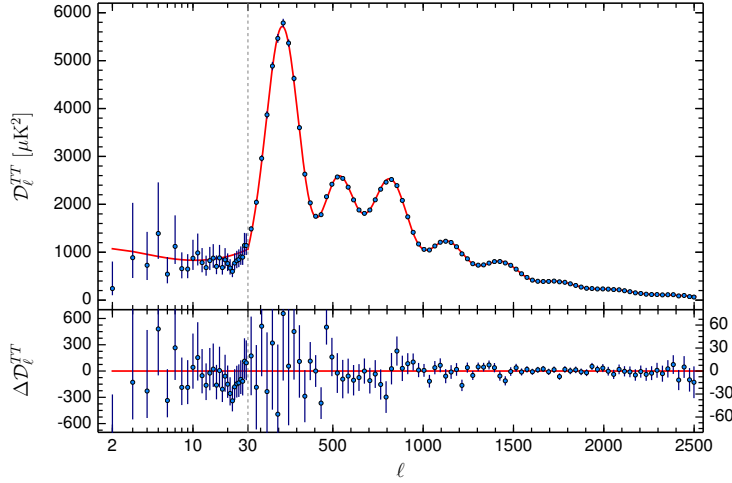


Figure 1.4 CMB temperature power spectrum as measured by *Planck*. The red line corresponds to the best-fitting  $\Lambda$ CDM model, which is a remarkably good fit to the data (Planck Collaboration et al. 2015a).

(CMB) radiation has a temperature of 2.73 K. This corresponds to a redshift of recombination  $z_{\text{rec}} = 1100$ . To first order, the CMB is homogeneous and isotropic, and exhibits a black body spectrum. However, it also contains fluctuations that are as small as  $10^{-5}$ ; these correspond to the anisotropies discussed in the previous section.

Figure 1.4 shows the CMB angular temperature power spectrum as measured by the *Planck* satellite. The spectrum can be accurately calculated by a Boltzmann code such as **CAMB**. Note that the fluctuations at the scales of interest are well described by linear perturbation theory which makes this cosmological probe particularly powerful. For example, the angular scale of the first peak (about  $1^\circ$ ) can be related to the sound horizon at recombination which provides a powerful way of measuring the curvature of the Universe. Assuming the  $\Lambda$ CDM model, spatial flatness is confirmed with a spectacular uncertainty on  $\Omega_k$  of  $\pm 0.005$  (Planck Collaboration et al. 2015a). Then, the position and amplitudes of the peaks carry information about the baryon and CDM densities and also allow to distinguish between adiabatic and isocurvature primordial fluctuations. Finally, the power in CMB anisotropies can be used to normalize the matter power spectrum (*Planck* makes this measurement at the scale  $k_0 = 0.05 \text{ Mpc}^{-1}$ ).

### 1.1.5 Other cosmological probes

The standard cosmological toolbox further contains two distance-measurement techniques. Supernovae of type Ia (SNIa) feature a characteristic relationship between their light curve and absolute luminosity. With this relation, one can use SNIa as standard candles and measure their distance as a function of redshift. In practice, one measures the luminosity distance, which is a function of the Hubble parameter  $H(z)$ . In fact, applying this technique lead to the discovery of the accelerated expansion of the Universe (Riess et al. 1998; Perlmutter et al. 1999). In this thesis we will use the Union2.1 compilation of 580 SNIa (Suzuki et al. 2012). Another technique relies on measuring the BAO peak at some redshift  $z$  using data from large galaxy surveys. One typically constrains the combination  $D_V(z)/r_s$ , where  $r_s$  is the comoving sound horizon at the baryon drag epoch and  $D_V(z) \equiv [(1+z)^2 D_A^2(z)cz/H(z)]^{1/3}$ , where  $D_A$  is the angular diameter distance (which itself is a function of  $H(z)$ ). In this thesis, we will use a combination of several such measurements at different redshifts  $z = 0.106$  (Beutler et al. 2011),  $z = 0.35$  (Padmanabhan et al. 2012) and  $z = 0.57$  (Anderson et al. 2012).

Both SNIa and BAO effectively probe  $H(z)$ , and are therefore sensitive to the matter density  $\Omega_m$ , the dark

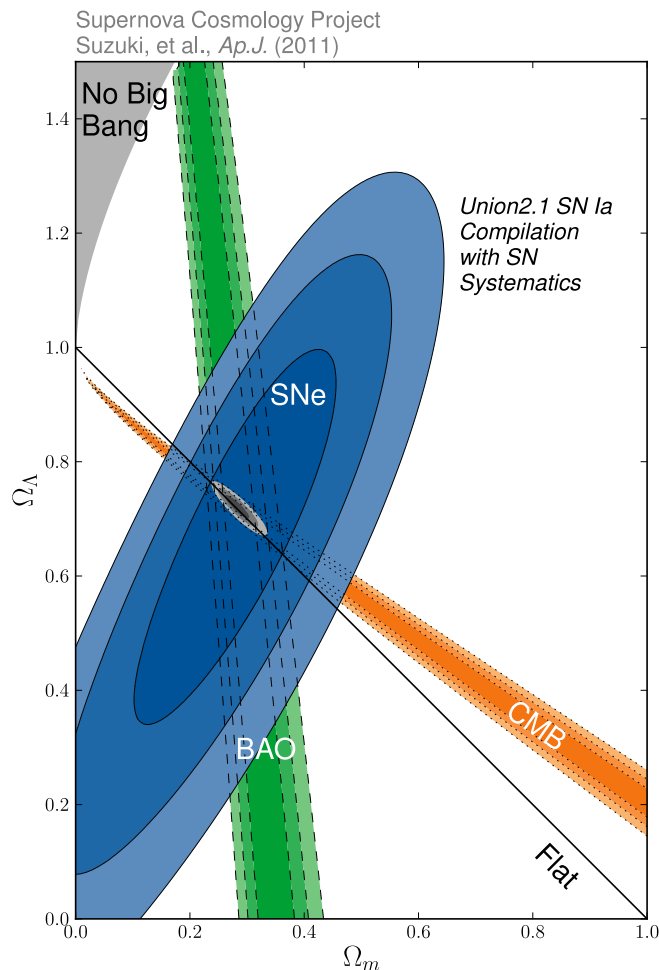


Figure 1.5 Constraints on a non-flat  $\Lambda$ CDM model from different probes (Suzuki et al. 2012). Their different and partially orthogonal degeneracies make them very complementary. The combination of all probes leads to very tight constraints.

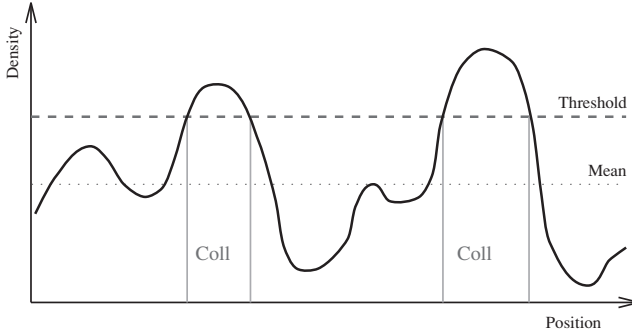


Figure 1.6 Schematic illustration of the smoothed matter density field. Regions with densities exceeding the threshold will collapse according to the Press-Schechter theory. Figure taken from Lyth & Liddle (2009).

energy density  $\Omega_\Lambda$ , and dark energy (e.g.,  $w$ ). Also note that both methods measure *relative* distances, but they are insensitive to the *overall* normalization of the Hubble relation  $H_0$ . This quantity can be measured using the cepheid method. Cepheids feature a direct relationship between their pulsation period and luminosity and can therefore be used to constrain  $H_0$  at low redshifts (e.g.,  $H_0 = 73.8 \pm 2.4 \text{ km s}^{-1} \text{ Mpc}^{-1}$ , Riess et al. 2011).

The cosmological probes discussed so far exhibit characteristic parameter degeneracies. Figure 1.5 shows this situation in the  $\Omega_m - \Omega_\Lambda$  plane for a  $\Lambda$ CDM model with non-zero curvature. In this example, the three probes are very complementary because of their degeneracies that do not align. Therefore, the combination of these datasets leads to much tighter constraints than obtained from the individual probes.

### 1.1.6 Cluster Formation, the Halo Mass Function, and Cosmology

So far, we have discussed density fluctuations that are small enough to be described by linear perturbation theory. However, it is clear that extended, overdense regions will continue contracting beyond the linear regime. We will now discuss the formation of dark matter haloes due to the collapse of overdense regions.

We can train our intuition with an analytic approach. The spherical collapse model predicts that the linear density contrast of a collapsed (spherical) perturbation is  $\delta_c = 1.69$ . As a consequence, any overdensity exceeding the threshold  $\delta_c$  will collapse. The size and therefore the mass of the collapsed object then depends on the size of the region exceeding the threshold, as illustrated in Figure 1.6. Obviously, given a Gaussian density field, high-mass objects are much less likely to form than their smaller, low-mass counterparts. It is now straightforward to predict the number density of collapsed objects as a function of their mass. The probability that a region enclosing the mass  $M$  exceeds the threshold is given by

$$P(M, z) = \text{erfc}\left(\frac{\delta_c}{\sqrt{2}\sigma(M, z)}\right), \quad (1.17)$$

expressed in terms of the complementary error function. The halo mass function  $dn/dM$  is then obtained by differentiating the above equation with respect to mass, and multiplying with the volume of a halo of mass  $M$  in the initial density field  $\rho_m/M$ . Effectively, this sets a number density of objects. In the end, this yields the Press-Schechter mass function (Press & Schechter 1974)

$$\frac{dn(M, z)}{dM} = -\sqrt{\frac{2}{\pi}} \frac{\rho_m}{M} \frac{\delta_c}{\sigma^2(M, z)} \frac{d\sigma(M, z)}{dM} \exp\left(-\frac{\delta_c^2}{2\sigma^2(M, z)}\right). \quad (1.18)$$

The mass function is shown in Figure 1.7. For low-mass cluster  $M \lesssim 10^{14} M_\odot$ , the number density evolves as a power-law with mass. More massive objects, however, are much less likely, resulting in an exponential

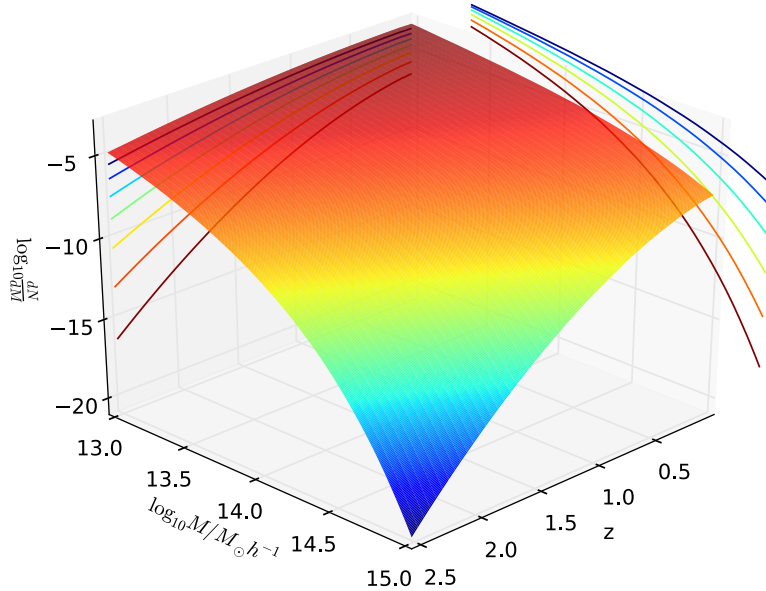


Figure 1.7 The halo mass function per unit mass and redshift. The number density decreases as a function of mass and redshift. Note how it quickly drops for high masses  $\sim 10^{15} M_{\odot}$ .

drop of the mass function toward the highest masses. As one would expect, the number density of objects increases with cosmic time (decreasing redshift), as  $\sigma(M)$  increases and they have more time to form.

Given its level of simplicity, the Press-Schechter formalism is still a surprisingly good description of the halo abundance. However, for actual studies of cluster cosmology, one uses a halo mass function calibrated against large numerical  $N$ -body simulations. In this case, the functional form motivated by the Press-Schechter approach is kept, but the parameters are set by the simulations. The standard reference is Tinker et al. (2008).

The mass function as discussed so far is given for unit mass and redshift. In order to use it for any cosmological purpose, one needs to multiply with the survey volume. In general, the survey will comprise some solid angle  $\Omega$  of the sky, and the redshift volume element is

$$dV(z, \Omega) = D_H \frac{D_M^2(z)}{E(z)} d\Omega dz \quad (1.19)$$

with the Hubble distance  $D_H \equiv c/H_0$  and the transverse comoving distance  $D_M$ . For a flat universe,  $D_M$  equals the line-of-sight comoving distance

$$D_C(z) = D_H \int_0^z \frac{dz'}{E(z')} \quad (1.20)$$

An overview of further cosmological distance measures and the generalization of the measures summarized here to non-flat cosmologies can be looked up in Hogg (1999).

With the predicted halo abundance from Equations 1.18 and 1.19 we are now set to perform a cluster cosmology analysis. However, as can be seen from the derivation of the cluster abundance, this analysis is not sensitive to all cosmological parameters; in particular, there is no dependence on  $\tau$ . The matter density enters through  $\rho_m$ . The amplitude of the matter power spectrum enters through  $\sigma(M)$  and clusters therefore are an ideal probe for measuring  $\sigma_8$ . Indeed, as shown in Figure 1.8(a), clusters provide tight constraints on  $\Omega_m$  and  $\sigma_8$ . These are particularly complementary with CMB anisotropy constraints given their approximate orthogonality. A particular strength of cluster cosmology is that the cluster abundance is both affected by the

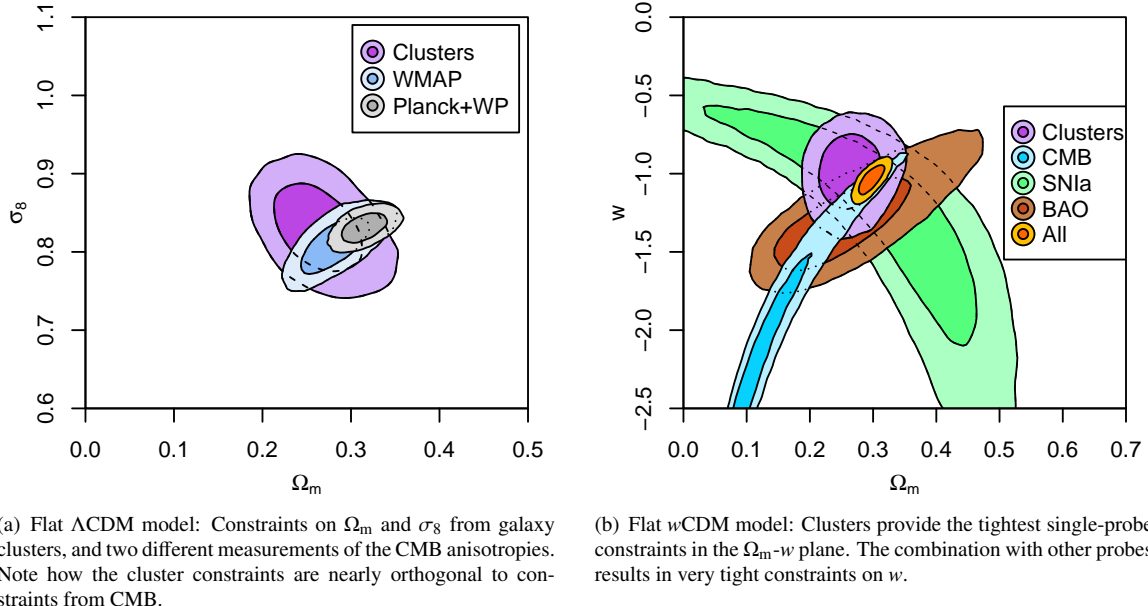


Figure 1.8 Illustration of cluster constraints compared with other cosmological probes (Mantz et al. 2015).

geometry of the Universe (through  $\rho_m$  and  $dV/dz$ ) as well as growth of structure through the power spectrum. Since both are affected by a change in the dark energy equation of state parameter  $w$ , clusters provide some of the tightest single-probe constraints on dark energy. This is shown in Figure 1.8(b) together with constraints from other probes. The combination of all probes leads to very tight constraints on  $w$  at the few percent level (Mantz et al. 2015).

## 1.2 Galaxy Cluster Astrophysics

In the previous section we have motivated the use of galaxy clusters in cosmology. In particular, the results in Figure 1.8 show that clusters can indeed be used as a competitive cosmological probe. However, in the theoretical derivation of the halo abundance, we have not yet accounted for the fact that cluster masses are not directly accessible observables. In fact, both the Press-Schechter approach as well as numerical simulations predict the abundance of dark matter haloes (plus gas if running a hydrodynamic simulation). These haloes host the galaxies and intergalactic gas. One therefore needs a way to relate observations of cluster galaxies or the gas component to the total mass of the clusters. This is a challenging task since ordinary, baryonic matter only contributes about 10% of the total cluster mass. Luckily, there are several different methods that provide cluster mass estimates. In this section, we will address the most important observational and methodological aspects of cluster cosmology. Comparisons of these different methods will be presented in the main body of this thesis.

### 1.2.1 Mass-Observable Scaling Relation and Sample Selection

As we will discuss in detail in the next sections, there is a variety of different techniques to estimate a cluster's mass. Not too surprisingly, all of them have in common that a precise measurement requires good (and therefore expensive) data. Let us set aside what exactly "good" means here and discuss the idea of scaling relations. The basic concept is to relate the observable  $O$  that a given technique provides to the cluster mass through a

parametric relation. We assume a power-law expression in mass  $M$ :

$$O = A M^B f(z)^C \quad (1.21)$$

with normalization  $A$ , mass slope  $B$ , and redshift evolution  $C$ . The redshift-dependent function  $f(z)$  ideally has a theoretical motivation; common choices are  $f(z) \equiv 1+z$  or  $f(z) \equiv E(z)$ . Given that each cluster is intrinsically a unique object, we must account for an intrinsic scatter between the true cluster true mass and the measured observable. Throughout this work, we will denote the scatter with  $D$ . Finally, the measurement of  $O$  will be affected by some (known) measurement uncertainty.

The key advantage of working with scaling relations is that once its parameters  $A$ ,  $B$ ,  $C$ , and  $D$  are properly calibrated, it can be used to readily estimate masses for all clusters with a measurement of  $O$ . In practice of course, this only works under the assumption that it is possible to calibrate the parameters in some reliable way in the first place. Luckily, there are such techniques: for example, measuring the shear induced by weak gravitational lensing by a massive cluster allows to obtain an accurate mass estimate (e.g., Applegate et al. 2014; Hoekstra et al. 2015), and the dispersion in the velocities of cluster galaxies can be calibrated against numerical  $N$ -body simulations (e.g., Evrard et al. 2008; Saro et al. 2013).

The basic strategy for a cluster cosmology analysis is to start with a survey catalog. In practice, the survey observable will be an observationally cheap one in order to be able to cover reasonable survey volumes. Because of the intrinsic scatter in the mass-observable relation, it is crucially important to construct the catalog based on some well-defined selection function (i.e., all clusters with  $O >$  threshold). Otherwise, the analysis will suffer from the Eddington bias and produce wrong results: Given the steep decline of the mass function with increasing (true) cluster mass, a cluster with a measured  $O$  is more likely to have scatter up in mass than to have scattered down. We show this in Figure 1.9, where for a given cluster with measured  $O$  the dashed green curve is obtained by “naively” inverting the scaling relation from Equation 1.21. However, as just discussed, this approach overestimates the mass of the cluster. The unbiased estimate is obtained by multiplying this estimate with the distribution from which the cluster was drawn from in the first place (which is the mass function  $P(M)$  is the equation below, shown as the thick black line in the figure):

$$P(M|O) = P(O|M)P(M). \quad (1.22)$$

The correct, unbiased mass estimate is shown as the blue curve in the figure. The effect of Eddington bias on a cluster sample is nicely illustrated in the set of figures A1 in Mantz et al. (2010a).

Finally, to calibrate the survey scaling relation, one collects follow-up data for survey clusters. Given parameter covariances between the parameters of the different scaling relations and with cosmology, it is preferable to perform the survey observable calibration simultaneously with the cosmological analysis, instead of applying a fixed, previously calibrated scaling relation. We will discuss the details of such a joint analysis with multiple observables in the main part of the thesis in Section 2.4.1.

## 1.2.2 Optical Cluster Observables

Optical data is of prime importance for obtaining redshifts and for confirming galaxy clusters proposed by other detection techniques. Furthermore, there are optical observables that can serve as cluster mass proxies. We will make use of two such observables in the main body of this thesis.

A way of characterizing clusters in optical data is through their richness, which is essentially the number of member galaxies weighed with their probabilities of actually being cluster members (Rykoff et al. 2012). This technique is implemented in the red-sequence Matched-Filter Probabilistic Percolation (redMaPPer) cluster finder which has been applied to data of the Sloan Digital Sky Survey (SDSS), and, relevant for this thesis, data of the Dark Energy Survey. We will present a study of the richness-mass scaling relation, and how it relates to other mass estimates in Chapter 3.

Another optical mass proxy relies on spectroscopic data. Besides their use for obtaining accurate and precise redshift measurements, these data can also be used to measure galaxy velocity dispersions  $\sigma_v$ . The motion

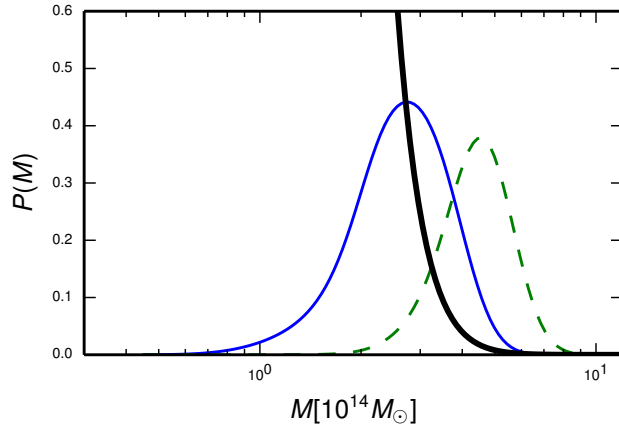


Figure 1.9 Illustration of how to obtain an unbiased mass estimate. The green dashed curve is obtained by directly inverting the mass-observable relation  $P(O|M)$  for a given observation  $O$ . The correct, unbiased mass estimate (Equation 1.22, blue solid curve) is obtained by multiplying with the mass function  $P(M)$  (thick black curve).

of galaxies, which nearly behave as non-interacting particles in the cluster potential well, can be well studied and calibrated in numerical simulations (e.g., Evrard et al. 2008; Saro et al. 2013). Using dispersions as a mass proxy is an interesting and complementary method to the following two methods because it is independent of the physics of the ICM. We will discuss mass calibration from  $\sigma_v$  in detail in Chapter 2.

### 1.2.3 X-ray Observations

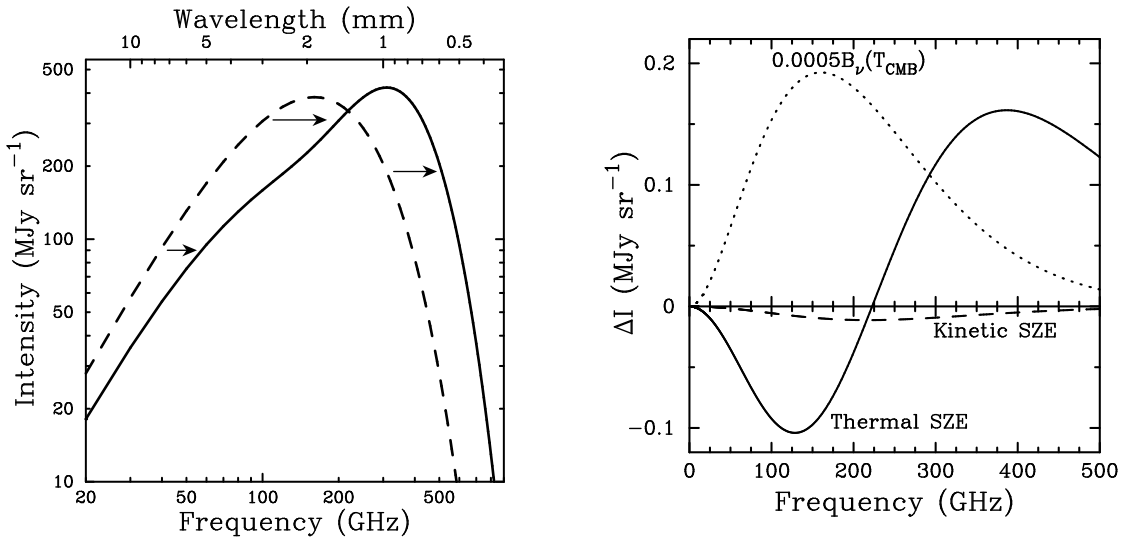
Most of the ordinary matter contained in a cluster is inter galactic gas, the so called intracluster medium (ICM). As it falls into the deep gravitational well of the cluster, the gas is heated to  $\sim$  keV temperatures. The emitted Bremsstrahlung can therefore be detected in the X-ray. The observationally cheapest X-ray observable is the luminosity  $L_X$  which can be obtained down to very low photon counts  $\sim 50$  and is therefore a suitable survey observable (e.g., for eROSITA, Pillepich et al. 2012). However, at fixed cluster mass, the luminosity quickly drops with redshift and a  $L_X$ -selected sample is therefore restricted to rather low redshifts  $z \lesssim 0.8$ .

In the present work, we focus on another X-ray observable:  $Y_X$  which is the product of the gas mass  $M_g$  with the temperature  $T_X$ . The  $Y_X$  observable is ideally suited as a follow-up measurement because it tightly correlates with cluster mass with small scatter in mass  $\sigma_M \simeq 0.07$  (Vikhlinin et al. 2009b).

### 1.2.4 The Sunyaev-Zel'dovich Effect

Another technique of observing the ICM is through the (thermal) Sunyaev-Zel'dovich effect (SZE, Sunyaev & Zel'dovich 1972): CMB photons passing through the hot ICM eventually gain energy by inverse Compton scattering off thermal electrons which leads to a characteristic distortion of the CMB spectrum at the location of the cluster. This is illustrated in Figure 1.10. To first order, the net effect is a slight blue-shift of the black-body spectrum of the CMB. The resulting distortion of the CMB spectrum is shown in the right panel.

In a high-resolution image of the CMB, one can indeed detect a galaxy cluster as a “shadow” in frequency bands  $< 218$  GHz, and as a bright spot at higher frequencies; there is no SZE signal at 218 GHz. Such surveys have been carried out by the South Pole Telescope (SPT, Carlstrom et al. 2011), the Atacama Cosmology Telescope (ACT, Fowler et al. 2007), and the *Planck* satellite (Planck Collaboration et al. 2011). Three of the



(a) Undistorted CMB spectrum (dashed) and CMB spectrum distorted by the presence of a cluster (solid). Note that the effect is dramatically exaggerated for illustrational purposes.

(b) Spectral distortion of the CMB by the SZ effect. The net effect of the thermal SZ effect vanishes at a characteristic frequency of  $\sim 218\text{GHz}$ .

Figure 1.10 Illustration of the Sunyaev-Zel'dovich effect as shown in Carlstrom et al. (2002).

studies presented here use data from the SPT, and we will discuss details of this survey together with these analyses in the main part of the thesis.

A key feature of using the SZE to detect clusters of galaxies is that the detection threshold in mass is in principle nearly redshift-independent. As a consequence, in a survey conducted with a telescope that provides sufficient angular resolution, all clusters above that mass threshold are detected out to the highest redshifts where clusters exist. This makes SZE-selected cluster samples particularly suitable for all studies that benefit from a large redshift leverage. These comprise cluster evolution studies and of course measurements of properties of dark energy and growth of structure.

### 1.3 Parameter Estimation

In the studies presented in this thesis we face multi-dimensional spaces of fit parameters  $\mathbf{p}$ . Given some data and a model – either phenomenological or predicted from theory – we would like to know what parameter set  $\mathbf{p}$  best describes the data. In a cosmological context, the default fit parameters would be the set of six base parameters describing the  $\Lambda\text{CDM}$  model. Adding the parameters of the scaling relations for three different observables one can easily end up with 20 or more free parameters. As a further complication, we do not only want to know the set of best-fitting parameters, but we are also interested in the uncertainties on each parameter.

The first ingredient for such a fit is the likelihood function  $\mathcal{L}$ , telling how well the set of parameters  $\mathbf{p}$  fits the data. The likelihood function is equivalent to the probability of the data given  $\mathbf{p}$ . In practice, we will consider Gaussian and Poisson processes, and then  $\mathcal{L}$  is simply a Gaussian or Poisson distribution centered on the theoretical prediction.

In order to obtain best-fitting values and confidence intervals for  $N$  parameters, it is in principle as simple as evaluating the likelihood of each point  $\mathbf{p}$  on a  $N$ -dimensional parameter grid. However, in a cosmological analysis, the evaluation of the likelihood of a single point  $\mathbf{p}$  takes between 1–10 seconds (depending on the implementation it can easily take a factor few times longer). Assuming a 10-dimensional parameter space, and applying a modestly resolved grid with 20 bins in each direction, the calculation will take at least  $20^{10} \times 1 \text{ sec}$  or

over 32,470 years. As the goal is to obtain a PhD within about  $10^{-4}$  of this time scale, more efficient sampling methods are needed. The weakness of the proposed sampling method is that every region of the parameter space gets sampled with the same density of points. However, we are in fact only interested in the  $\sim 99\%$  confidence region or so. We therefore need a sampling method that cleverly distributes points in the region of high likelihood without wasting time on low-likelihood parts of parameter space. It is then sufficient to only obtain of the order of  $10^4 - 10^5$  sample points, which already represents a factor  $\sim 10^8$  speed-up compared to the naive example just discussed. In the next subsections, I will briefly discuss three such methods. In practice, the density of points sampled by each algorithm is proportional to the likelihood; sometimes an additional weight is assigned to each point.

My experience during this thesis has shown that every fit will be repeated a significant number of times prior to obtaining the final result, which will be presented in the publication. These repetitions are not only due to debugging and code testing, but also to different data combinations that one might wish to consider. I would therefore argue that any fit that takes longer than 24 hours is too slow. Throughout my thesis I have used three different sampling algorithms and spent a significant amount of time understanding, implementing, and testing them. I therefore find it useful to present a brief overview, highlighting basic features as well as advantages and disadvantages of each method. Note that this comparison necessarily contains some level of personal taste.

### 1.3.1 Markov Chain Monte Carlo: Metropolis-Hastings algorithm

The Markov chain Monte Carlo (MCMC) method is probably the most basic, yet very popular sampling algorithm: Assuming that the chain is currently at the point  $\mathbf{p}_0$  of likelihood  $\mathcal{L}_0$ , draw a proposal  $\mathbf{p}'$  and calculate its likelihood  $\mathcal{L}'$  as well as  $R \equiv \mathcal{L}'/\mathcal{L}_0$ . Draw a random number  $r \sim [0, 1]$ . If  $R > r$ , accept  $\mathbf{p}'$  as the next step in the chain, else reject  $\mathbf{p}'$  and draw a new proposal. In other words, if the new point has a higher likelihood than the current one, then it is accepted, otherwise, there is still a chance to keep it depending on the ratio  $R/r$ .

After a sufficient number of steps – typically thousands or tens of thousands depending on the dimensionality and complexity of the target distribution – the chain will have become stationary. The accepted points are then a fair sampling of the target likelihood distribution and their density can be used to extract marginalized confidence intervals. The acceptance rate can be tuned by providing a suitable proposal distribution that will favor new proposals to be drawn from a region of high likelihood.

The main inconvenience of this algorithm is that it is hardly parallelizable, because each proposal point needs to be considered at a time. Obviously, one can speed up the likelihood evaluation itself, but typically one can only achieve a speed-up by a factor  $\sim 10$  (factor 8 for CAMB, which is the main bottleneck in the analyses performed in this thesis).

### 1.3.2 Population Monte Carlo

For the first work presented in this thesis I used the Population Monte Carlo (PMC) method as implemented in the CosmoPMC<sup>3</sup> code (Kilbinger et al. 2011). The PMC method is an iterative process: In each iteration, a large sample of trial points (a population of  $O(10^3 - 10^4)$  points) is spread across the parameter space according to some proposal distribution. Then, the likelihood of each trial point of the population is calculated. This task can be performed in parallel, since the individual likelihood evaluations are independent. Then, the calculated likelihood of each member of the population is compared to the probability of this point according to the proposal distribution, and the proposal distribution is updated. The updated proposal distribution is used to create a new population for the next iteration. The overall convergence can be estimated for each iteration by comparing the ratio of the calculated likelihood to the proposal likelihood for each trial point. If this ratio is constant or close to constant throughout the whole population, then the proposal and target distributions are basically identical: the algorithm has converged. Typically, this happens after a few iterations.

<sup>3</sup><http://www2.iap.fr/users/kilbinge/CosmoPMC/>

The obvious advantage of this method is that the slowest part in the process can be run in parallel on a big computing cluster, speeding up the overall run time by orders of magnitudes. However, the performance of this method critically depends on the accuracy of the proposal distribution. Since the proposal is updated by an importance sampling technique, it is mandatory that the proposal has significant overlap with the target likelihood distribution at the  $1\sigma$  level roughly. The initial proposal can be estimated by a Fisher matrix approach.

For target likelihood distributions that are Gaussian or reasonably close to Gaussian, the PMC is extremely efficient in quickly producing a large number of sample points that can be used for parameter estimations. I successfully ran PMC codes for up to 30 dimensions. In principle, the code can be run on as many CPU cores as there are sample points in each population, and, together with a good initial proposal distribution, the runtime on the wall clock can be as short as tens of minutes.

However, I did encounter limitations of this method when the posterior distributions were not Gaussian; narrow, bent degeneracies between parameters were particularly problematic. In these cases, the proposal update by importance sampling does not work as well as in the Gaussian case, and convergence can be very slow.

### 1.3.3 Affine Invariant Ensemble Sampling

Another approach is the so called affine invariant ensemble sampling, as implemented in the `emcee`<sup>4</sup> code (Foreman-Mackey et al. 2013). The ensemble consists of a large number of typically hundreds of so-called walkers. The proposal distribution of walker  $i$  is then given by the distribution of all other walkers, and every walker is subject to an acceptance-rejection procedure similar to the Metropolis-Hastings method. This procedure is repeated for each walker over and over again until the required number of sample points in the chain is reached. A slight modification to the method just described allows this code to be run in parallel with as many separate processes as there are walkers in the ensemble.

This algorithm has two main advantages: 1) It is extremely robust and performs well for arbitrarily shaped posterior distributions because it does not assume any functional form for the proposal. Remember that the proposal distribution is given by the current position of all walkers themselves and is therefore updated at each step. 2) It can be run in parallel on hundreds of CPU cores. By the time I am writing this thesis I have updated and reorganized all my codes and am using `emcee` for all parameter fits. According to my personal experience it outperforms both the standard MCMC and PMC methods. More discussion can also be found in Foreman-Mackey et al. (2013) and references therein.

## 1.4 Conclusions and Outlook

In this introduction, we have reviewed the basic ingredients of cluster cosmology. In particular, we discussed the foundation of modern cosmology and showed that the abundance of galaxy clusters is deeply linked to several key properties. With this background knowledge we are now ready to focus on some particular aspects, which are discussed in the scientific work presented in the main part of this thesis.

In the first study we use an SZE-selected cluster sample from the SPT survey to constrain cosmology. As anticipated, the limiting factor in such an analysis is the systematic uncertainty in cluster masses. This work uses two types of mass calibration data: X-ray  $Y_X$  measurements, and cluster galaxy velocity dispersions  $\sigma_v$ . First, we discuss in detail how such a multi-wavelength cluster cosmology analysis is conducted and introduce the analysis method. This builds upon the introduction given in Section 1.2.1. Then, we compare how the choice of the mass calibration dataset (or their combination) affects the recovered cosmological results. We compare our cluster-based results to constraints from CMB anisotropy measurements and find them to be in agreement. As anticipated in Figure 1.8, the combination of the different cosmological probes leads to tighter joint constraints. Finally, we consider some extensions of the baseline  $\Lambda$ CDM cosmological model. This work bridges the gap between astrophysical properties of clusters and cosmology.

---

<sup>4</sup><http://dan.iel.fm/emcee/current/>

The second study is dedicated to measuring optical properties of SPT-selected galaxy clusters found in the Dark Energy Survey (DES) science verification data. In particular, we focus on the optical richness, which essentially is the number of cluster member galaxies. After discussing the catalog matching algorithm, we establish a richness-mass scaling relation and calibrate its parameters against mass estimates derived from the SZE. Once more, this step crucially relies on correcting for selection effects as illustrated in Figure 1.9. We finally compare the cluster positions in the optical and SZE and measure the offset distribution. This study is an important step towards using large, high-quality optical datasets that will be available in the very near future. It demonstrates once more how multi-wavelength survey data are useful for performing cross-comparisons like the one presented here.

The third analysis builds upon the methods and tools developed for the first project, and we now use the full SPT-SZ survey data to constrain cosmology. This work focuses specifically on constraints on the growth of cosmic structure. Assuming a flat  $\Lambda$ CDM cosmology, we find our growth measurement to be in good agreement with the prediction from General Relativity. Going one step further, we also allow the dark energy equation of state parameter to vary, and thus constrain both the expansion and growth histories of the Universe. We do not find any evidence for departure from the  $\Lambda$ CDM model.

Finally, in a fourth, theoretical project, we focus on the halo mass function itself. As discussed earlier, the commonly used fitting functions are calibrated against  $N$ -body simulations and baryons are neglected. However, one does expect – and this has been shown previously – that baryonic effects play a role at least in low-mass clusters and groups. However, typical hydrodynamic simulations do not yet cover enough volume to provide reliable statistics for the most massive and therefore rarest systems. In this study, we use the largest hydrodynamic simulations available to date to provide a fitting function that takes cluster baryons properly into account. We discuss technical and theoretical aspects of the fitting procedure. In particular, we argue that the functional form of the fit should depend on the halo mass definition to provide a universal description that is independent of redshift and cosmology. We then compare our new established fit with previous work. Baryonic effects will have to be accounted for in the next-generation of cluster surveys that will extend to lower cluster masses. Neglecting this baryonic impact could then lead to biases that are as large as the overall expected error budget.

Together, these four studies cover a sizable range of topics in the vast area of cluster cosmology. In particular, they represent an important step towards using cluster data obtained from different observational methods to perform multi-wavelength studies that will play an important role in the future of cluster cosmology.



# Mass Calibration and Cosmology

In the following, three studies related to cluster mass calibration and cosmology are presented. The studies all use data from the South Pole Telescope, and each focuses on another specific aspect. First, a comprehensive multi-wavelength mass calibration and cosmological analysis is presented as published in ApJ (Bocquet et al. 2015b). In the second study, we compare optical richness measurements with cluster properties in the SZE. This work is to be submitted to MNRAS (Saro, Bocquet, et al. in preparation). Finally, we present a study of the full SPT cluster data set which we use to put tight constraints on cosmic growth (Bocquet et al., in preparation).



## Chapter 2

# Mass calibration and cosmological analysis of the SPT-SZ galaxy cluster sample using velocity dispersion $\sigma_v$ and X-ray $Y_X$ measurements

**S. Bocquet**, A. Saro, J. J. Mohr, K. A. Aird, M. L. N. Ashby, M. Bautz, M. Bayliss, G. Bazin, B. A. Benson, L. E. Bleem, M. Brodwin, J. E. Carlstrom, C. L. Chang, I. Chiu, H. M. Cho, A. Clocchiatti, T. M. Crawford, A. T. Crites, S. Desai, T. de Haan, J. P. Dietrich, M. A. Dobbs, R. J. Foley, W. R. Forman, C. Gangkofner, E. M. George, M. D. Gladders, A. H. Gonzalez, N. W. Halverson, C. Hennig, J. Hlavacek-Larrondo, G. P. Holder, W. L. Holzapfel, J. D. Hrubes, C. Jones, R. Keisler, L. Knox, A. T. Lee, E. M. Leitch, J. Liu, M. Lueker, D. Luong-Van, D. P. Marrone, M. McDonald, J. J. McMahon, S. S. Meyer, L. Mocanu, S. S. Murray, S. Padin, C. Pryke, C. L. Reichardt, A. Rest, J. Ruel, J. E. Ruhl, B. R. Saliwanchik, J. T. Sayre, K. K. Schaffe, E. Shirokoff, H. G. Spieler, B. Stalder, S. A. Stanford, Z. Staniszewski, A. A. Stark, K. Story, C. W. Stubbs, K. Vanderlinde, J. D. Vieira, A. Vikhlinin, R. Williamson, O. Zahn, and A. Zenteno  
2015, *The Astrophysical Journal (ApJ)*, 799, 214

### ABSTRACT

We present a velocity dispersion-based mass calibration of the South Pole Telescope Sunyaev-Zel'dovich effect survey (SPT-SZ) galaxy cluster sample. Using a homogeneously selected sample of 100 cluster candidates from  $720 \text{ deg}^2$  of the survey along with 63 velocity dispersion ( $\sigma_v$ ) and 16 X-ray  $Y_X$  measurements of sample clusters, we simultaneously calibrate the mass-observable relation and constrain cosmological parameters. Our method accounts for cluster selection, cosmological sensitivity, and uncertainties in the mass calibrators. The calibrations using  $\sigma_v$  and  $Y_X$  are consistent at the  $0.6\sigma$  level, with the  $\sigma_v$  calibration preferring  $\sim 16\%$  higher masses. We use the full SPT<sub>CL</sub> dataset (SZ clusters+ $\sigma_v$ + $Y_X$ ) to measure  $\sigma_8(\Omega_m/0.27)^{0.3} = 0.809 \pm 0.036$  within a flat  $\Lambda$ CDM model. The SPT cluster abundance is lower than preferred by either the WMAP9 or *Planck*+WMAP9 polarization (WP) data, but assuming the sum of the neutrino masses is  $\sum m_\nu = 0.06 \text{ eV}$ , we find the datasets to be consistent at the  $1.0\sigma$  level for WMAP9 and  $1.5\sigma$  for *Planck*+WP. Allowing for larger  $\sum m_\nu$  further reconciles the results. When we combine the SPT<sub>CL</sub> and *Planck*+WP datasets with information from baryon acoustic oscillations and supernovae Ia, the preferred cluster masses are  $1.9\sigma$  higher than the  $Y_X$  calibration and  $0.8\sigma$  higher than the  $\sigma_v$  calibration. Given the scale of these shifts ( $\sim 44\%$  and  $\sim 23\%$  in mass, respectively), we execute a goodness of fit test; it reveals no tension, indicating that the best-fit model provides an adequate description of the data. Using the multi-probe dataset, we measure  $\Omega_m = 0.299 \pm 0.009$  and  $\sigma_8 = 0.829 \pm 0.011$ . Within a  $\nu$ CDM model we find  $\sum m_\nu = 0.148 \pm 0.081 \text{ eV}$ . We present a consistency test of the cosmic growth rate using SPT clusters. Allowing both the growth index  $\gamma$  and the dark energy equation of state parameter  $w$  to vary, we find  $\gamma = 0.73 \pm 0.28$  and  $w = -1.007 \pm 0.065$ , demonstrating that the expansion and the growth histories are consistent with a  $\Lambda$ CDM Universe ( $\gamma = 0.55$ ;  $w = -1$ ).

**Key words:** cosmic background radiation — cosmology: observations — galaxies: clusters: individual — large-scale structure of universe

## 2.1 Introduction

Galaxy cluster surveys provide important insights into cosmological questions such as the nature of cosmic acceleration (Wang & Steinhardt 1998; Haiman et al. 2001; Holder et al. 2001; Battye & Weller 2003; Molnar et al. 2004; Wang et al. 2004; Lima & Hu 2007), the Gaussian character of underlying density perturbations (Dalal et al. 2008; Cayón et al. 2011; Williamson et al. 2011) and the cosmic growth rate (Rapetti et al. 2013). Because their distribution in mass and redshift depends on both the geometry of the Universe and the growth rate of structure, galaxy clusters are complementary to distance-based probes such as Type Ia Supernovae (e.g., Sullivan et al. 2011) and Baryon Acoustic Oscillations (e.g., Percival et al. 2010). Indeed, recent studies demonstrate the constraining power of galaxy clusters using real cluster samples in X-ray (e.g., Vikhlinin et al. 2009b; Mantz et al. 2010b), optical (e.g., Rozo et al. 2010) and Sunyaev-Zel'dovich effect (SZE; e.g., Vanderlinde et al. 2010; Sehgal et al. 2011; Benson et al. 2013; Reichardt et al. 2013; Hasselfield et al. 2013; Planck Collaboration et al. 2014c) surveys.

Today, the largest available cluster catalogs come from X-ray and optical surveys. However, galaxy clusters can also be detected through their thermal SZE signature, which arises from the interaction of the cosmic microwave background (CMB) photons with the hot, ionized intracluster medium (Sunyaev & Zel'dovich 1972). The surface brightness of the SZE signature is independent of redshift, and the integrated signature is expected to be a low-scatter mass proxy (Barbosa et al. 1996; Holder et al. 2001; Motl et al. 2005; Nagai et al. 2007; Stanek et al. 2010). Therefore, SZE cluster surveys with sufficient angular resolution are expected to generate nearly mass-limited samples extending to the highest redshifts at which clusters exist. Dedicated millimeter-wave SZE surveys over large areas of the sky are being carried out by the South Pole Telescope (SPT, Carlstrom et al. 2011), the Atacama Cosmology Telescope (Fowler et al. 2007), and *Planck* (Planck Collaboration et al. 2011).

The first cosmological analysis of an SPT cluster sample used 21 clusters selected from 178 deg<sup>2</sup> of survey data (Vanderlinde et al. 2010). The observed SPT signal-to-noise  $\xi$  was used as a proxy for cluster mass, assuming a relationship that was calibrated from simulations. Using the same cluster sample, Benson et al. (2013) repeated the cosmological analysis using additional mass calibration from the X-ray observable  $Y_X \equiv M_g T_X$ , where  $M_g$  is the intracluster gas mass and  $T_X$  is the X-ray temperature. The X-ray data were obtained for a sub-sample of 14 clusters using *Chandra* and *XMM-Newton* (Andersson et al. 2011). The combination of the cluster abundance measurements with CMB anisotropy data improved constraints on  $\Omega_m$  and  $\sigma_8$  by a factor of 1.5 over the results from CMB data alone (WMAP7, Komatsu et al. 2011). Most recently, Reichardt et al. (2013) analyzed a sample of 100 cluster candidates extracted from the first 720 deg<sup>2</sup> of the SPT-SZ survey, including X-ray data on the same 14 clusters. The uncertainty in the derived cosmological constraints was dominated by the systematic uncertainties in the mass calibration of the sample.

Given the importance of the cluster mass calibration, the SPT collaboration has undertaken a comprehensive follow-up program to make use of multiple mass measurement techniques to better characterize the SPT mass-observable relation. Our strategy is to obtain direct mass constraints from X-ray observations and cluster velocity dispersions, and these will be supplemented with mass constraints from weak lensing in future studies. Both velocity dispersions and weak lensing exhibit significant uncertainties on individual cluster mass measurements but can be studied in detail using *N*-body studies of structure formation in order to characterize and correct for the systematic biases (e.g., White et al. 2010; Becker & Kravtsov 2011; Saro et al. 2013). Therefore, large ensembles of these measurements can be combined to deliver precise and accurate mass information. In a complementary fashion, the X-ray mass proxy  $Y_X$  is tightly correlated with the cluster virial mass, and can be calibrated using weak lensing or velocity dispersions to provide accurate and reasonably precise single cluster mass measurements (e.g., Sun et al. 2009; Vikhlinin et al. 2009a; Mantz et al. 2010a). In addition, we expect the small scatter X-ray observable to play an important role as we want to constrain not only the masses of our SPT clusters, but also the scatter about the SPT mass-observable relation. The latter plays a central role in the SPT cluster survey selection, and is critically important for the cosmological interpretation of the sample (e.g., Lima & Hu 2005).

In this work, we report a detailed analysis of the SZE mass-observable relation calibration using the cluster sample of the 720 deg<sup>2</sup> SPT-SZ survey together with a subset of 64 SZE detected galaxy clusters with additional spectroscopic and/or X-ray observations. The cluster sample with its mass calibration data and external cosmological datasets are described in Section 2.2. In Section 2.3 we summarize how velocity dispersions are used as mass calibrators, and largely follow the recent theoretical exploration of this issue (Saro et al. 2013). We present our analysis method in Section 2.4, and show how we tested it on simulated data. In Section 2.5 we compare the X-ray and velocity dispersion constraints. Because they are in good agreement, we combine them and present our best current constraints from SPT clusters alone assuming a flat  $\Lambda$ CDM model, showing that these results are in agreement with constraints from external datasets. We then carry out a joint cosmological analysis that combines our SPT clusters with external data to deliver the tightest constraints on cluster masses and cosmological parameters. We also explore constraints on the sum of the neutrino masses, cosmic growth, and the Dark Energy equation of state parameter  $w$ . We review our conclusions in Section 2.6.

In this work, unless otherwise specified, we assume a flat  $\Lambda$ CDM cosmology with massless neutrinos. Cluster masses refer to  $M_{500,c}$ , the mass enclosed within a sphere of radius  $r_{500}$ , in which the mean matter density is equal to 500 times the critical density. The critical density at the cluster's redshift is  $\rho_{\text{crit}}(z) = 3H^2(z)/8\pi G$ , where  $H(z)$  is the Hubble parameter.

## 2.2 Observations and Data

### 2.2.1 South Pole Telescope Observations, Cluster Catalog, and Scaling Relations

The SPT is a 10 m telescope located within 1 km of the geographical South Pole. From 2007 to 2011, the telescope was configured to observe in three millimeter-wave bands (centered at 95, 150, and 220 GHz). The majority of this period was spent on a survey of a contiguous 2500 deg<sup>2</sup> area within the boundaries 20h  $\leq$  R.A.  $\leq$  7h and  $-65^\circ \leq$  Dec.  $\leq -40^\circ$ , which we term the SPT-SZ survey. The survey was completed in November 2011, and achieved a fiducial depth of 18  $\mu$ K-arcmin in the 150 GHz band. Details of the survey strategy and data processing can be found in Schaffer et al. (2011).

Galaxy clusters are detected via their thermal SZE signature in the 95 and 150 GHz maps. These maps are created using time-ordered data processing and map-making procedures equivalent to those described in Vanderlinde et al. (2010), and clusters are extracted from the multi-band data as in Williamson et al. (2011); Reichardt et al. (2013). A multi-scale matched-filter approach is used for cluster detection (Melin et al. 2006). The observable of the cluster SZE signal is  $\xi$ , the detection significance maximized over all filter scales. Because of the impact of noise biases, a direct scaling relation between  $\xi$  and cluster mass is difficult to characterize. Therefore, an unbiased SZE significance  $\zeta$  is introduced, which is the signal-to-noise at the true, underlying cluster position and filter scale (Vanderlinde et al. 2010). For  $\zeta > 2$ , the relationship between  $\xi$  and  $\zeta$  is given by

$$\zeta = \sqrt{\langle \xi \rangle^2 - 3}. \quad (2.1)$$

The unbiased significance  $\zeta$  is related to mass  $M_{500,c}$  by

$$\zeta = A_{\text{SZ}} \left( \frac{M_{500,c}}{3 \times 10^{14} M_\odot h^{-1}} \right)^{B_{\text{SZ}}} \left( \frac{E(z)}{E(0.6)} \right)^{C_{\text{SZ}}} \quad (2.2)$$

where  $A_{\text{SZ}}$  is the normalization,  $B_{\text{SZ}}$  the mass slope,  $C_{\text{SZ}}$  the redshift evolution parameter and  $E(z) \equiv H(z)/H_0$ . An additional parameter  $D_{\text{SZ}}$  describes the intrinsic scatter in  $\zeta$  which is assumed to be log-normal and constant as a function of mass and redshift. The scaling parameters and the priors we adopt are summarized in Table 2.1, and further discussed in Section 2.4.3.

Table 2.1  $\Lambda$ CDM constraints from SZE cluster number counts  $N(\xi, z)$  with mass calibration from  $Y_X$  and  $\sigma_8$ , CMB and additional cosmological probes.

Param.	Prior	$N(\xi, z)$	$N(\xi, z) + \text{BBN} + H_0 +$	$Y_X + \sigma_v$	WMAP9	$\text{SPT}_{\text{CL}} + \text{WMAP9}$	$P_{\text{Planck}} + \text{WP}$	$\text{SPT}_{\text{CL}} + P_{\text{Planck}} + \text{WP}$	$+ \text{BAO} + \text{SNIa}$	$+ \text{BAO} + \text{SNIa}$
$A_{\text{SZ}}$	$6.24 \pm 1.87$	$6.49^{+2.08}_{-1.89}$	$5.59^{+1.19}_{-1.69}$	$4.38^{+1.05}_{-1.45}$	$4.70^{+0.82}_{-1.24}$	...	...	$3.79^{+0.57}_{-0.63}$	$3.47 \pm 0.48$	$3.27 \pm 0.35$
$B_{\text{SZ}}$	$1.33 \pm 0.266$	$1.54 \pm 0.16$	$1.56 \pm 0.13$	$1.65 \pm 0.14$	$1.58 \pm 0.12$	...	$1.47 \pm 0.11$	$1.48 \pm 0.11$	$1.49 \pm 0.11$	$1.49 \pm 0.11$
$C_{\text{SZ}}$	$0.83 \pm 0.415$	$0.75 \pm 0.39$	$0.82 \pm 0.35$	$0.92 \pm 0.37$	$0.91 \pm 0.35$	...	$0.40 \pm 0.23$	$0.44 \pm 0.23$	...	$0.44 \pm 0.21$
$D_{\text{SZ}}$	$0.24 \pm 0.16$	$0.32 \pm 0.16$	$0.28 \pm 0.11$	$0.24^{+0.11}_{-0.14}$	$0.26 \pm 0.10$	...	$0.25 \pm 0.10$	$0.27 \pm 0.10$	...	$0.26 \pm 0.05$
$A_X$	$5.77 \pm 0.56$	...	$5.40 \pm 0.56$	...	$5.76 \pm 0.50$	...	$5.79 \pm 0.43$	$5.94 \pm 0.43$	...	$6.10 \pm 0.42$
$B_X$	$0.57 \pm 0.03$	...	$0.547 \pm 0.030$	...	$0.545 \pm 0.030$	...	$0.548 \pm 0.029$	$0.549 \pm 0.029$	...	$0.546 \pm 0.029$
$C_X$	$-0.40 \pm 0.20$	...	$-0.37 \pm 0.18$	...	$-0.28 \pm 0.17$	...	$-0.24 \pm 0.17$	$-0.21 \pm 0.17$	...	$-0.17 \pm 0.16$
$D_X$	$0.12 \pm 0.08$	...	$0.15 \pm 0.07$	...	$0.15 \pm 0.07$	...	$0.14 \pm 0.07$	$0.14 \pm 0.07$	...	$0.14 \pm 0.07$
$A\sigma_v [\text{km s}^{-1}]$	$939 \pm 47$	...	...	$971^{+47}_{-43}$	$984 \pm 39$	...	$973 \pm 35$	$961 \pm 35$	...	$948 \pm 34$
$B\sigma_v$	$2.91 \pm 0.15$	...	...	$2.91 \pm 0.16$	$2.92 \pm 0.16$	...	$2.92 \pm 0.15$	$2.92 \pm 0.16$	...	$2.92 \pm 0.16$
$C\sigma_v$	$0.33 \pm 0.02$	...	...	$0.330 \pm 0.021$	$0.331 \pm 0.021$	...	$0.329 \pm 0.021$	$0.329 \pm 0.020$	...	$0.327 \pm 0.021$
$D\sigma_{v0}$	$0.2 \pm 0.04$	...	...	$0.176 \pm 0.030$	$0.176 \pm 0.030$	...	$0.176 \pm 0.028$	$0.174 \pm 0.030$	...	$0.175 \pm 0.029$
$D\sigma_{v,\text{N}}$	$3 \pm 0.6$	...	...	$2.93 \pm 0.56$	$2.92 \pm 0.56$	...	$2.92 \pm 0.56$	$2.93 \pm 0.54$	...	$2.93 \pm 0.54$
$H_0 [\text{km s}^{-1} \text{Mpc}^{-1}]$	...	$73.5 \pm 2.4$	$73.2 \pm 2.5$	$73.4 \pm 2.4$	$73.2 \pm 2.6$	$70.0 \pm 2.4$	$70.1 \pm 1.7$	$68.6 \pm 1.0$	$67.6 \pm 1.2$	$68.3 \pm 1.1$
$\Omega_m$	...	$0.39^{+0.07}_{-0.13}$	$0.41^{+0.07}_{-0.14}$	$0.45^{+0.09}_{-0.16}$	$0.44^{+0.07}_{-0.15}$	$0.281 \pm 0.028$	$0.276 \pm 0.018$	$0.292 \pm 0.011$	$0.310 \pm 0.017$	$0.297 \pm 0.014$
$\sigma_8$	...	$0.67 \pm 0.07$	$0.69 \pm 0.06$	$0.72 \pm 0.07$	$0.71 \pm 0.06$	$0.825 \pm 0.027$	$0.812 \pm 0.017$	$0.816 \pm 0.016$	$0.841 \pm 0.013$	$0.828 \pm 0.011$
$\sigma_8 \left( \frac{\Omega_m}{0.27} \right)^{0.3}$	...	$0.741 \pm 0.064$	$0.774 \pm 0.040$	$0.831 \pm 0.052$	$0.809 \pm 0.036$	$0.835 \pm 0.051$	$0.817 \pm 0.027$	$0.835 \pm 0.022$	$0.877 \pm 0.024$	$0.852 \pm 0.020$

Note. —  $N(\xi, z)$  denotes the cluster sample without additional mass calibration information;  $\text{SPT}_{\text{CL}}$  contains the clusters with the mass calibration data from X-ray  $Y_X$  and velocity dispersion  $\sigma_v$ . The priors are Gaussian as discussed in Section 2.4.3. We apply a prior  $H_0 = 73.8 \pm 2.4 \text{ km s}^{-1} \text{ Mpc}^{-1}$  when no CMB data are included in the fit. The scalar spectral index  $n_s$ , the reionization optical depth  $\tau$ , the baryon density  $\Omega_b$ , and the  $P_{\text{Planck}}$  nuisance parameters are not shown in this table but are included in the analysis and marginalized out. We fix  $\tau = 0.089$  when no CMB data are included in the fit.

We use SPT-selected clusters for the cosmological cluster number count and mass calibration analysis, described in Section 2.4. For the number counts, we use a cluster sample identical to the one used in Reichardt et al. (2013). This sample uses data from the first 720 deg<sup>2</sup> of the SPT-SZ survey and is restricted to  $\xi > 5$  and redshift  $z > 0.3$ ; it contains 100 cluster candidates. No optical counterparts were found for six of these SZE detections; we discuss their treatment in the analysis in Section 2.4.1. The SPT-SZ 720 deg<sup>2</sup> survey comprises 5 fields with different depths which are accounted for by rescaling the SPT  $\zeta$ -mass relation normalization  $A_{\text{SZ}}$  for each field (Reichardt et al. 2013). Our mass calibration data consists of a sub-sample of 64 SPT clusters with additional X-ray and/or spectroscopic follow-up data, as described in Section 2.2.3 and 2.2.4. Twenty-two clusters with velocity dispersion  $\sigma_v$  measurements lie outside the SPT-SZ 720 deg<sup>2</sup> survey. The depths of these fields and the corresponding scaling factors for  $A_{\text{SZ}}$  will be presented elsewhere together with the analysis of the full 2500 deg<sup>2</sup> survey catalog (de Haan et al. in preparation). These scaling factors are all between 1.08 – 1.27 with a median value of 1.17.

## 2.2.2 Optical and Near-Infrared Imaging

The galaxy clusters analyzed here have been followed up in optical and near infrared in the context of the SPT follow-up program, as described in Song et al. (2012a), to which we refer the reader for details of the strategy and data reduction. Briefly, the SPT strategy is to target all galaxy clusters detected at SZE significance  $\xi > 4.5$  for multiband imaging in order to identify counterparts to the SZE signal and obtain photometric redshifts. We also obtain *Spitzer*/IRAC near-infrared imaging for every cluster with SZE significance  $\xi > 4.8$ , and we target those systems at lower  $\xi$  which are not optically confirmed or have a redshift above 0.9 with ground based near infrared imaging using the NEWFIRM imager on the CTIO Blanco 4 m telescope.

## 2.2.3 Optical Spectroscopy

We use follow-up optical spectroscopy to measure the velocity dispersion  $\sigma_v$  of 63 clusters. Of these, 53 were observed by the SPT team (Ruel et al. 2014) and 10 have data taken from the literature (Barrena et al. 2002; Buckley-Geer et al. 2011; Sifón et al. 2013). In Ruel et al. (2014), four additional clusters with spectroscopic data are listed, but we choose not to include them in our analysis as they are all at relatively low redshifts below  $z < 0.1$  where the SZE mass-observable scaling relation we adopt is likely not valid. The lowest redshift cluster entering our mass calibration analysis is SPT-CL J2300-5331 at  $z = 0.2623$ .

Our own data come from a total observation time of  $\sim 70$  h on the largest optical telescopes (Gemini South, Magellan, and VLT) in the southern hemisphere; we specifically designed these observations to deliver the data needed for this velocity dispersion mass calibration study. We obtained low-resolution ( $R \simeq 300$ ) spectra using several different instruments: GMOS<sup>1</sup> on Gemini South, FORS2 (Appenzeller et al. 1998) on VLT Antu, LDSS3 on Magellan Clay and IMACS/Gladders Image-Slicing Multislit Option (GISMO<sup>2</sup>) on Magellan Baade.

Apart from early longslit spectroscopy using the Magellan LDSS3 spectrograph on a few SPT clusters, the general strategy is to design two masks per cluster for multi-object spectroscopy to get a final average number of 25 member galaxy redshifts per cluster. We typically obtained deep ( $m^* + 1$ ) pre-imaging in  $i'$ -band for spectroscopic observation to (1) accurately localize galaxies to build masks for multi-object spectroscopy, and (2) identify possible giant arcs around cluster cores. This deep pre-imaging is used together with existing shallower optical imaging and near infrared photometry, where available, to select galaxy cluster members along the red sequence. We refer the reader to Ruel et al. (2014) for a detailed description of the cluster member selection and the data reduction.

---

<sup>1</sup><http://www.gemini.edu/node/10625>

<sup>2</sup><http://www.lco.cl/telescopes-information/magellan/instruments/imacs/gismo/gisomoquickmanual.pdf>

### 2.2.4 X-ray Observations and $Y_X$ Scaling Relation Parametrization

Sixteen clusters of our sample have been observed in X-ray using either *Chandra* or *XMM-Newton*. The derived properties of 15 of these clusters are published in Andersson et al. (2011). This sub-sample corresponds to the highest SZE significance clusters in the first 178 deg<sup>2</sup> of the SPT-SZ survey that lie at  $z \gtrsim 0.3$ . We obtained *Chandra* observations of SPT-CL J2106-5844 in a separate program whose results are published elsewhere (Foley et al. 2011). All of these observations have  $> 1500$  source photons within  $0.5 \times r_{500}$  and in the 0.5–7.0 keV energy band. X-ray observations are used to derive the intracluster medium temperature  $T_X$  and the gas mass  $M_g$ . For a detailed description of the data reduction method, we refer the reader to Andersson et al. (2011). Note that there is a calibration offset between temperature measurements from the two satellites (Schellenberger et al. 2014). For our analysis, we adopt priors on the  $Y_X$ -mass relation that come from an analysis of *Chandra* data. Given that only 2/16 systems in this study rely on *XMM-Newton* data, and the amplitude of the calibration offset is  $\sim 30\%$  in temperature for these massive clusters, we expect an overall temperature bias of  $\sim 4\%$ , corresponding to a  $\sim 2\%$  bias in our mass scale, assuming that the *Chandra*-derived temperatures are unbiased. Given that this is much smaller than the systematic uncertainty in our  $Y_X$ -mass calibration, we neglect any cross-calibration.

Following Benson et al. (2013) we rely on the X-ray observable  $Y_X \equiv M_g T_X$ . For the cosmological analysis performed in this work we need to evaluate  $Y_X$  as a function of cosmology and scaling relation parameters. In practice, for a given set of cosmological and scaling relation parameters, we iteratively fit for  $r_{500}$  and  $Y_X(r)$  which is then used to estimate the cluster mass.

We adopt a calibrated scaling relation derived from hydrostatic masses at low redshifts (Vikhlinin et al. 2009a):

$$\frac{M_{500,c}}{10^{14} M_\odot} = A_X h^{1/2} \left( \frac{Y_X}{3 \times 10^{14} M_\odot \text{keV}} \right)^{B_X} E(z)^{C_X}, \quad (2.3)$$

where  $A_X$  is the normalization,  $B_X$  the slope and  $C_X$  the redshift evolution parameter. We assume an intrinsic log-normal scatter in  $Y_X$  denoted  $D_X$  and an observational log-normal uncertainty for each cluster. The fiducial values and priors we adopt for the  $Y_X$  parameters are discussed in Section 2.4.3 and shown in Table 2.1.

### 2.2.5 External Cosmological Datasets

In addition to our cluster sample, we include external cosmological datasets such as measurements of the CMB anisotropy power spectrum, the baryon acoustic oscillations (BAO), Type Ia Supernovae (SNIa), the Hubble constant ( $H_0$ ), and Big Bang nucleosynthesis (BBN). We use these abbreviations when including the datasets in the analysis. We refer to the SPT SZE cluster sample without the follow-up mass information as  $N(\xi, z)$  (which stands for the distribution of the clusters in  $\xi$ - $z$  space), and we refer to the full cluster sample with mass measurements from  $\sigma_v$  and  $Y_X$  as SPT<sub>CL</sub>.

We include measurements of the CMB anisotropy power spectrum from two all-sky surveys. We use data from the *Wilkinson Microwave Anisotropy Probe* (WMAP, 9-year release; Hinshaw et al. 2013) and data from the *Planck* satellite (1-year release, including WMAP polarization data (WP); Planck Collaboration et al. 2014a,b). The BAO constraints are applied as three measurements:  $D_V(z = 0.106) = 457 \pm 27$  Mpc (Beutler et al. 2011),  $D_V(z = 0.35)/r_s = 8.88 \pm 0.17$  (Padmanabhan et al. 2012), and  $D_V(z = 0.57)/r_s = 13.67 \pm 0.22$  (Anderson et al. 2012);  $r_s$  is the comoving sound horizon at the baryon drag epoch,  $D_V(z) \equiv [(1 + z)^2 D_A^2(z)cz/H(z)]^{1/3}$ , and  $D_A$  is the angular diameter distance. We include distance measurements coming from Type Ia supernovae using the Union2.1 compilation of 580 SNe (Suzuki et al. 2012). We adopt a Gaussian prior on the Hubble constant  $H_0 = 73.8 \pm 2.4$  km s<sup>-1</sup> Mpc<sup>-1</sup> from the low-redshift measurements from the *Hubble Space Telescope* (Riess et al. 2011). Finally we use a BBN prior from measurements of the abundance of <sup>4</sup>He and deuterium which we include as a Gaussian prior  $\Omega_b h^2 = 0.022 \pm 0.002$  (Kirkman et al. 2003). Note that both the BBN and  $H_0$  priors are only applied when analyzing the cluster samples without CMB data.

## 2.3 Velocity Dispersions $\sigma_v$ as Mass Calibrators

Multiple studies highlight the fact that the line-of-sight velocity dispersion of galaxies within clusters may be used to measure galaxy cluster masses (e.g., Biviano et al. 2006; Evrard et al. 2008; White et al. 2010; Munari et al. 2013; Saro et al. 2013). The motivation to use velocity dispersions as a mass probe for galaxy clusters stems from the fact that the galaxy dynamics are unaffected by the complex physics of the intracluster medium. Therefore, the dominant source of scatter and bias in the  $\sigma_v$ -mass scaling relation is related to gravitational dynamics of subhalos, an effect that can be studied using high-resolution  $N$ -body simulations. As we will discuss in Section 2.4.3, the systematic floor on dynamical mass, which is due to uncertainties in modeling the velocity bias, is currently of the order of 15% in mass (equivalent to 5% in  $\sigma_v$ ).

Saro et al. (2013) used the publicly available galaxy catalogs produced with the semi-analytic model (De Lucia & Blaizot 2007) from the Millennium simulation (Springel et al. 2005) to precisely characterize the  $\sigma_v$ -mass scaling relation as a function of parameters such as redshift, number of selected red-sequence galaxy cluster members and aperture size centered on the cluster. Their approach provides a mapping between  $\sigma_v$  and cluster mass that includes the effects of galaxy selection, departures from equilibrium and sample size, all of which can be used to interpret the velocity dispersions available for our SPT clusters. There are two important, but opposing effects that may lead to a potential bias: (1) dynamical friction, which biases the velocity dispersion low, and (2) interlopers, which for our selection tend to bias dispersions high. For our selection approach, these contributions effectively cancel, producing no net bias. The intrinsic scatter on an individual dynamical mass is typically 80% due to the random projection of the velocity ellipsoid along the line of sight and interlopers in the calculation of velocity dispersion.

Given the large mass uncertainty associated with the dispersion from an individual cluster, we use a large ensemble of dispersion measurements for our mass calibration analysis. Within this context, we should be able to constrain the normalization  $A_{\text{SZ}}$  of the SZE  $\xi$ -mass relation to a level where it is dominated by the 15% systematic uncertainty in the dispersion mass estimates. However, because the intrinsic scatter in the velocity dispersion scaling relation is much larger than the scatter in the SZE  $\xi$ -mass scaling relation, we do not expect to improve our constraints on the scatter of the SZE  $\xi$ -mass scaling relation using velocity dispersions.

We assume the scatter in  $\sigma_v$  to be uncorrelated with the scatter in SZE. In principle, cluster triaxiality might induce such a correlation; however, for our sample, the intrinsic scatter in  $\sigma_v$  is dominated by the effect of interlopers, which do not affect the SZE signal.

We adopt the mass-observable scaling relation for velocity dispersions  $\sigma_v$  presented in Saro et al. (2013):

$$M_{200,c} = \left( \frac{\sigma_v}{A_{\sigma_v} h_{70}(z)^{C_{\sigma_v}}} \right)^{B_{\sigma_v}} 10^{15} M_{\odot} \quad (2.4)$$

where  $M_{200,c}$  is the mass expressed relative to the critical density,  $A_{\sigma_v}$  is the normalization,  $B_{\sigma_v}$  the slope, and  $C_{\sigma_v}$  the redshift evolution parameter. We express the scatter in  $\sigma_v$  as a function of  $N_{\text{gal}}$ , the number of spectroscopically observed cluster galaxies. The scatter is described by a log-normal distribution of width

$$D_{\sigma_v} = D_{\sigma_v,0} + D_{\sigma_v,N}/N_{\text{gal}} \quad (2.5)$$

where  $D_{\sigma_v,0}$  and  $D_{\sigma_v,N}$  are two parameters extracted from the simulations. Given that the typical number of spectroscopically observed galaxies is small for our sample, this dependency of the scatter on  $N_{\text{gal}}$  is important for our analysis. The fiducial values and priors adopted for the parameters are discussed in Section 2.4.3 and shown in Table 2.1.

Note that the SZE and X-ray mass scaling relations are defined in terms of  $M_{500,c}$  whereas the dynamical mass is defined as  $M_{200,c}$ . The mass conversion is performed using the NFW profile (Navarro et al. 1997) and the Duffy et al. (2008) mass-concentration relation.

## 2.4 Analysis Method

In this Section we introduce the likelihood model adopted for analyzing the data. When combining the cluster experiment with other cosmological probes, we multiply the individual likelihoods. The multi-dimensional parameter fit varying all relevant cosmological and scaling relation parameters is performed using a Population Monte Carlo (PMC) algorithm as implemented in the CosmoPMC code (Kilbinger et al. 2011). In contrast to the widely used Markov Chain Monte Carlo (MCMC) method, which explores the parameter space based on an acceptance-rejection algorithm, the PMC algorithm iteratively fits for the posterior distribution using samples of points (populations) in parameter space. This leads to a significant reduction of computational time as (1) the calculations of the likelihood at individual points in parameter space are independent and therefore can be computed in parallel and (2) the overall efficiency is higher than when using MCMC as there are no rejected points. For a detailed description of the PMC algorithm and its comparison with MCMC see e.g., Wraith et al. (2009).

When analyzing the SPT<sub>CL</sub> sample without CMB data we fit for up to 18 parameters: 4 SZE, 4  $Y_X$ , 5  $\sigma_v$  scaling relation parameters, and 5 cosmological parameters ( $\sigma_8$ ,  $\Omega_m$ ,  $\Omega_b$ ,  $H_0$ ,  $n_s$ ); we fix the optical depth because it is not constrained by the data. When combining with the CMB dataset from WMAP we also include the optical depth  $\tau$  as a free parameter in the fit; when analyzing *Planck* data we include further nuisance parameters.

We finally describe the priors that we adopt for each of the mass-observable scaling relations and explain how we tested our code using mock data.

### 2.4.1 Likelihood Model

The cluster number count analysis in the SZE observable  $\xi$  can be separated from the additional mass calibration in an unbiased way. This approach allows for an easy comparison and combination of the different mass calibrators as we will discuss in Section 2.4.2. For a detailed derivation of our likelihood function, see Appendix.

#### Cluster Mass Function

At each point in the space of cosmological and scaling-relation parameters we use the Code for Anisotropies in the Microwave Background (CAMB, Lewis et al. 2000) to compute the matter power spectrum at 180 evenly spaced redshift bins between  $0.2 < z < 2$ . We then use the fitting function presented in Tinker et al. (2008) to calculate the cluster mass function  $dN/dM$  for 500 mass bins evenly distributed in log-space between  $10^{13.5} h^{-1} M_\odot \leq M \leq 10^{16} h^{-1} M_\odot$ . This fitting function is accurate at the 5% level across a mass range  $10^{11} h^{-1} M_\odot \leq M \leq 10^{15} h^{-1} M_\odot$  and for redshifts  $z \leq 2.5$ .

We move the mass function from its native mass and redshift space to the observable space in  $\xi$ - $z$ :

$$\frac{dN(\xi, z|\mathbf{p})}{d\xi dz} = \int dM dz \Theta(\xi - 5, z - 0.3) P(\xi|M, z, \mathbf{p}) \otimes \frac{dn(M, z|\mathbf{p})}{dM} \frac{dV(z)}{dz} \quad (2.6)$$

where  $dV/dz$  is the comoving volume within each redshift bin,  $\mathbf{p}$  is a vector containing all scaling relation and cosmological parameters, and  $\Theta$  is the Heaviside step function describing cluster selection in the SZE observable  $\xi > 5$ , and observed redshift  $z > 0.3$ . The term  $P(\xi|M, z, \mathbf{p})$  describes the relationship between mass and the SZE observable from the scaling relation (Equations 2.1 and 2.2), and contains both intrinsic and observational uncertainties. In practice, we convolve the mass function with this probability distribution.

Finally, the logarithm of the likelihood  $\mathcal{L}$  for the observed cluster counts is computed following Cash (1979). After dividing up the observable space in small bins, the number of expected clusters in each bin is assumed to follow a Poisson distribution. With this the likelihood function is

$$\ln \mathcal{L}(\mathbf{p}) = \sum_i \ln \frac{dN(\xi_i, z_i|\mathbf{p})}{d\xi dz} - \int \frac{dN(\xi, z|\mathbf{p})}{d\xi dz} d\xi dz, \quad (2.7)$$

up to a constant offset, and where  $i$  runs over all clusters in the catalog. For clusters without spectroscopic data, we integrate the model over redshift weighting with a Gaussian whose central value and width correspond to the cluster's photometric redshift measurement.

The 720 deg<sup>2</sup> survey area contains five fields of different depths, see Section 2.2.1. In practice, we perform the above calculation for each field rescaling  $A_{\text{SZ}}$  with the corresponding factor, and sum the resulting log likelihoods.

## Mass Calibration

For each cluster in our sample containing additional mass calibration information from X-ray and/or velocity dispersions, we include the  $Y_X$  or  $\sigma_v$  measurement as follows: At every point in cosmological and scaling relation parameter space  $\mathbf{p}$ , we calculate the probability distribution  $P(M|\xi, z, \mathbf{p})$  for each cluster mass, given that the cluster has a measured significance  $\xi$  and redshift  $z$ :

$$P(M|\xi, z, \mathbf{p}) \propto P(\xi|M, z, \mathbf{p})P(M|z, \mathbf{p}). \quad (2.8)$$

In practice, we calculate the probability distribution  $P(\xi|M, z, \mathbf{p})$  from the SZE scaling relation (Equations 2.1 and 2.2) taking both intrinsic and observational scatter into account, and weight by the mass function  $P(M|z, \mathbf{p})$ , thereby correcting for Eddington bias. We then calculate the expected probability distribution in the follow-up observable(s) which we here call  $O$  for simplicity:

$$P(O|\xi, z, \mathbf{p}) = \int dM P(O|M, z, \mathbf{p})P(M|\xi, z, \mathbf{p}). \quad (2.9)$$

The term  $P(O|M, z, \mathbf{p})$  contains the intrinsic scatter and observational uncertainties in the follow-up observable. We assume the intrinsic scatter in the SZE scaling relation and the follow-up measurements to be uncorrelated. For each cluster in the mass calibration sample, we compare the predicted  $P(O|\xi, z, \mathbf{p})$  with the actual measurement and extract the probability of consistency. Finally, we sum the log-likelihoods for all these clusters and add the result to the number count likelihood (Equation 2.7).

It is important that any cosmological dependence of the mass calibration observations be accounted for. In the case of a single velocity dispersion  $\sigma_v$ , the measurement comes from the combination of redshift measurements from a sample of cluster galaxies; the cosmological sensitivity, if any, is subtle. On the other hand, the X-ray observable  $Y_X$  is calculated from the measured temperature and gas mass within  $r_{500}$ , and the limiting radius and the gas mass are both cosmology dependent. Therefore,  $Y_X$  has to be extracted from the observations for each set of cosmological and scaling relation parameters as described in Section 2.2.4.

## Unconfirmed Cluster Candidates

Out of the 100 cluster candidates in the survey, 6 detections could not be confirmed by the optical follow-up and were assigned lower redshift limits based on the depth of the imaging data (Song et al. 2012a). In addition, each of these unconfirmed candidates has some probability of being a noise fluctuation.

Our treatment of these candidates takes into account the false detection rate at the detection signal-to-noise as well as the expected number of clusters exceeding the lower redshift bound of the candidate as predicted by the cluster mass function. We calculate the probability of a candidate  $i$  to be a true cluster according to

$$P_{\text{true}}^i = \frac{N_{\text{expected}}(\xi^i, z_{\text{low}}^i | \mathbf{p})}{N_{\text{expected}}(\xi^i, z_{\text{low}}^i | \mathbf{p}) + N_{\text{false detect}}(\xi^i)} \quad (2.10)$$

where the number of clusters  $N_{\text{expected}}$  above some lower redshift limit is given by  $\int_{z_{\text{low}}^i}^{\infty} N(\xi^i, z | \mathbf{p}) dz$ . The expected number of false detections as a function of  $\xi$  has been estimated from simulations and cross-checked against direct follow-up and is assumed to be redshift independent (Song et al. 2012a; Reichardt et al. 2013).

In the cosmological analysis, each of the unconfirmed candidates is treated like an actual cluster but weighted with its  $P_{\text{true}}^i$ . However, the specific treatment of the unconfirmed candidates has little effect on the cosmological and scaling relation parameters; for example, simply removing these candidates from the catalog leads to negligible changes in the results.

### 2.4.2 Discussion of the Analysis Method

In previous SPT cluster cosmology studies, we have used a somewhat different method. In that method the expected number density of clusters as a function of  $\xi$ ,  $Y_X$ , and  $z$  is calculated on a three-dimensional grid. The likelihood is evaluated by comparing this prediction to the cluster sample in a way analogous to Equation 2.7. For clusters without  $Y_X$  data the likelihood is integrated over the full range of  $Y_X$  (Benson et al. 2013).

As we show in the Appendix, the method we employ in the current analysis is mathematically equivalent to this other method; here we assume uncorrelated scatter. For the current application, where we have  $\sigma_v$  and  $Y_X$  follow-up measurements, we do not work in the four-dimensional  $\xi$ - $Y_X$ - $\sigma_v$ - $z$ -space, but rather we treat the number count part of the likelihood in its  $\xi$ - $z$ -space, and the mass calibration part of the likelihood  $P(O|\xi, z, p)$  separately. The results obtained with this analysis method do not show any sign of biases when tested against different sets of mock data (see Section 2.4.4). This method is convenient when analyzing a cluster sample with multiple different mass observables where only a fraction of the clusters have those observables. In the limit where every cluster in the survey has the same follow-up mass measurements, the likelihood presented and used in our previous analyses (Benson et al. 2013; Reichardt et al. 2013) would be more computationally efficient.

### 2.4.3 Priors Used in the Analysis

We present the priors used in our analysis and discuss their motivation. All priors are also listed in the first column of Table 2.1.

#### Priors on SZE $\xi$ -mass Scaling Relation Parameters

The SZE scaling relation parameters were estimated from simulations of the SZE sky of about  $4000 \text{ deg}^2$  in size (Reichardt et al. 2013). We adopt 30%, 20%, 50% Gaussian uncertainties on  $A_{\text{SZ}}$ ,  $B_{\text{SZ}}$ , and  $C_{\text{SZ}}$ , respectively (e.g., Vanderlinde et al. 2010). For the scatter  $D_{\text{SZ}}$ , we adopt a conservative 67% uncertainty (Benson et al. 2013; Reichardt et al. 2013).

#### Priors on $Y_X$ -mass Scaling Relation Parameters

The priors used in the X-ray scaling relation parameters are motivated by published constraints from X-ray measurements and simulations. The absolute mass scale of the  $Y_X$ -mass scaling relation has been calibrated using hydrostatic mass estimates of a sample of 17 low-redshift ( $z < 0.3$ ) relaxed clusters (Vikhlinin et al. 2009a). Simulations were used to estimate an upper limit of 4% on the systematic offset in the  $Y_X$ -mass relation between relaxed and unrelaxed clusters (Kravtsov et al. 2006). Also, simulations predict that biases in hydrostatic mass estimates are less for relaxed clusters and are of the order of 15% (Nagai et al. 2007). Therefore, the  $Y_X$ -mass relationship calibrated from hydrostatic mass of a sample of relaxed clusters should be in principle applicable to less relaxed systems.

We adopt the best-fit value of  $A_X = 5.77 \pm 0.20$  for the normalization and  $B_X = 0.57 \pm 0.03$  for the slope where uncertainties are statistical only (Vikhlinin et al. 2009a). The systematic uncertainty on  $A_X$  was determined by comparing to weak-lensing mass estimates for a sample of 10 low-redshift clusters (Hoekstra 2007). The derived  $1\sigma$  systematic uncertainty is 9% on the *Chandra* mass calibration. Adding this in quadrature to the statistical uncertainty yields the Gaussian prior  $A_X = 5.77 \pm 0.56$  we use in this study.

For the redshift evolution parameter, we assume a Gaussian prior  $C_X = -0.4 \pm 0.2$ . The 50% uncertainty is motivated by simulations (Kravtsov et al. 2006) and matches the prior used in the hydrostatic calibration analysis (Vikhlinin et al. 2009a).

We apply a Gaussian prior  $D_X = 0.12 \pm 0.08$  on the log-normal intrinsic scatter. The central value of the prior is chosen to be consistent with simulations (e.g., Kravtsov et al. 2006), while the uncertainty is chosen to encompass the range found in simulations and in measured values in the literature (Vikhlinin et al. 2009a; Mantz et al. 2010a).

### Priors on $\sigma_v$ -mass Scaling Relation Parameters

The statistical uncertainty on the normalization  $A_{\sigma_v}$  of the relation is of the order of 0.06% (Saro et al. 2013). However, there is a systematic uncertainty associated with the poorly determined galaxy velocity bias  $b$ , and this has been the focus of multiple investigations. Remember that  $b = 1$  means no bias. For example, from the analysis of the Millennium simulation (Springel et al. 2005), a weak velocity bias of 1.02 is claimed (Faltenbacher & Diemand 2006), while Biviano et al. (2006) derive a bias of 0.95 using gas dynamic simulations (Borgani et al. 2004). Based on the comparison of different simulations, Evrard et al. (2008) estimates a bias of  $1.00 \pm 0.05$ , and White et al. (2010) derives a value  $\sim 1.06$  from their own  $N$ -body simulation. In more recent studies comparing different simulations, Wu et al. (2013) and Gifford et al. (2013) find a spread in velocity bias of the order of 10%. Taking into account these different results, we adopt a Gaussian 5% prior on the normalization of the scaling relation centered at the value given by Saro et al. (2013):  $A_{\sigma_v} = 939 \pm 47 \text{ km s}^{-1}$ . This corresponds to a 15% systematic uncertainty floor in the velocity dispersion mass estimates used in our analysis. We expect future studies to help in providing more accurate estimations of the velocity bias.

In our recent presentation of the velocity dispersion data on the SPT cluster sample (Ruel et al. 2014) we note a 10% offset in the dispersion normalization of the dataset as compared to the predicted dispersions (Saro et al. 2013) when using the previously published SPT cluster masses (Reichardt et al. 2013). Stated in another way, this offset is an indication that if the dispersions were used for mass calibration, then they would lead to a change in the mass scale of the SPT cluster sample. This expectation is confirmed in the results presented below (see Section 2.5.1).

Saro et al. (2013) find the statistical uncertainties for the slope  $B_{\sigma_v}$  and the evolution term  $C_{\sigma_v}$  to be  $O(10^{-4})$  and  $O(10^{-3})$ , respectively, and hence completely negligible. However, these results do not include potential systematic uncertainties. We adopt conservative 5% Gaussian uncertainties on both parameters and apply  $B_{\sigma_v} = 2.91 \pm 0.15$  and  $C_{\sigma_v} = 0.33 \pm 0.02$ . We confirm that the width of those priors plays a negligible role in our analysis by tightening both priors to the levels of the statistical uncertainties quoted above; the results on all other parameters remain essentially unchanged.

The effect of interlopers is the dominant contribution to the intrinsic scatter (Saro et al. 2013) and we assume a 20% uncertainty on the scatter normalization  $D_{\sigma_0} = 0.2 \pm 0.04$  as well as a 20% uncertainty on its dependence on the number of observed galaxies  $D_{\sigma N} = 3 \pm 0.6$ . The results from our observed velocity dispersion sample support this approach; we measure the scatter in the observed sample to be  $D_{\sigma_v} = 0.31 \pm 0.03$  (Ruel et al. 2014). In the present analysis we use a parametrization of the scatter that includes the number of spectroscopically observed galaxies (see Section 2.3). For the typical number of observed galaxies in our sample  $\langle N_{\text{gal}} \rangle = 25$ , we model the scatter to be  $D_{\sigma_v}(N_{\text{gal}} = 25) = 0.32$ , which is in very good agreement with the direct measurement.

### Additional Priors on Cosmological Parameters

Galaxy clusters are not sensitive to all cosmological parameters. Therefore, when not including the CMB dataset in a cosmological analysis, we fix the optical depth at reionization to the WMAP9 best-fit value  $\tau = 0.089$  and we adopt a Gaussian prior on the spectral index  $n_s = 0.972 \pm 0.013$  representing the WMAP9 result.

#### 2.4.4 Validation of the Analysis Tool using Mock Data

We validate the analysis method using simulated data. In a first step we test the number count part in SZE significance and redshift space using simulated cluster catalogs that match the SPT data but contain orders of magnitude more clusters; our goal here is to minimize statistical noise so as to resolve possible systematics in the analysis at a level far below the statistical noise in our real sample. Our mock generator produces clusters in mass-redshift space, converts the cluster masses to the SZE observable  $\xi$  using Equations 2.1 and 2.2 with log-normal and normal scatter, respectively, and then applies the survey selection. The crucial part of the analysis - that is the conversion from mass to observable - is thereby computed differently than in the likelihood code we use to explore cosmological parameter space.

We generate large catalogs using different sets of input values and obtain samples containing on the order of  $10^4$  clusters. We then run our analysis pipeline on the mock data using priors equivalent to the ones listed in Table 2.1; our tests show that we are able to recover the input values to within  $1\sigma$  statistical uncertainties, verifying that there are no biases in our codes at a level well below the statistical noise in our real cluster ensemble.

We further analyzed mock catalogs produced using the analysis pipeline used in our previous analyses (Benson et al. 2013; Reichardt et al. 2013), recovering the input parameters at the  $1\sigma$  statistical level. To test the mass calibration module, we use a subset of 500 clusters drawn from the SZE mock catalog described above and additionally convert the cluster masses to X-ray  $Y_X$  and velocity dispersion  $\sigma_v$  measurements. We then run our analysis code on the mass calibration part alone, that is without using the number count information and use  $Y_X$  and/or  $\sigma_v$ , showing that we are able to recover the input values. Finally we confirm that the combination of number counts and mass calibration produces unbiased results by combining the SZE mock catalog with the X-ray and spectroscopic cluster mass observables. These tests give us confidence that our code is producing unbiased constraints.

## 2.5 Results

In this section, we present the results of our mass calibration and cosmological analysis. As we discuss in detail, the constraints obtained using  $\sigma_v$  mass calibration are statistically consistent with those we obtain using  $Y_X$ , but the dispersions prefer higher cluster masses. Assuming a flat  $\Lambda$ CDM cosmology, we compare the constraints obtained from the SPT galaxy clusters and mass calibration with independent cosmological constraints from CMB anisotropies, and finally combine the datasets in order to obtain tighter cosmological constraints. We then use the combined datasets to constrain extensions of the standard cosmological model in which the Dark Energy equation of state or the sum of neutrino masses are allowed to vary. Finally, we present the first SPT result on the cosmological growth of structure.

#### 2.5.1 Using $\sigma_v$ and $Y_X$ as Mass Calibrators

In Table 2.1, we present the results of the analysis of the SPT-SZ survey cluster sample and its mass calibration assuming a flat  $\Lambda$ CDM model. For now we do not include CMB, BAO, or SNIa data, because we first wish to isolate the galaxy cluster constraints and the impact of the mass calibration data. However, we include the BBN and  $H_0$  priors, because not all parameters are well constrained by the cluster data.

We present results using the SPT cluster sample  $N(\xi, z)$  only,  $N(\xi, z)$  with  $Y_X$  data,  $N(\xi, z)$  with  $\sigma_v$  data, and  $N(\xi, z)$  with both  $Y_X$  and  $\sigma_v$ . It is clear that the additional mass information from  $\sigma_v$  or  $Y_X$  help in improving the results obtained from  $N(\xi, z)$  only. The constraints on the SZE scaling relation normalization  $A_{SZ}$ , the scatter in that relation  $D_{SZ}$ , and the cosmological parameter combination  $\sigma_8(\Omega_m/0.27)^{0.3}$  tighten. The uncertainty on this parameter reflects the width of the likelihood distribution in  $\Omega_m$ - $\sigma_8$  space in the direction orthogonal to the cluster degeneracy (see Figure 2.1).

There is agreement between the results obtained using the mass calibrators  $\sigma_v$  or  $Y_X$ , which provides an indication that both methods are reliable and that systematics are under control. The normalization  $A_{SZ}$  de-

creases by 22% when replacing the  $Y_X$  calibration dataset with the  $\sigma_v$  dataset. Due to the skewness of the probability distributions with tails towards larger values, the constraints on  $A_{\text{SZ}}$  from  $\sigma_v$  and  $Y_X$  measurements have significant overlap, with the  $Y_X$ -favored value displaced  $1.15\sigma$  from the result obtained from  $\sigma_v$  (see also Figure 2.2). The constraints on the slope  $B_{\text{SZ}}$ , the redshift evolution parameter  $C_{\text{SZ}}$ , as well as the scatter  $D_{\text{SZ}}$  are not much affected by the choice of the mass calibrator. We note that the  $Y_X$  scaling relation is calibrated by observations at  $z \sim 0.3$  which is extrapolated to higher redshifts using priors motivated by simulations, whereas the  $\sigma_v$  scaling relation is calibrated to simulations over the full redshift range. In terms of the cosmological results, both follow-up methods perform similarly in constraining the fully marginalized values for  $\Omega_m$  and  $\sigma_8$ . However, the  $Y_X$  calibration does better in constraining  $\sigma_8(\Omega_m/0.27)^{0.3}$ .

Our constraints using SPT clusters with mass calibration from X-ray  $Y_X$  only are comparable with previously published results from nearly the same cluster sample (Reichardt et al. 2013). Note that the X-ray sample used here contains measurements of  $Y_X$  for two additional clusters (see Section 2.2.4). We recover almost identical constraints on the SZE and X-ray scaling relation parameters. However, in the  $\Omega_m$ - $\sigma_8$  plane, the constraints presented here extend further along the degeneracy direction towards higher values of  $\Omega_m$ . This difference is due to a prior on the power spectrum normalization  $\ln(10^{-10}A_s) = [2.3, 4]$  that was narrow enough to affect the cosmological constraints in Reichardt et al. (2013); we fit for  $\sigma_8$  in the range [0.4, 1.2] which is much broader than the recovered probability distribution and hence our choice of prior does not affect our results.

We estimate the effect of potentially larger galaxy velocity bias (see discussion in Section 2.3 and 2.4.3) by loosening our prior on  $A_{\sigma_v}$  from the 5% recommended by Saro et al. (2013) to 10% when analyzing the  $N(\xi, z) + \sigma_v + \text{BBN} + H_0$  data. There is a broadening of the uncertainty on  $A_{\text{SZ}}$  by 25%, and a  $\sim 0.3\sigma$  shift to a higher value. The constraint on  $\sigma_8(\Omega_m/0.27)^{0.3}$  degrades by 14% and shifts only by a negligible amount. In addition, we examine the impact of tightening the prior on  $A_{\sigma_v}$  to 1%. In this case, we observe improvements on the constraints on  $A_{\text{SZ}}$  (28%) and  $\sigma_8(\Omega_m/0.27)^{0.3}$  (23%).

Because of the consistency of the two calibration datasets, we combine them into a joint mass calibration analysis. We observe that the SZE normalization  $A_{\text{SZ}}$  remains close to the value favored by the  $\sigma_v$  measurements, while its 68% confidence region decreases by roughly 20% compared to the individual results. This impact on  $A_{\text{SZ}}$  is the best improvement on the SZE parameters we observe when combining the mass calibrators. The constraints on  $\Omega_m$  and  $\sigma_8$  lie between the individual results with similar uncertainties. However,  $\sigma_8(\Omega_m/0.27)^{0.3}$  clearly benefits from the combined mass information, and its uncertainty is 10% (23%) smaller than when using the individual  $Y_X$  ( $\sigma_v$ ) calibration data.

### 2.5.2 $\Lambda$ CDM Results with WMAP9

We now compare the results from our cluster data with constraints from CMB anisotropies as obtained from WMAP9. The probability distributions of the cluster datasets and WMAP9 overlap, indicating agreement between both sets of constraints (see also Figure 2.1). Moreover, the parameter degeneracies in the  $\Omega_m$ - $\sigma_8$  space for clusters are nearly orthogonal to the ones of CMB data.

We quantify the agreement between two datasets by testing the degree to which their probability distributions  $P(\mathbf{x})$  overlap in some parameter space  $\mathbf{x}$ . We measure this by first drawing representative samples of points  $\{\mathbf{x}_1\}$  and  $\{\mathbf{x}_2\}$  from the two probability distributions  $P_1(\mathbf{x})$  and  $P_2(\mathbf{x})$ . We then compute the distances between pairs of sampled points  $\delta \equiv \mathbf{x}_1 - \mathbf{x}_2$  and estimate the probability distribution  $P_\delta$  from this ensemble  $\{\delta\}$ . We then evaluate the likelihood  $p$  that the origin lies within this distribution:

$$p = \int_S d\mathbf{y} P_\delta(\mathbf{y}) \quad (2.11)$$

where the space  $S$  is that where  $P_\delta < P_\delta(\mathbf{0})$ , and  $P_\delta(\mathbf{0})$  is the probability at the origin. We convert  $p$  to a significance assuming a normal distribution. Within the PMC fitting procedure used to obtain the probability distributions  $P$ , each sample point  $\mathbf{x}$  is assigned a weight. We calculate the agreement between two distributions

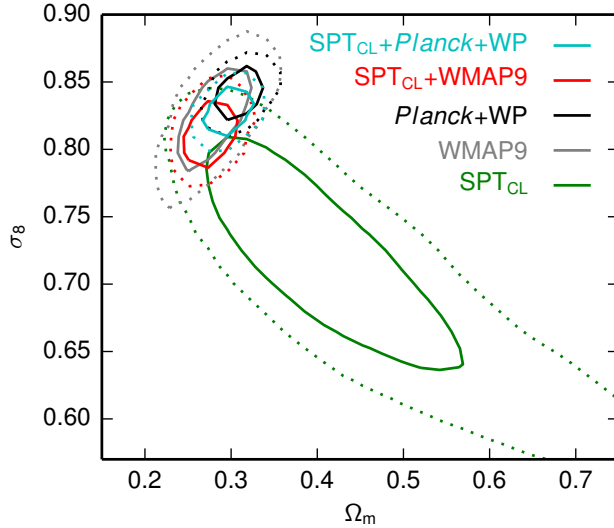


Figure 2.1 Likelihood contours (68% and 95%) in  $\Omega_m$ - $\sigma_8$  space for SPT clusters with  $\sigma_v$  and  $Y_X$  ( $SPT_{CL}$ ), CMB from WMAP9 and  $Planck+WP$ , and the combination of clusters with CMB data. The independent cluster and CMB constraints overlap, and their approximate orthogonality make them particularly complementary. We quantify the agreement between  $SPT_{CL}$  and WMAP9 ( $Planck+WP$ ) to be  $1.3\sigma$  ( $1.9\sigma$ ) (see Section 2.5.2). Accounting for a single massive neutrino ( $m_\nu = 0.06$  eV) shifts these values to  $1.0\sigma$  ( $1.5\sigma$ ); treating the sum of neutrino masses as a free parameter yields  $0.7\sigma$  ( $1.1\sigma$ ).

using the method presented above, assigning each point  $\delta$  a weight that is the product of the weights of the points  $x_1$  and  $x_2$ .

We apply this method in the two-dimensional  $\Omega_m$ - $\sigma_8$  space. Within our baseline model that assumes massless neutrinos we report good consistency ( $1.3\sigma$ ) between the results from our cluster sample and from WMAP9. Changing the baseline assumptions to account for one massive neutrino with mass  $m_\nu = 0.06$  eV decreases the tension to  $1.0\sigma$ . We note that this increase in neutrino mass shifts CMB constraints towards lower values of  $\sigma_8$  by about  $\Delta\sigma_8 \approx -0.012$  while having negligible impact on the cluster constraints. We fit for the sum of neutrino masses in Section 2.5.7; this further reduces the tension.

Given the overlap between the probability distributions from our clusters and WMAP9 we combine the datasets to break degeneracies and thereby tighten the constraints. In Table 2.2, we show how the combination of the  $N(\xi, z)$  cluster sample with WMAP9 data benefits from the additional mass calibration from  $\sigma_v$  and/or

Table 2.2 Impact of  $\sigma_v$  and/or  $Y_X$  mass calibration on results from SPT clusters  $N(\xi, z)+WMAP9$ .

Dataset	$A_{SZ}$	$\Omega_m$	$\sigma_8$	$\sigma_8(\Omega_m/0.27)^{0.3}$
$N(\xi, z)+WMAP9$	$3.59^{+0.60}_{-1.04}$	$0.284 \pm 0.027$	$0.823 \pm 0.026$	$0.835 \pm 0.047$
$N(\xi, z)+WMAP9+\sigma_v$	$3.51^{+0.65}_{-0.63}$	$0.288 \pm 0.022$	$0.824 \pm 0.020$	$0.840 \pm 0.035$
$N(\xi, z)+WMAP9+Y_X$	$3.85^{+0.62}_{-0.66}$	$0.273 \pm 0.019$	$0.811 \pm 0.019$	$0.813 \pm 0.032$
$N(\xi, z)+WMAP9+Y_X+\sigma_v$	$3.79^{+0.57}_{-0.63}$	$0.276 \pm 0.018$	$0.812 \pm 0.017$	$0.817 \pm 0.027$

Note. — These are fully marginalized constraints. The results from  $N(\xi, z)+Y_X+\sigma_v+WMAP9$  are presented in more detail in Table 2.1.

$Y_X$ . It is clear that, even if the cosmological constraints are dominated by the CMB data, the mass calibration from either observable leads to tighter constraints on all four parameters shown in the table. We also observe that the constraints on the cosmological parameters  $\Omega_m$ ,  $\sigma_8$ , and  $\sigma_8(\Omega_m/0.27)^{0.3}$  obtained when including  $Y_X$  data are systematically lower by about half a  $\sigma$  than results obtained without these data; the constraints on  $A_{\text{SZ}}$  are higher. These shifts correspond to lower cluster masses; we will come back to this in Section 2.5.4.

When adding the WMAP9 data to our full cluster sample  $SPT_{\text{CL}}$  we observe shifts in the SZE scaling relation parameters, as shown in Table 2.1. There is a decrease in the SZE normalization  $A_{\text{SZ}}$  by 19%, and the uncertainty tightens by 42%. We further observe a notable shift in the redshift evolution  $C_{\text{SZ}}$  towards a lower value at the  $1\sigma$  level. This is due to the degeneracy between  $C_{\text{SZ}}$  and  $\Omega_m$ , as the latter also shifts significantly when the WMAP9 data are added. The remaining scaling relation parameters do not benefit from the additional data. Conversely, the SPT cluster data improve the cosmological constraints from the WMAP9 data by reducing the uncertainty on  $\Omega_m$  by 36%, on  $\sigma_8$  by 33%, and on  $\sigma_8(\Omega_m/0.27)^{0.3}$  by 47%. Figure 2.1 shows how the combination of the datasets leads to improved constraints due to the nearly orthogonal parameter degeneracies of the individual results (red contours in figure).

Finally, we add data from BAO and SNIa which carry additional information on cosmic distances. As expected, we see a further tightening of the constraints on  $\Omega_m = 0.292 \pm 0.011$  and  $H_0 = 68.6 \pm 1.0 \text{ km s}^{-1} \text{ Mpc}^{-1}$ .

### 2.5.3 $\Lambda$ CDM Results with *Planck+WP*

In Figure 2.1, we also show the constraints in the  $\Omega_m$ - $\sigma_8$  plane from *Planck+WP* and report a mild  $1.9\sigma$  tension between our cluster sample and this CMB dataset. The tension is slightly larger than when comparing the clusters to WMAP9. The *Planck+WP* data favor a larger value of  $\sigma_8$  than our cluster sample. Assuming one massive neutrino with mass  $m_\nu = 0.06 \text{ eV}$  relaxes the tension to  $1.5\sigma$ .

We proceed and combine our cluster sample with the CMB data from *Planck+WP*. This data combination prefers a value for  $\sigma_8$  that is about  $1\sigma$  lower than suggested by the CMB data. Adding our cluster sample to *Planck+WP* leads to improvements on the constraints on  $\Omega_m$ ,  $\sigma_8$  and  $\sigma_8(\Omega_m/0.27)^{0.3}$ , all on the order of 15% (see Table 2.1, and black/cyan contours in Figure 2.1).

We add BAO and SNIa data to further improve the cosmological constraints, and measure  $\Omega_m = 0.297 \pm 0.009$ ,  $\sigma_8 = 0.829 \pm 0.011$ ,  $\sigma_8(\Omega_m/0.27)^{0.3} = 0.855 \pm 0.016$ , and  $H_0 = 68.3 \pm 0.8 \text{ km s}^{-1} \text{ Mpc}^{-1}$ . These represent improvements of 18% ( $\Omega_m$ ), 8% ( $\sigma_8$ ), and 11% ( $\sigma_8(\Omega_m/0.27)^{0.3}$ ) over the constraints from *Planck+WP+BAO+SNIa* without  $SPT_{\text{CL}}$ . In addition, these represent improvements of 18% ( $\Omega_m$ ), 31% ( $\sigma_8$ ), 20% ( $\sigma_8(\Omega_m/0.27)^{0.3}$ ) and 20% ( $H_0$ ) over the corresponding parameter uncertainties when using WMAP9 instead of *Planck+WP*.

### 2.5.4 Impact on Cluster Masses

Combining the mass calibration from  $Y_X$  with  $\sigma_v$  data and further with CMB data leads to shifts in the SZE scaling relation parameters which ultimately shift the mass estimates of the clusters. As shown in Figure 2.2, there is a systematic increase of the cluster mass scale as we move from X-ray to dispersion only calibration, further on to  $Y_X + \sigma_v$  and finally on to analyses of our  $SPT_{\text{CL}}$  dataset in combination with external datasets (remember that a decrease in  $A_{\text{SZ}}$  corresponds to an increase in cluster mass, see Equation 2.2). Also, it is clear that the constraints on the SZE normalization  $A_{\text{SZ}}$  obtained when including CMB data are much stronger than the constraints from the cluster data alone. The Gaussian prior on  $A_{\text{SZ}}$  is in some tension with the  $A_{\text{SZ}}$  constraints after including the CMB data. In this case, we note that the recovered values of  $A_{\text{SZ}}$  do not significantly change when removing the prior, because it is much broader than the recovered constraints.

We quantify the agreement between these distributions in the space of  $A_{\text{SZ}}$  in a way equivalent to the one presented in Section 2.5.2. We find that the results from both  $Y_X$  and  $\sigma_v$  mass calibration are consistent at the  $0.6\sigma$  level. There is a mild tension ( $1.9\sigma$ ) between mass calibration from  $Y_X$  and  $SPT_{\text{CL}} + \text{Planck+WP+BAO+SNIa}$ , while the mass calibration from  $\sigma_v$  is consistent with the multi-probe dataset at the  $0.8\sigma$  level. These shifts would approximately correspond to an increase in the preferred cluster mass scale by 44% and 23%, respectively, when using the multi-probe dataset. Note that there are shifts in  $B_{\text{SZ}}$  and  $C_{\text{SZ}}$  when adding CMB data

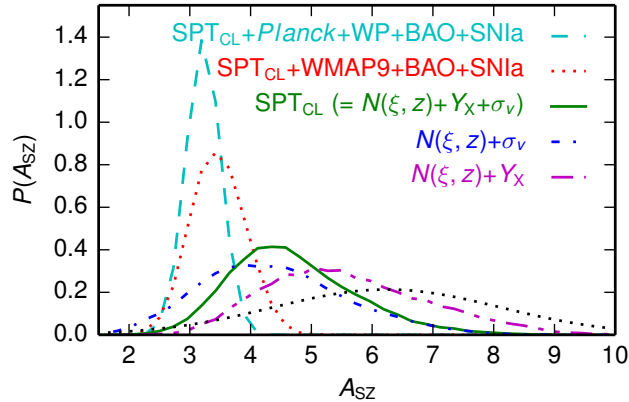


Figure 2.2 Posterior probability distributions for the normalization  $A_{\text{SZ}}$  of the SZE  $\zeta$ -mass relation for different combinations of mass calibration, CMB, and additional datasets. The Gaussian prior is shown by the black dashed curve. Note the systematic trend towards lower  $A_{\text{SZ}}$  values and smaller uncertainty when adding external cosmological data, corresponding to an increase in the characteristic scale of SPT cluster masses by  $\sim 44\%$  from  $N(\xi, z) + Y_X$  (magenta) to SPT<sub>CL</sub>+CMB+BAO+SNIa (cyan/red).

to our cluster sample which add a slight  $\xi$  (or equivalently mass), and redshift dependence to this comparison of cluster masses.

On average, our cluster mass estimates are higher by 32% than our previous results in Reichardt et al. (2013), primarily driven by using new CMB and BAO datasets. Relative to Reichardt et al. (2013), we have updated the CMB data set from WMAP7 and SPT (Komatsu et al. 2011; Keisler et al. 2011) to *Planck*+WP (Planck Collaboration et al. 2014a,b), and also updated the BAO dataset from Percival et al. (2010) to a combination of three measurements (Beutler et al. 2011; Anderson et al. 2012; Padmanabhan et al. 2012). The new datasets have led to more precise constraints on the cosmological parameters, in particular  $\sigma_8(\Omega_m/0.27)^{0.3}$ , and drive shifts in the preferred cluster mass scale through  $A_{\text{SZ}}$ , to improve consistency between the cluster data set and the cosmological constraints. For example, using WMAP9 data instead of *Planck*+WP+BAO+SNIa leads to an average 11% decrease of the cluster masses. Finally, we observe an increase in the slope  $B_{\text{SZ}}$  as compared to Reichardt et al. (2013) which reduces the mass change to only  $\sim 15\%$  on the high-mass end of the sample.

### 2.5.5 Goodness of Fit of Cluster Data

Our analysis to this point has focused on extracting parameter confidence regions that emerge from different combinations of our cluster sample with external datasets. We observed shifts especially in the SZE scaling relation parameters when switching among the different data combinations. In the following, we investigate whether the adopted SZE mass-observable scaling relation parametrization is adequate for describing the cluster sample. We execute two tests: (1) we evaluate the goodness of fit of the SZE selected clusters in the  $\xi$ - $z$  plane, and (2) we compare the predicted values for the follow-up observables  $Y_X$  and  $\sigma_v$  to their actual measurements. Both tests are performed adopting parameter values at the best-fit location in cosmological and scaling relation parameter space from the SPT<sub>CL</sub>+*Planck*+WP+BAO+SNIa analysis.

We compare the distribution of the SZE clusters in the observable  $\xi$ - $z$  plane with its prediction. This is done using a two-dimensional Kolmogorov-Smirnov (KS) test as described in Press et al. (1992): At the location of each cluster in  $\xi$  and  $z$  space, we split the observational space into four quadrants, and calculate the absolute difference between the number of clusters and the number predicted by the model within that area. The largest of these  $4 \times N_{\text{cl}}$  values is taken as the maximum difference  $D$  between the data and the model. We characterize

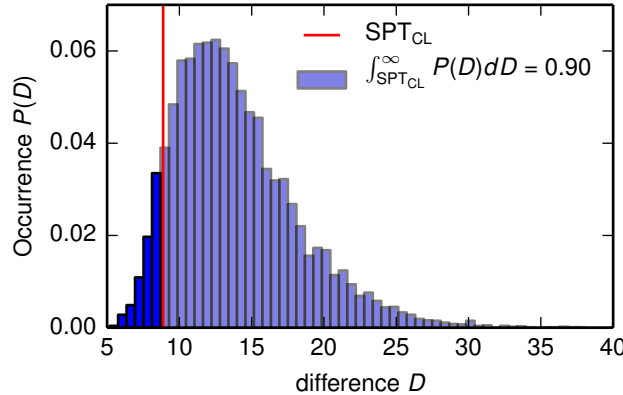


Figure 2.3 The goodness of fit of our cluster dataset to the best-fit cosmological model is evaluated using a two-dimensional KS test on the distribution of clusters in SZE signature  $\xi$  and redshift  $z$  (see Section 2.5.5). The blue histogram is the expected distribution of differences  $D$  between the observations and the model for an ensemble of 10,000 simulated realizations of the best-fit cosmology. The SPT<sub>CL</sub> dataset is marked by the red line and exhibits no tension with the parametrization from the best-fit model.

this difference measure by calculating it for 10,000 independent catalogs that we produce using the best-fit cosmology and scaling relation parameters. Figure 2.3 contains a histogram of the distribution of differences  $D$  from the set of catalogs, and the red line marks the difference for the real sample. This test indicates that there is a 90% chance of obtaining a larger difference  $D$  than observed in our real dataset. We conclude that there is no tension between our SPT cluster sample and the way we model it through the SZE scaling relation parametrization.

We now go one step further and ask whether there is tension between the predicted values for the follow-up observables  $Y_X$  and  $\sigma_v$ , and their actual measurements. Remember that the predicted probability distributions are obtained from the observed SZE signal  $\xi$  according to Equation 2.9. For each cluster, we calculate the percentile of the observed value in its predicted distribution. We get a distribution of percentiles which we convert to a distribution of pulls (Eadie & Frederick 1983; Lyons 1989) using the inverse error function:

$$\text{pull} = \sqrt{2} \times \text{erf}^{-1}(2 \times \text{percentile} - 1). \quad (2.12)$$

This distribution is finally compared to a normal distribution of unit width centered at zero using the KS test. In Figure 2.4 we show the distribution of pulls for the  $Y_X$  and  $\sigma_v$  measurements. For each observable, we show the distribution for two different sets of cosmological and scaling relation parameters: (1) the results obtained from clusters with mass calibration only, and (2) the results from clusters with mass calibration combined with the external cosmological probes. In all 4 cases, the KS test provides  $p$ -values in the range  $0.1 < p < 0.8$ , indicating no tension between the predicted follow-up mass observables and their measurements. This is an interesting observation given the shifts we observe in the scaling relation and cosmological parameters when adding CMB data to the cluster sample. It shows that the adopted form of the SZE mass-observable scaling relation has enough freedom to compensate for the shifts in cosmological parameters. With a larger cluster and mass calibration dataset we could expect to make a more precise consistency test of the data and our adopted scaling relation parametrization.

### 2.5.6 Dark Energy Equation of State

The first extension of the  $\Lambda$ CDM model we analyze is the flat  $w$ CDM cosmology which includes the Dark Energy equation of state parameter  $w$ . As the Dark Energy becomes relevant only in the late Universe and

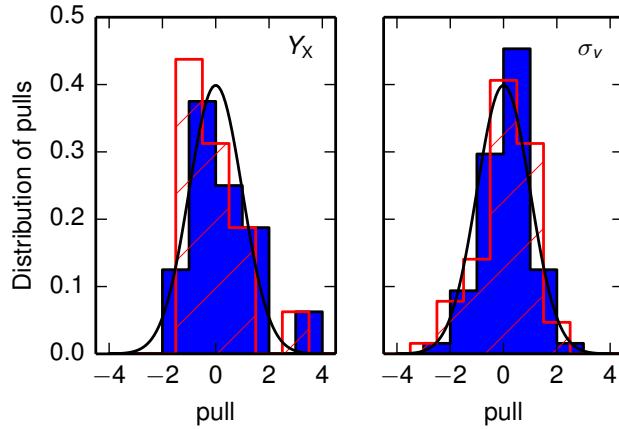


Figure 2.4 Difference of the X-ray and dispersion follow-up mass measurements and their predictions from SZE. We show the distribution of pulls (see Section 2.5.5), and the expected Gaussian distribution in black. The result obtained from clusters alone is shown in blue, and the combined results from all cosmological probes are shown in red. A KS test indicates there is no tension between our cluster mass calibration data and the expected mass distribution in the best-fit cosmology.

affects the cluster mass function through its impact on the cosmological growth rate and volume we expect our cluster sample to provide an important contribution in constraining its nature.

Analyzing our cluster sample using priors on  $H_0$  and BBN, we obtain  $w = -1.5 \pm 0.5$ . This measurement is compatible with external constraints from WMAP9+ $H_0$  ( $w = -1.13 \pm 0.11$ ) and *Planck*+WP+BAO ( $w = -1.13 \pm 0.25$ , 95% confidence limits; Planck Collaboration et al. 2014b), and consistent with the  $\Lambda$ CDM value  $w = -1$ . Remember that the results obtained from clusters might in principle be subject to systematics in the mass estimates, while, on the other hand, the CMB anisotropy measurements are most sensitive to the characteristics of the Universe at  $z \sim 1100$ , and the distance measurements are subject to their own systematics.

Combining datasets breaks degeneracies and leads to tighter constraints. When adding our SPT<sub>CL</sub> sample to the WMAP9+ $H_0$  data, we measure  $w = -1.07 \pm 0.09$ , or an 18% improvement over the constraint without clusters. Combining our cluster sample with *Planck*+WP+BAO+SNIa ( $w = -1.051 \pm 0.072$ ) data leads to an even tighter constraint, and we measure  $w = -0.995 \pm 0.063$  (12% improvement, see also Table 2.3).

### 2.5.7 Massive Neutrinos

We now extend the  $\Lambda$ CDM model and include the sum of neutrino masses  $\sum m_\nu$  as a free parameter. We will refer to this model as  $\nu$ CDM in the following, and we assume three degenerate mass neutrino species.

Massive neutrinos are still relativistic at the epoch of recombination and hence do not significantly affect the structure of CMB anisotropies (as long as  $m_\nu < 0.6$  eV for each species, Komatsu et al. 2009). In the late Universe, massive neutrinos contribute to  $\Omega_m$  but do not cluster in structures smaller than their free streaming length, leading to a lower  $\sigma_8$ . Therefore, results from CMB anisotropy data exhibit a strong degeneracy between  $\sum m_\nu$  and  $\sigma_8$ . Using the *Planck*+WP+BAO+SNIa data combination we measure  $\sum m_\nu = 0.092 \pm 0.058$  eV and an upper limit  $\sum m_\nu < 0.182$  eV (95% confidence limit, hereafter CL).

Galaxy clusters are ideal probes for measuring  $\sigma_8$  and therefore represent a valuable piece of information when constraining the  $\nu$ CDM model. When adding our SPT<sub>CL</sub> sample to the dataset, we observe that the mean of the recovered  $\sum m_\nu$  increases significantly; we measure  $\sum m_\nu = 0.148 \pm 0.081$  eV, and an upper limit  $\sum m_\nu < 0.270$  eV (95% CL). As discussed earlier, our cluster sample prefers lower values for  $\sigma_8$  than the CMB data, which here leads to increased neutrino masses due to their degeneracy with  $\sigma_8$ . The results on  $\nu$ CDM

Table 2.3 Constraints on extensions of flat  $\Lambda$ CDM cosmology from the SPT<sub>CL</sub>+*Planck*+WP+BAO+SNIa data combination.

Parameter	$w$ CDM	$v$ CDM	$\gamma+\Lambda$ CDM	$\gamma+v$ CDM	$\gamma+w$ CDM
$\Omega_m$	$0.301 \pm 0.014$	$0.309 \pm 0.011$	$0.302 \pm 0.010$	$0.309 \pm 0.012$	$0.301 \pm 0.014$
$\sigma_8$	$0.827 \pm 0.024$	$0.799 \pm 0.021$	$0.793^{+0.046}_{-0.075}$	$0.796^{+0.057}_{-0.080}$	$0.794^{+0.054}_{-0.078}$
$H_0$ (km s <sup>-1</sup> Mpc <sup>-1</sup> )	$68.1 \pm 1.6$	$67.5 \pm 0.9$	$68.2 \pm 0.8$	$67.5 \pm 0.9$	$68.3 \pm 1.6$
$w$	$-0.995 \pm 0.063$	(−1)	(−1)	(−1)	$-1.007 \pm 0.065$
$\sum m_\nu$ (eV)	(0)	$0.148 \pm 0.081$	(0)	$0.143^{+0.066}_{-0.100}$	(0)
$\sum m_\nu$ (eV), 95% CL	(0)	$< 0.270$	(0)	$< 0.277$	(0)
$\gamma$	(0.55)	(0.55)	$0.72 \pm 0.24$	$0.63 \pm 0.25$	$0.73 \pm 0.28$

Note. — These are fully marginalized constraints.

from the full data combination are also shown in Table 2.3.

We recalculate the difference between results from SPT<sub>CL</sub> and CMB data as in Section 2.5.2, but we now adopt our best-fit sum of neutrino masses  $\sum m_\nu = 0.148$  eV. This decreases the tension to  $0.7\sigma$  for WMAP9, and  $1.1\sigma$  for *Planck*+WP.

## 2.5.8 Testing the Cosmological Growth of Structure

Our constraints on the Dark Energy equation of state parameter confirm once more that the flat  $\Lambda$ CDM model provides an excellent fit to the best currently available cosmological data. However, it still remains unclear what exactly is causing the accelerating expansion in the present epoch. Possible explanations include a new energy component or a modification of gravity on large scales. While measurements of CMB anisotropies and cosmic distances (BAO and SNIa) have proven extremely useful for probing the expansion history of the Universe, galaxy clusters provide a unique probe for testing its growth history. Combining these tests allows for an interesting consistency test of General Relativity (GR) on large scales (e.g., Rapetti et al. 2013).

### Parametrized Growth of Structure

We parametrize the linear growth rate of density perturbations  $f(a)$  at late times as a power law of the matter density (e.g., Peebles 1980; Wang & Steinhardt 1998)

$$f(a) \equiv \frac{d \ln \delta}{d \ln a} = \Omega_m(a)^\gamma \quad (2.13)$$

where  $\gamma$  is the cosmic growth index and  $\delta \equiv \delta\rho_m/\langle\rho_m\rangle$  is the ratio of the comoving matter density fluctuations and the mean matter density. Solving for  $\gamma$  and assuming GR one obtains

$$\gamma_{\text{GR}} \approx \frac{6 - 3(1 + w)}{11 - 6(1 + w)} \quad (2.14)$$

where the leading correction depends on the dark energy equation of state parameter  $w$  and so  $\gamma_{\text{GR}} = 0.55$  for a cosmological constant with  $w = -1$ . Normalizing the parametrized cosmic growth factor  $D(z) \propto \delta(z)$  at some high redshift  $z_{\text{ini}}$  we can express it as

$$D_{\text{ini}}(z) = \frac{\delta(z)}{\delta(z_{\text{ini}})} = \delta(z_{\text{ini}})^{-1} \exp \int d \ln a \Omega_m(a)^\gamma \quad (2.15)$$

and the parametrized matter power spectrum becomes

$$P(k, z) = P(k, z_{\text{ini}}) D_{\text{ini}}^2(z). \quad (2.16)$$

Note that the complete wavenumber-dependence is contained in  $P(k, z_{\text{ini}})$  while the growth factor  $D_{\text{ini}}(z)$ , which now depends on  $\gamma$ , evolves with redshift only.

In our analysis, we choose an initial redshift of  $z_{\text{ini}} = 10$  as a starting point for the parametrized growth which corresponds to an era well within matter domination when  $f(a) = 1$  is a very good approximation. We modify the likelihood code presented in Section 2.4.1 so that the matter power spectrum at redshift  $z_{\text{ini}}$  is provided by CAMB and then evolves depending on the growth index  $\gamma$  according to Equations 2.15 and 2.16.

We note that this parametrization is in principle degenerate with a cosmological model containing neutrino mass as a free parameter; given a particular power spectrum constrained by the CMB anisotropies at very high redshift, variations in both neutrino mass and  $\gamma$  modify the low-redshift power spectrum. However, the SPT sample spans a broad redshift range which should ultimately allow one to differentiate between the two effects.

### Constraints on the Cosmic Growth Index

We fit for a spatially flat  $\Lambda$ CDM model with the additional degree of freedom  $\gamma$  (we will refer to this model as  $\gamma+\Lambda$ CDM). Using our SPT<sub>CL</sub> sample with BBN and  $H_0$  priors, we get results that are consistent with the prediction of GR,  $\gamma_{\text{GR}} = 0.55$ . However, the uncertainty on  $\gamma$  is large, and the 68% confidence interval is  $[-0.2, 0.7]$ . We tighten the constraints by including the CMB dataset which serves as a high-redshift “anchor” of cosmic evolution. To isolate the constraining power clusters have on growth of structure, we choose not to use the constraints on  $\gamma$  that come from the Integrated Sachs-Wolfe (ISW) effect, which has an impact on the low  $l$  CMB temperature anisotropy. Regardless, we would expect the additional constraints on  $\gamma$  from the ISW to be less constraining than the cluster-based constraints presented here (see, e.g., Rapetti et al. 2010). We further use distance information from BAO and SNIa. As presented in Table 2.3, we find  $\gamma = 0.72 \pm 0.24$ , which agrees with the prediction of GR. In Figure 2.5(a), we show the two-dimensional likelihood contours for  $\gamma$  and the most relevant cosmological parameters  $\Omega_m$  and  $\sigma_8$ . The degeneracy between  $\gamma$  and  $\Omega_m$  is weak. We see a strong degeneracy with  $\sigma_8$ , as would be expected given the dependence of  $\sigma_8$  on growth history.

Our constraints are weaker than those obtained from an X-ray cluster sample (Rapetti et al. 2013). Using 238 clusters from different X-ray catalogs together with CMB anisotropy data from the 5-year WMAP release these authors obtain  $\gamma = 0.415 \pm 0.127$ .

We also consider a  $\gamma+\nu$ CDM cosmological model, where we additionally allow a non-zero sum of the neutrino masses. There is only a mild degeneracy between  $\gamma$  and  $\sum m_\nu$ , which does not significantly degrade our constraints on cosmic growth or neutrino masses (see upper panel of Figure 2.5(a) and Table 2.3). However, the best-fit value for  $\gamma$  shifts by  $\sim 0.5\sigma$  closer to the GR value.

Finally, we consider a  $\gamma+w$ CDM cosmological model, where we fix  $\sum m_\nu = 0$  eV, and allow a varying Dark Energy equation of state parameter  $w$ . In doing so we can simultaneously account for possible departures from the standard cosmic growth history as well as departures from the expansion history as described by the  $\Lambda$ CDM model. As presented in Table 2.3, the results show consistency with the fiducial values  $\gamma_{\text{GR}} = 0.55$  and  $w_{\Lambda\text{CDM}} = -1$ . Joint parameter constraints are shown in the bottom panel of Figure 2.5(b). This combined test confirms that the standard cosmological model accurately describes the evolution of the cosmic expansion and structure formation throughout a wide redshift and distance range.

## 2.6 Summary

We use an SZE selected galaxy cluster sample from 720 deg<sup>2</sup> of the SPT-SZ survey in combination with follow-up data from optical spectroscopy and X-ray observations to carry out a calibration of the SPT mass-observable relation. This work improves on previous analyses by the inclusion of the velocity dispersion data.

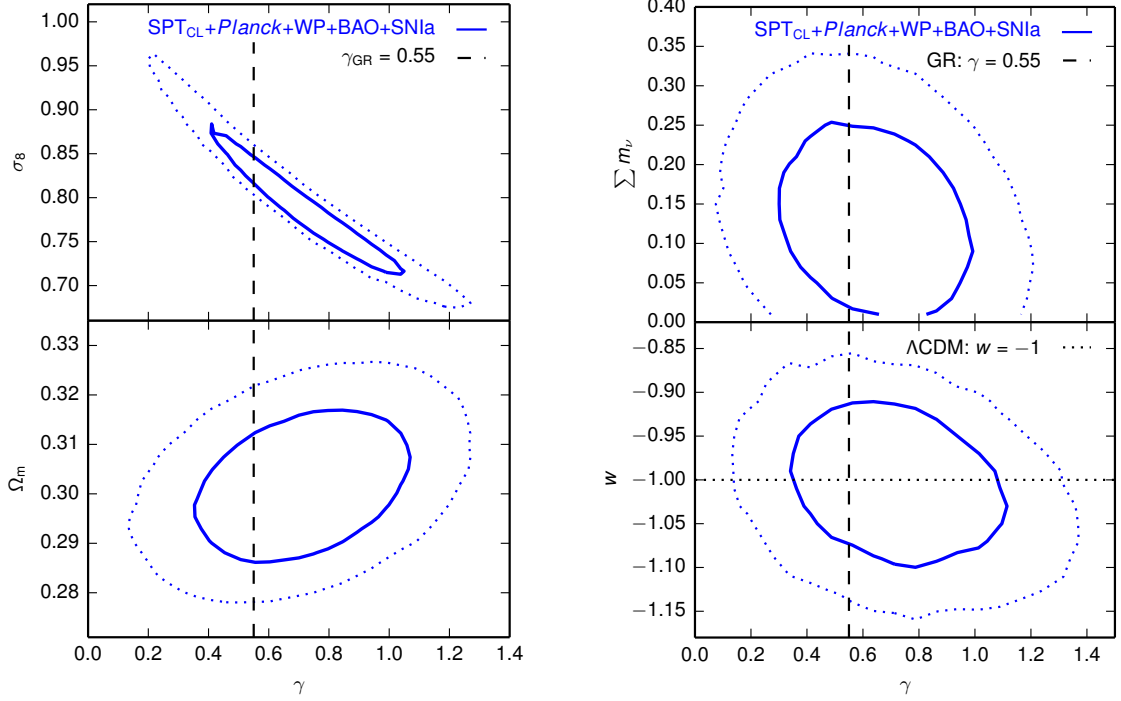


Figure 2.5 Extensions of the  $\Lambda\text{CDM}$  model including the growth index  $\gamma$ .

We present a method to fit for the SPT mass-observable relation through comparison of the SZE observable to the external calibrators  $\sigma_v$  and/or  $Y_X$ . The method accounts for selection effects in the SPT cluster survey, for intrinsic scatter in the mass-observable scaling relations, for observational uncertainties, and for uncertainties in the scaling relation parameters. With this method we compute the likelihood for the cluster counts in the space of  $\xi$  and  $z$ , and for the mass calibration using measurements in the follow-up observables.

Before combining the  $Y_X$  and  $\sigma_v$  mass calibration datasets we show that their individual constraints on the SPT  $\zeta$ -mass scaling relation parameters are comparable, agreeing at the  $0.6\sigma$  level. Given the different nature of  $Y_X$  and  $\sigma_v$  and their different calibration schemes, we argue that this agreement is a useful crosscheck of systematics present in either calibrating dataset. Combining the mass calibration datasets leads to an improvement of the constraints on  $A_{\text{SZ}}$  and  $\sigma_8(\Omega_m/0.27)^{0.3}$ . Cosmological constraints from SPT clusters with external BBN and  $H_0$  priors differ from the independent CMB anisotropy constraints from WMAP9 (*Planck+WP*) at the  $1.3\sigma$  ( $1.9\sigma$ ) level (see Figure 2.1 and Table 2.1). Accounting for the impact of one massive neutrino ( $m_\nu = 0.06$  eV) reduced the differences to  $1.0\sigma$  ( $1.5\sigma$ ).

Combining our SPT cluster sample with CMB data from WMAP9, we show that the mass calibration from  $\sigma_v$  or  $Y_X$  lead to tighter constraints on key cosmological parameters; the use of both mass calibration datasets together furthers tightens these constraints. Throughout the different combinations of cluster mass calibration and external data, we observe that the cluster mass scale from dispersions is higher than the one inferred from  $Y_X$ . As we summarize in Figure 2.2, the SZE scaling relation normalization  $A_{\text{SZ}}$  obtained using the multi-probe dataset is in better agreement with the  $\sigma_v$  calibration results ( $0.8\sigma$ ) than with the  $Y_X$  calibration results ( $1.9\sigma$ ). Analyzing the cluster sample with data from *Planck+WP*, BAO, and SNIa, we find that the average cluster masses in this work have increased by  $\sim 32\%$  relative to Reichardt et al. (2013), primarily driven by the use of new CMB and BAO datasets, which prefer a  $\Lambda$ CDM cosmology with a higher  $\sigma_8(\Omega_m/0.27)^{0.3}$ .

Assuming a flat  $\Lambda$ CDM model, and using the SPT cluster catalog,  $\sigma_v$  and  $Y_X$  mass calibration, and external data from *Planck+WP*, BAO, and SNIa, we measure  $\Omega_m = 0.299 \pm 0.009$ ,  $\sigma_8 = 0.829 \pm 0.011$ , and  $\sigma_8(\Omega_m/0.27)^{0.3} = 0.855 \pm 0.016$ . These correspond to  $18\%$  ( $\Omega_m$ ),  $8\%$  ( $\sigma_8$ ), and  $11\%$  ( $\sigma_8(\Omega_m/0.27)^{0.3}$ ) improvements over the constraints from *Planck+WP+BAO+SNIa* without  $\text{SPT}_{\text{CL}}$ .

We execute two goodness of fit tests to evaluate whether the adopted SZE mass-observable scaling relation parametrization is adequate to describe our cluster sample. As shown in Figure 2.3, there is good agreement between the distribution of the observed cluster sample in  $\xi$  and  $z$ , and the prediction by the model. We also find good agreement between the predicted SZE mass estimates, and the follow-up mass measurements, using either  $\sigma_v$  and  $Y_X$  (see Figure 2.4).

We examine an extension of the standard  $\Lambda$ CDM model by adding the Dark Energy equation of state parameter  $w$ . Our results are all compatible with  $w = -1$ , and our best constraint is  $w = -0.995 \pm 0.063$ , which we obtained from our cluster sample in combination with *Planck+WP*, BAO, and SNIa (12% improvement after adding  $\text{SPT}_{\text{CL}}$ ). We consider another extension to  $\Lambda$ CDM in which we fit for the sum of neutrino masses, and find  $\sum m_\nu = 0.148 \pm 0.081$  eV, with  $\sum m_\nu < 0.270$  eV (95% CL).

We then allow for another additional cosmological degree of freedom by parametrizing the cosmic growth rate. The growth index is constrained to  $\gamma = 0.72 \pm 0.24$  when assuming a  $\Lambda$ CDM background. This agrees with the GR prediction  $\gamma_{\text{GR}} = 0.55$ , indicating that the growth of structure is correctly described by GR. We consider the effect on  $\gamma$  when additionally allowing a non-zero sum of the neutrino masses, and find only a weak degeneracy between the two parameters, with relatively small changes in the constraints on  $\gamma$  and  $\sum m_\nu$ . Finally, we consider a  $\gamma+w$ CDM model, and allow both  $\gamma$  and  $w$  to vary. We recover results ( $\gamma = 0.73 \pm 0.28$  and  $w = -1.007 \pm 0.065$ ) that are consistent with the predictions of the standard GR+ $\Lambda$ CDM cosmological model.

Velocity dispersions haven proven to be useful follow-up mass calibrators in our analysis. However, much of their constraining power relies on a precise knowledge of the scaling relation normalization  $A_{\sigma_v}$ , which we assume to be calibrated to within 5% from  $N$ -body simulations (Saro et al. 2013). When relaxing this prior to 10% in an analysis that uses only the SZE clusters and the measured  $\sigma_v$ 's, the constraint on the SZE normalization  $A_{\text{SZ}}$  degrades by 25%, and the cosmological constraints relax modestly (14% on  $\sigma_8(\Omega_m/0.27)^{0.3}$ ). A better knowledge of the systematics in the  $\sigma_v$  mass-observable relation, in particular the galaxy velocity bias, is

therefore crucial for obtaining better constraints from ongoing and future galaxy cluster surveys. This improved knowledge could be obtained with detailed numerical simulations as well as large spectroscopic datasets.

The next steps in the SPT mass calibration consist of the inclusion of weak lensing masses and a larger number of dispersions from an ongoing program on Gemini focused at  $z < 0.8$  and a complementary program focused at  $z > 0.8$  on the VLT. In addition, X-ray observations of a sample of approximately  $\sim 100$  systems with *Chandra* and *XMM-Newton* are complete. Improved calibration of the mass-observable relations for  $Y_X$  and  $\sigma_v$  would lead to stronger cosmological constraints. Combined analyses of these calibration data together with the full SPT cluster sample (Bleem et al. 2015) will enable significant progress in cluster studies of cosmology and structure formation.

We acknowledge the support of the DFG Cluster of Excellence “Origin and Structure of the Universe” and the Transregio program TR33 “The Dark Universe”. The calculations have been carried out on the computing facilities of the Computational Center for Particle and Astrophysics (C2PAP) and of the Leibniz Supercomputer Center (LRZ). Optical spectroscopic data from VLT programs 086.A-0741 and 286.A-5021 and Gemini program GS-2009B-Q-16 were included in this work. Additional data were obtained with the 6.5 m Magellan Telescopes, which is located at the Las Campanas Observatory in Chile. This work is based in part on observations made with the *Spitzer Space Telescope*, which is operated by the Jet Propulsion Laboratory, California Institute of Technology under a contract with NASA. The South Pole Telescope is supported by the National Science Foundation through grant PLR-1248097. Partial support is also provided by the NSF Physics Frontier Center grant PHY-1125897 to the Kavli Institute of Cosmological Physics at the University of Chicago, the Kavli Foundation and the Gordon and Betty Moore Foundation grant GBMF 947. Galaxy cluster research at Harvard is supported by NSF grant AST-1009012, and research at SAO is supported in part by NSF grants AST-1009649 and MRI-0723073. Work at Argonne National Lab is supported by UChicago Argonne, LLC, Operator of Argonne National Laboratory (“Argonne”). Argonne, a U.S. Department of Energy Office of Science Laboratory, is operated under Contract No. DE-AC02-06CH11357. The McGill group acknowledges funding from the National Sciences and Engineering Research Council of Canada, Canada Research Chairs Program, and the Canadian Institute for Advanced Research.

*Facilities:* Gemini-S (GMOS), Magellan: Baade (IMACS), South Pole Telescope, *Spitzer*/IRAC, VLT: Antu (FORS2)

## Appendix: Analysis Method and Likelihood Function

We show that the analysis method we use in the present work is equivalent to the method used in previous SPT analyses. Specifically, we show how we separate the mass calibration from the cluster number counts. As presented in Equation 4 in Benson et al. (2013), the expected number density in terms of  $\xi$ ,  $z$  and the follow-up observable  $Y_X$  is

$$\frac{dN(\xi, Y_X, z|\mathbf{p})}{d\xi dY_X dz} d\xi dY_X dz = \int dMP(\xi, Y_X|M, z, \mathbf{p})P(M, z|\mathbf{p})\Theta(\xi - 5, z - 0.3), \quad (2.17)$$

and the likelihood function is evaluated according to Poisson statistics

$$\ln \mathcal{L}(\mathbf{p}) = \sum_i \ln \frac{dN(\xi_i, Y_{Xi}, z_i|\mathbf{p})}{d\xi dY_X dz} - \int \frac{dN(\xi, Y_X, z|\mathbf{p})}{d\xi dY_X dz} d\xi dY_X dz, \quad (2.18)$$

up to a constant offset, and where the sum over  $i$  runs over all clusters in the sample.

We assume no correlated scatter in the different observables, i.e. we assume that  $P(\xi, Y_X|M, z, \mathbf{p}) = P(\xi|M, z, \mathbf{p})P(Y_X|M, z, \mathbf{p})$  holds, and transform Equation 2.17 into two separate factors; this is the analysis method we use here. In the following, and for ease of reading, we omit  $z$  and  $\mathbf{p}$  (e.g.,  $P(M) \equiv P(M|z, \mathbf{p})$ ), and

the selection function  $\Theta(\xi - 5)$  as it does not depend on mass for a given cluster with measured  $\xi$ . We use Bayes' theorem twice, e.g.  $P(\xi|M)P(M) = P(M|\xi)P(\xi)$ .

$$\begin{aligned}
 \frac{dN(\xi, Y_X, z|\mathbf{p})}{d\xi dY_X dz} &= \int dM P(\xi, Y_X|M)P(M) \\
 &= \int dM P(Y_X|M)P(\xi|M)P(M) \int dM' P(M'|\xi) \\
 &= \iint dM dM' P(Y_X|M)P(M|\xi)P(\xi) \frac{P(\xi|M')P(M')}{P(\xi)} \\
 &= \int dM P(Y_X|M)P(M|\xi) \int dM' P(\xi|M')P(M') \\
 &\equiv P(Y_X|\xi, z, \mathbf{p}) \frac{dN(\xi, z|\mathbf{p})}{d\xi dz}
 \end{aligned} \tag{2.19}$$

With this, the likelihood function we use in this work is

$$\ln \mathcal{L}(\mathbf{p}) = \sum_j \ln P(Y_{Xj}|\xi_j, z_j, \mathbf{p}) + \sum_k \ln \frac{dN(\xi_k, z_k|\mathbf{p})}{d\xi dz} - \int \frac{dN(\xi, z|\mathbf{p})}{d\xi dz} d\xi dz \tag{2.20}$$

where the sum over  $k$  runs over the full SPT-SZ cluster catalog, and  $j$  runs over all clusters with  $Y_X$  measurements, thereby marginalizing over  $Y_X$  for clusters without X-ray data. Note that the total number of expected clusters  $\int \frac{dN(\xi, z|\mathbf{p})}{d\xi dz} d\xi dz$  does not depend on  $Y_X$ . The generalization to include the  $\sigma_v$  observable is straightforward.



## Chapter 3

# Constraints on the Richness-Mass Relation and the Optical-SZE Positional Offset Distribution for SZE-Selected Clusters

A. Saro, **S. Bocquet**, E. Rozo, B. A. Benson, J. Mohr, E. S. Rykoff, M. Soares-Santos, L. Bleem, S. Dodelson, P. Melchior, F. Sobreira, V. Upadhyay, J. Weller, T. Abbott, F. B. Abdalla, S. Allam, R. Armstrong, M. Banerji, A.H. Bauer, M. Bayliss, A. Benoit-Lévy, G. M. Bernstein, E. Bertin, M. Brodwin, D. Brooks, E. Buckley-Geer, D. L. Burke, J. E. Carlstrom, R. Capasso, D. Capozzi, A. Carnero Rosell, M. Carrasco Kind, I. Chiu, R. Covarrubias, T. M. Crawford, M. Crocce, C. B. D’Andrea, L. N. da Costa, D. L. DePoy, S. Desai, T. de Haan, H. T. Diehl, J. P. Dietrich, P. Doel, C. E Cunha, T. F. Eifler, A. E. Evrard, A. Fausti Neto, E. Fernandez, B. Flaugher, P. Fosalba, C. Gangkof, E. Gaztanaga, D. Gerdes, D. Gruen, R. A. Gruendl, N. Gupta, C. Hennig, W. L. Holzapfel, K. Honscheid, B. Jain, D. James, K. Kuehn, N. Kuropatkin, O. Lahav, T. S. Li, H. Lin, M. A. G. Maia, M. March, J. L. Marshall, Paul Martini, M. McDonald, C.J. Miller, R. Miquel, B. Nord, R. Ogando, A. A. Plazas, C. L. Reichardt, A. K. Romer, A. Roodman, M. Sako, E. Sanchez, M. Schubnell, I. Sevilla, R. C. Smith, B. Stalder, A. A. Stark, V. Strazzullo, E. Suchyta, M. E. C. Swanson, G. Tarle, J. Thaler, D. Thomas, D. Tucker, V. Vikram, A. von der Linden, A. R. Walker, R. H. Wechsler, W. Wester, A. Zenteno, and K. Ziegler

2015, to be submitted to *Monthly Notices of the Royal Astronomical Society*

### ABSTRACT

We cross-match galaxy cluster candidates selected via their Sunyaev-Zel’dovich effect (SZE) signatures in  $129.1 \text{ deg}^2$  of the South Pole Telescope SPT-SZ survey with optically selected clusters selected from the Dark Energy Survey (DES) science verification data. We identify 25 clusters between  $0.1 \lesssim z \lesssim 0.8$  in the union of the SPT-SZ and redMaPPer (RM) samples. RM is an optical cluster finding algorithm that also returns a richness estimate for each cluster. We model the richness  $\lambda$ -mass relation with the following function  $\langle \ln \lambda | M_{500} \rangle \propto B_\lambda \ln M_{500} + C_\lambda \ln E(z)$  and use SPT-SZ cluster masses and RM richnesses  $\lambda$  to constrain the parameters. We find  $B_\lambda = 1.14^{+0.21}_{-0.18}$  and  $C_\lambda = 0.73^{+0.77}_{-0.75}$ . The associated scatter in mass at fixed richness is  $\sigma_{\ln M | \lambda} = 0.18^{+0.08}_{-0.05}$  at a characteristic richness  $\lambda = 70$ . We demonstrate that our model provides an adequate description of the matched sample, showing that the fraction of SPT-SZ selected clusters with RM counterparts is consistent with expectations and that the fraction of RM selected clusters with SPT-SZ counterparts, while lower than expected, exhibits no more than  $2\sigma$  tension with the predictions of our model. We model the optical-SZE cluster positional offset distribution with the sum of two Gaussians, showing that it is consistent with a dominant, centrally peaked population and a sub-dominant population characterized by larger offsets. We also cross-match the RM catalog with SPT-SZ candidates below the official catalog threshold significance  $\xi = 4.5$ , using the RM catalog to provide optical confirmation and redshifts for additional low- $\xi$  SPT-SZ candidates. In this way, we identify 15 additional clusters with  $\xi \in [4, 4.5]$  over the redshift regime explored by RM in the overlapping region between DES science verification data and the SPT-SZ survey.

**Key words:** galaxy clusters: general – galaxies: clusters: individual

### 3.1 Introduction

Clusters of galaxies were first identified as over-dense regions in the projected number counts of galaxies (e.g., Abell 1958; Zwicky et al. 1968). Nowadays, clusters are also regularly identified through their X-ray emission (e.g., Gioia et al. 1990; Vikhlinin et al. 1998; Böhringer et al. 2000; Pacaud et al. 2007; Šuhada et al. 2012) and at millimeter wavelengths through their Sunyaev-Zel'dovich effect (SZE) signatures (Sunyaev & Zel'dovich 1972). Large, homogeneously selected samples of clusters are useful for both cosmological and astrophysical studies, and such samples have recently begun to be produced using SZE selection (Staniszewski et al. 2009; Hasselfield et al. 2013; Planck Collaboration et al. 2015b; Bleem et al. 2015). There is a longer history of large cluster samples selected from optical and near infrared photometric surveys (e.g., Gladders & Yee 2000; Koester et al. 2007; Eisenhardt et al. 2008; Menanteau et al. 2010; Hao et al. 2010; Wen et al. 2012; Rykoff et al. 2014; Bleem et al. 2014; Ascaso et al. 2014, and references therein), and even larger samples will soon be available from ongoing and future surveys like the Dark Energy Survey (DES, The Dark Energy Survey Collaboration 2005)<sup>1</sup>, KiDS (de Jong et al. 2013), Euclid (Laureijs et al. 2011) and LSST (LSST Dark Energy Science Collaboration 2012).

Reliable estimates of galaxy cluster masses play a key role in both cosmological and astrophysical cluster studies. First, the abundance of galaxy clusters as a function of mass is a well-known cosmological probe (White et al. 1993; Bartlett & Silk 1994; Eke et al. 1998; Viana & Liddle 1999; Borgani et al. 2001; Vikhlinin et al. 2009b; Rozo et al. 2010; Mantz et al. 2010b; Allen et al. 2011; Benson et al. 2013; Bocquet et al. 2015b, and many others). Second, accurate estimates of cluster masses are crucial in disentangling environmental effects from the secular evolution processes shaping galaxy formation (Mei et al. 2009; Zenteno et al. 2011; Muzzin et al. 2012).

In this paper, we calibrate the richness-mass relation for SZE-selected galaxy clusters detected in the DES science verification data (SVA1) using the redMaPPer (Rykoff et al. 2014) cluster-finding algorithm. Specifically, we study the clusters detected via their SZE signatures in the South Pole Telescope SPT-SZ cluster survey (Bleem et al. 2015, hereafter B15) that are also present in the redMaPPer catalog. We also study the distribution of offsets between the SZE derived centers and the associated optical centers, properly including the SZE positional uncertainties. Finally, we demonstrate our ability to push to even lower candidate significance within the SPT-SZ candidate catalog by taking advantage of the contiguous, deep, multiband imaging available through DES. In this respect, our study points towards the combined use of DES and SPT datasets to provide highly reliable extended SZE-selected cluster samples. We note that historically the optical follow-up of SPT selected clusters was the original motivation for proposing DES.

The plan of the paper is as follows. In Section 3.2 we describe the galaxy cluster catalogs and the matching metric we use in this work. Section 3.3 describes the method we adopt to calibrate the SZE-mass and richness-mass relations. Our results are presented in Section 3.4. Section 3.5 contains a discussion of our findings and our conclusions. In the Appendix, we provide a preliminary analysis of a cluster sample created using an independent cluster finding algorithm — the Voronoi Tessellation (VT) cluster finder — which helps to highlight areas where the VT algorithm can be improved. Throughout this work, we adopt  $\Omega_M = 0.3$ ,  $\Omega_\Lambda = 0.7$ ,  $H_0 = 70 \text{ km s}^{-1} \text{ Mpc}^{-1}$ , and  $\sigma_8 = 0.8$ . Cluster masses are defined within  $R_{500}$ , the radius within which the density is 500 times the critical density of the Universe. Future analyses will include the dependence of the derived scaling relation parameters on the adopted cosmology by simultaneously fitting for cosmological and scaling-relation parameters (e.g. Mantz et al. 2010b; Rozo et al. 2010; Bocquet et al. 2015b).

---

<sup>1</sup><http://www.darkenergysurvey.org>

## 3.2 Cluster Sample

### 3.2.1 SPT-SZ Cluster Catalog

The SPT-SZ galaxy cluster sample used in this analysis has been selected via the cluster thermal SZE signatures in the  $2365 \text{ deg}^2$  SPT-SZ survey using 95 GHz and 150 GHz data. Typical instrumental noise is approximately  $40$  ( $18$ )  $\mu K\text{-arcmin}$  and the beam FWHM is  $1.6$  ( $1.19$ ) arcmin for the 95 (150) GHz maps. We use a multi-frequency matched filter to extract the cluster SZE signal in a manner designed to optimally measure the cluster signal given knowledge of the cluster profile, the SZE spectrum and the noise in the maps (Haehnelt & Tegmark 1996; Melin et al. 2006). The cluster gas profiles are assumed to be described by a projected isothermal  $\beta$  model (Cavaliere & Fusco-Femiano 1976) with  $\beta = 1$ . Note that, as discussed in Vanderlinde et al. (2010), the resulting SPT-SZ candidate catalogs are not sensitive to this assumption. The adopted model provides a SZE temperature decrement that is maximum at the cluster center and weakens with separation  $\theta$  from the cluster centre as:

$$\Delta T(\theta) = \Delta T_0 [1 + (\theta/\theta_c)^2]^{-1}, \quad (3.1)$$

where  $\Delta T_0$  is the central value and  $\theta_c$  is the core radius. We adopt 12 different cluster profiles linearly spaced from  $\theta_c = 0.25$  to  $3$  arcmin (Vanderlinde et al. 2010; Reichardt et al. 2013, B15). For each cluster, the maximum signal-to-noise across the 12 filtered maps is denoted as  $\xi$ . The SPT-SZ cluster candidates with  $\xi > 4.5$  have been previously published in B15.

### 3.2.2 DES Optical Cluster Catalogs

The DES Science Verification Data (DES-SVA1) that overlap SPT have been used to produce optically selected catalogs of clusters. In Section 3.2.2 we describe the acquisition and preparation of the DES-SVA1 data, and in Section 3.2.2 we describe the production of the redMaPPer cluster catalog used in the primary analysis. We remind the reader that in Appendix 3.6 we present results of a preliminary analysis of the VT cluster catalog.

#### DES-SVA1 Data

The DES-SVA1 data include imaging of  $\sim 300 \text{ deg}^2$  over multiple disconnected fields (Melchior et al. 2014; Sánchez et al. 2014; Banerji et al. 2015), most of which overlap with the SPT-SZ survey. The DES-SVA1 data were acquired with the Dark Energy Camera (Diehl & For Dark Energy Survey Collaboration 2012; Flaugher et al. 2012, 2015) over 78 nights, starting in Fall 2012 and ending early in 2013. The data have a range in depth, up to the nominal depth of the full DES survey (Rykoff et al., in preparation).

Data have been processed through the DES Data Management (DESDM, Desai et al. 2012) pipeline that is an advanced version of development versions described in several publications (Ngeow et al. 2006; Mohr et al. 2008, 2012). The data were calibrated in several stages leading to a *Gold* catalog of DES-SVA1 galaxies (Rykoff et al., in preparation). The *Gold* catalog covers  $\sim 250 \text{ deg}^2$  and is optimized for extragalactic science. In particular it masks regions south of declination  $\delta = -61^\circ$ , avoiding the Large Magellanic Cloud and its high stellar densities. Furthermore, the footprint is restricted to the regions where we have coverage in all four bands.

#### redMaPPer Cluster Catalog

The red-sequence Matched-Filter Probabilistic Percolation (redMaPPer, hereafter RM) algorithm is a cluster-finding algorithm based on the richness estimator of Rykoff et al. (2012). RM has been applied to photometric data from the Eighth Data Release (DR8) of the Sloan Digital Sky Survey (Aihara et al. 2011, SDSS,) and to the SDSS Stripe 82 coadd data (Annis et al. 2014), and has been shown to provide excellent photometric redshifts, richness estimates that tightly correlate with external mass proxies, and very good completeness and

purity (Rozo & Rykoff 2014; Rozo et al. 2014b,c). We refer the reader to the paper by Rykoff et al. (2014) for a detailed description of the algorithm. Here, we briefly summarize the most salient features.

We employ an updated version of the algorithm (v6.3.3), with improvements summarized in Rozo & Rykoff (2014), Rozo et al. (2015, in preparation), and Rykoff et al. (2015, in preparation). RM calibrates the colour of red-sequence galaxies using galaxy clusters with spectroscopic redshifts. RM uses this information to estimate the membership probability of every galaxy in the vicinity of a galaxy cluster. The richness  $\lambda$  is thus defined as the sum of the membership probabilities ( $p_{RM}$ ) over all galaxies:

$$\lambda = \sum p_{RM}. \quad (3.2)$$

In addition to the estimate of membership probabilities, the RM centering algorithm is also probabilistic. With the assumption that there is a cluster galaxy at the center, we can estimate centering probabilities using a luminosity filter, a photometric redshift filter, and a local density filter. These probabilities have been tested on SDSS DR8 data using X-ray selected galaxy clusters, and have been shown to produce cluster centers that are consistent with the X-ray centers (Rozo & Rykoff 2014).

The DES-SVA1 RM catalog was produced by running on a smaller footprint than that for the full SVA1 *Gold* sample. In particular, we restrict the catalog to the regions where the  $z$ -band  $10\sigma$  galaxy limiting magnitude is  $z > 22$ . In total, we use  $148 \text{ deg}^2$  of DES-SVA1 imaging, with  $129.1 \text{ deg}^2$  overlapping the SPT-SZ footprint. In this area, the largest fraction ( $124.6 \text{ deg}^2$ ) is included in the so called DES-SVA1 SPT-E field. The final catalog used in this work consists of 9281 clusters with  $\lambda > 5$  and redshifts in the range  $0.1 < z < 0.9$ . Due to the varying depth of the DES-SVA1 catalog, RM produces a mask that determines the maximum redshift of the cluster search at any given location in the survey. As an example, the effective area in the SPT-E region at the highest redshift ( $z > 0.85$ ) is only  $\sim 30 \text{ deg}^2$ . In addition to the cluster catalog, the RM algorithm also uses the survey mask to produce a set of random points with the same richness and redshift distribution as the clusters in the catalog. The random points take into account the survey geometry and the physical extent of the clusters, and as with the clusters, only includes points that have  $< 20\%$  of the local region masked (see Rykoff et al. 2014).

### 3.2.3 Catalog Matching

We cross-match the SPT-SZ catalog with the RM optical cluster catalog following the method of Rozo et al. (2014c). First, we sort the SPT-SZ clusters to produce a list with decreasing SZE observable  $\xi$ , and we sort the RM catalog to produce a list with decreasing richness. Second, we go down the SPT-SZ sorted list, associating each SPT cluster candidate with the richest RM cluster candidate whose centre lies within  $1.5 R_{500}$  of the SZE centre. Third, we remove the associated RM cluster from the list of possible counterparts when matching the remaining SPT-selected clusters.

$R_{500}$  is first computed assuming the redshift of the optical counterpart and using the SZE-mass scaling relation parameters adopted in B15. We subsequently check that our sample does not change when adopting our best fitting scaling relation parameters (see Section 3.3.1).

To test the robustness of our matching algorithm against chance associations, we first perform the above described procedure on a sample of randomly generated RM clusters as described in the previous Section. Positions of clusters in this randomly generated sample do not correlate with the positions of the SPT-SZ clusters. Using an ensemble of  $10^4$  random catalogs we measure the distribution of richness in chance associations for each SPT-SZ candidate. In Figure 3.1 (left panel) we show the resulting 84% and 97.5% confidence limits (solid and dotted lines, respectively) in the richness distribution of the chance associations as a function of the SPT-SZ observable  $\xi$ . This test allows us to estimate the probability of chance superposition for each SPT-SZ cluster candidate. As detailed below, we use this information to determine whether or not to include particular matches for further analysis. As Figure 3.1 shows, this filtering of the matched sample then ensures that chance superpositions are playing no more than a minor role even at  $4 < \xi < 4.5$ .

We then apply the algorithm to match the real RM cluster catalog with the SPT-SZ candidate list where  $\xi > 4.5$ . Within the DES-SVA1 region explored by RM there are 36 such SPT-SZ cluster candidates. Using

information on the contamination fraction at  $\xi > 4.5$  of the SPT-SZ candidate list and on the redshift distribution of the confirmed cluster candidates (Song et al. 2012b, B15), we expect  $\sim 9$  of these candidates to be noise fluctuations and  $\sim 80\%$  of the real clusters to lie at  $z < 0.8$ . Therefore, assuming the optical catalog is complete, the expected number of real cluster matches is  $\sim 22$ . Similarly, one can estimate an expected number of real cluster matches (23.6) by scaling the total number of confirmed clusters in B15 below  $z = 0.8$  (433) in the  $2365 \text{ deg}^2$  of the SPT-SZ survey by the DES-SVA1 area overlapping SPT-SZ that has been processed with the RM cluster finder ( $129.1 \text{ deg}^2$ ).

The actual number of matches to the SPT-SZ candidates is 33. Eight systems are foreground, low-richness RM clusters that have been erroneously associated with SPT-SZ candidates with either previously measured redshifts (four systems) or lower limits estimated in B15 (the remaining four candidates) that are at  $z \gtrsim 0.8$ ; these systems are either noise fluctuations or real clusters that are at redshifts too high for them to be detected by RM. In fact, all of these systems have a probability  $p$  of chance associations estimated from the randomly generated sample that is  $p > 84\%$ . Therefore, we remove these matches from the sample. This leaves 25 SPT-SZ candidates at  $\xi > 4.5$  that have RM counterparts, and the expectation is that within this sample of 25 candidates there is less than one false association. The associated optical richness as a function of the SPT-SZ significance is shown in the left panel of Figure 3.1. This number is somewhat larger but statistically consistent with the expected number of matches presented above. All 22 of the SPT-SZ confirmed clusters presented in B15 that lie at redshifts where they could be detected by RM are in this matched sample. According to our matching metric (which differs from the approach in B15) there are also three unconfirmed SPT-SZ candidates (i.e., candidates without identified optical counterparts in the B15 analysis) that have RM counterparts: SPT-CL J0502-6048, SPT-CL J0437-5307 and SPT-CL J0500-4551. The newly confirmed clusters are highlighted with large circles in Figure 3.1.

Of the 25 SPT-SZ candidates with robust RM counterparts, we use 19 of them to calibrate the RM richness-mass relation. Six clusters are excluded from the analysis for the following reasons. Clusters with estimated redshift  $z < 0.25$  in the SPT-SZ catalog from B15 are highlighted in cyan in the left panel of Figure 3.1. Because the  $\xi$ -mass relation is robust only above this redshift (Vanderlinde et al. 2010), these systems are not used in the following analysis. Two systems (SPT-CL J0440-4744 and SPT-CL J0441-4502) are excluded from this analysis as they are detected in SPT-SZ regions that have been masked due to their proximity to point sources, which can compromise the SZE signal-to-noise measurement. In addition, we exclude the three clusters highlighted in magenta: SPT-CL J0417-4748, SPT-CL J0456-5116 and SPT-CL J0502-6048. These systems are strongly masked in the DES-SVA1 data; based on the SZE position, the masks cover 40% of the total cluster region. As a result, the associated optical counterparts are highly mis-centered, and the corresponding richness is severely biased. We note that the average centering failure rate caused by the detection mask is 12% (3 clusters out of 25), in comparison to the corresponding rate in the SDSS RM catalog, which is  $\approx 1\% - 2\%$ . The difference reflects the fact that SDSS has a much larger contiguous area, as well as the more aggressive star mask that is used in SVA1. We expect this failure rate will decrease as the DES coverage increases, and object masking improves. Furthermore, improvements will be made to the RM algorithm to estimate the masked area not only at the putative center of the cluster, but at all possible centers. In this way, clusters at high risk of mask-induced mis-centering will be properly removed from the sample.

The B15 catalog contains only SPT-SZ candidates with  $\xi \geq 4.5$ . In this work we also apply the matching algorithm to SPT-SZ candidates at  $4 < \xi < 4.5$ . We identify 26 matches in this signal to noise range. Similarly to the  $\xi > 4.5$  case, we exclude 11 of these systems, which have estimated probabilities  $p$  of chance associations  $p > 84\%$ . For the 15 matched systems, the expected number of false associations is also smaller than one. The remaining *cleaned* sample is shown as red points on the left panel of Figure 3.1. The resulting total number of SPT-SZ and RM associations at  $\xi > 4$  is 40. This number is in good agreement with the expectation ( $\sim 36$ ) obtained using the number of SPT-candidates above  $\xi > 4$  in the DES-SVA1 region explored by RM (88) and correcting it by the expected number of noise fluctuations ( $\sim 45$ ) and the number of clusters above  $z > 0.8$  ( $\sim 7$ ). We find that two  $\xi < 4.5$  SPT-SZ candidates, SPT-CL J0501-4717 and SPT-CL J0439-5611, have probabilities of random associations larger than 5%, and therefore it is not clear whether these low richness associations are correct (see Figure 3.1).

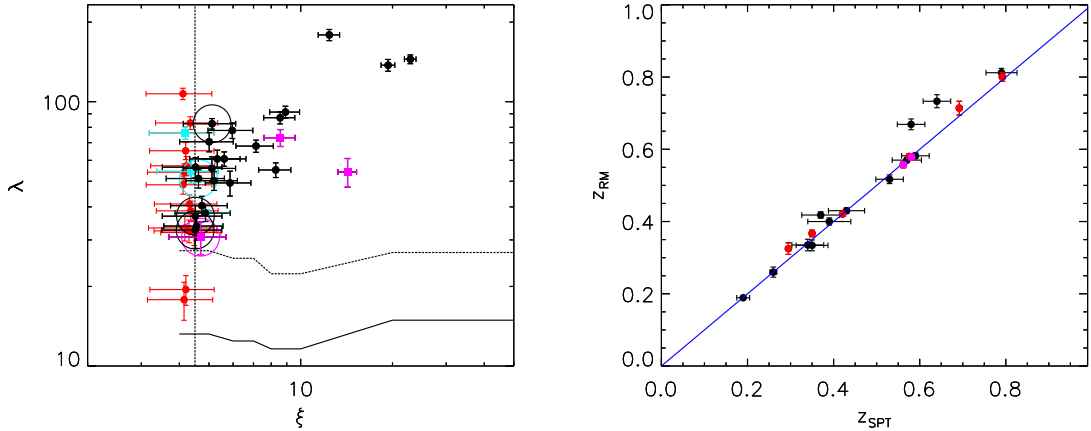


Figure 3.1 *Left panel*: Richness as a function of the SZE significance  $\xi$  for the matched cluster sample. SPT-SZ candidates with  $\xi < 4.5$  (vertical line) are shown in red. Clusters at  $z < 0.25$  (cyan) and clusters with miscentering due to a high masked fraction (magenta) are not used in the richness analysis. Large circles indicate the newly confirmed SPT-SZ candidates with  $\xi > 4.5$ . Solid and dashed lines represent the upper 84 and 97.5 percentiles in richness of chance associations of SPT-SZ candidates and clusters from the randomly generated RM catalog. *Right panel*: The estimated redshift for the RM sample as a function of SPT redshifts as presented in B15 from independent optical follow-up data. SPT-SZ candidates with spectroscopic redshift are shown in red. Magenta symbols are the same as in the left panel.

The right panel of Figure 3.1 contains a comparison of the redshifts from the RM catalogs with the redshifts published in B15 ( $z_{\text{SPT}}$ ) for the same clusters (obtained through dedicated optical/NIR followup by the SPT team or taken from the literature). Clusters with spectroscopic redshifts are highlighted in red. We note that the redshift estimates are not biased for the clusters affected by masking (magenta points). For SPT-SZ candidates with  $4 < \xi < 4.5$  the SPT collaboration did not complete followup optical imaging, and therefore we adopt the redshifts of the RM optical cluster counterpart.

Table 3.1 contains all SPT candidates with RM counterparts used in this work. For newly confirmed SPT-SZ clusters, the associated  $z_{\text{SPT}}$  redshift is not given. We caution that the masses for low-redshift clusters ( $z < 0.25$ ) may be underestimated due to filtering that is done to remove the noise component associated with the primary CMB.

### 3.3 Mass Calibration Method

We apply the method described in Bocquet et al. (2015b) to characterize the  $\lambda$ -mass relation of SPT-selected clusters. We refer the reader to the original paper for a detailed description of the method. A similar approach has been adopted by Liu et al. (2015) for studying the SZE properties of an X-ray selected cluster sample from the XMM-BCS survey (Šuhada et al. 2012; Desai et al. 2012). In this analysis, we consider the RM richness as a follow-up observable to the SZE-selected cluster sample. This choice is adequate as there are no SPT-SZ candidates with  $\xi > 4.5$  missing RM counterparts in the redshift and spatial regime explored by the RM catalog, so that the cross-sample can indeed be thought of as solely SPT-selected. We note that this is not the case for SPT-SZ candidates with  $4 < \xi \leq 4.5$  that do not have RM counterparts. However, the adopted method is also accurate under the assumption that cross-matching the SPT-SZ candidate list with the RM cluster catalog *cleans* the SPT-SZ candidate list, removing the expected noise fluctuations. Within this context the resulting cluster sample is therefore drawn from the halo mass function through the SPT-SZ selection in the redshift

Table 3.1 SPT-SZ cluster candidates with RM counterpart. We report the SPT-ID (1), right ascension (2) and declination (3), SPT peak detection significance  $\xi$  (4), corresponding core radius (5), richness  $\lambda$  (6), associated redshift from the RM catalog (7) and SPT catalog (8), and SPT derived masses (9). Coordinates are J2000.

SPT ID	R.A.	DEC	$\xi$	$\theta_c$ [arcmin]	$\lambda$	$z_{\text{RM}}$	$z_{\text{SPT}}$	$M_{500} [10^{14} h_{70}^{-1} M_{\odot}]$
SPT-CL J0438-5419	69.574	-54.319	22.88	0.50	$144.76 \pm 5.52$	$0.42 \pm 0.01$	0.42	$10.19 \pm 1.33$
SPT-CL J0040-4407	10.199	-44.133	19.34	0.50	$137.45 \pm 7.03$	$0.37 \pm 0.01$	0.35	$9.71 \pm 1.28$
SPT-CL J0417-4748	64.344	-47.812	14.24	0.25	$54.22 \pm 6.75$	$0.58 \pm 0.01$	0.58	$7.41 \pm 1.00$
SPT-CL J0516-5430	79.149	-54.510	12.41	1.50	$178.93 \pm 8.71$	$0.33 \pm 0.02$	0.29	$7.05 \pm 0.97$
SPT-CL J0449-4901	72.273	-49.023	8.91	0.50	$91.37 \pm 4.75$	$0.80 \pm 0.01$	0.79	$5.24 \pm 0.78$
SPT-CL J0456-5116	74.115	-51.275	8.58	1.00	$73.08 \pm 5.39$	$0.56 \pm 0.01$	0.56	$5.39 \pm 0.81$
SPT-CL J0441-4855	70.450	-48.917	8.56	0.50	$86.96 \pm 4.55$	$0.81 \pm 0.01$	$0.79 \pm 0.04$	$5.10 \pm 0.77$
SPT-CL J0439-4600	69.807	-46.012	8.28	0.25	$55.18 \pm 3.52$	$0.34 \pm 0.02$	$0.34 \pm 0.04$	$5.52 \pm 0.84$
SPT-CL J0440-4657	70.229	-46.964	7.13	1.25	$67.95 \pm 3.62$	$0.33 \pm 0.02$	$0.35 \pm 0.04$	$4.95 \pm 0.81$
SPT-CL J0447-5055	71.843	-50.921	5.97	0.25	$77.84 \pm 5.26$	$0.40 \pm 0.01$	$0.39 \pm 0.05$	$4.24 \pm 0.81$
SPT-CL J0422-5140	65.591	-51.674	5.86	1.00	$49.28 \pm 5.32$	$0.58 \pm 0.01$	$0.59 \pm 0.03$	$3.98 \pm 0.78$
SPT-CL J0439-5330	69.928	-53.502	5.61	0.75	$60.77 \pm 3.81$	$0.43 \pm 0.01$	$0.43 \pm 0.04$	$3.97 \pm 0.81$
SPT-CL J0433-5630	68.249	-56.502	5.32	1.75	$60.75 \pm 4.82$	$0.71 \pm 0.02$	0.69	$3.56 \pm 0.78$
SPT-CL J0535-5956	83.791	-59.939	5.20	0.25	$50.25 \pm 4.09$	$0.67 \pm 0.02$	$0.58 \pm 0.03$	$3.46 \pm 0.77$
SPT-CL J0440-4744	70.242	-47.736	5.12	1.25	$82.55 \pm 3.80$	$0.30 \pm 0.02$	—	$3.75 \pm 0.83$
SPT-CL J0428-6049	67.026	-60.828	5.11	1.25	$55.91 \pm 5.95$	$0.73 \pm 0.02$	$0.64 \pm 0.03$	$3.46 \pm 0.79$
SPT-CL J0444-4352	71.162	-43.872	5.01	1.50	$70.53 \pm 5.91$	$0.57 \pm 0.01$	$0.57 \pm 0.03$	$3.53 \pm 0.82$
SPT-CL J0458-5741	74.598	-57.695	4.87	2.50	$37.90 \pm 2.68$	$0.19 \pm 0.00$	$0.19 \pm 0.02$	$3.69 \pm 0.85$
SPT-CL J0534-5937	83.606	-59.625	4.74	0.25	$40.43 \pm 3.42$	$0.58 \pm 0.01$	0.58	$3.15 \pm 0.76$
SPT-CL J0502-6048	75.724	-60.810	4.69	0.25	$30.73 \pm 4.32$	$0.79 \pm 0.02$	—	$3.03 \pm 0.76$
SPT-CL J0441-4502	70.345	-45.040	4.62	2.50	$51.22 \pm 4.11$	$0.15 \pm 0.01$	—	$3.49 \pm 0.85$
SPT-CL J0429-5233	67.430	-52.559	4.56	0.75	$33.84 \pm 3.97$	$0.52 \pm 0.01$	$0.53 \pm 0.03$	$3.15 \pm 0.79$
SPT-CL J0452-4806	73.002	-48.108	4.52	0.50	$56.54 \pm 4.89$	$0.42 \pm 0.01$	$0.37 \pm 0.04$	$3.26 \pm 0.81$
SPT-CL J0437-5307	69.259	-53.119	4.51	0.25	$36.89 \pm 3.56$	$0.29 \pm 0.02$	—	$3.20 \pm 0.80$
SPT-CL J0500-4551	75.209	-45.856	4.51	0.75	$32.68 \pm 4.82$	$0.26 \pm 0.01$	—	$3.66 \pm 0.91$
SPT-CL J0453-5027	73.307	-50.451	4.47	0.25	$31.99 \pm 3.44$	$0.77 \pm 0.02$	—	$2.89 \pm 0.74$
SPT-CL J0449-4440	72.473	-44.672	4.37	0.75	$54.50 \pm 5.43$	$0.15 \pm 0.00$	—	$3.42 \pm 0.86$
SPT-CL J0423-5506	65.809	-55.104	4.36	1.25	$38.65 \pm 3.44$	$0.27 \pm 0.02$	—	$3.26 \pm 0.83$
SPT-CL J0451-5057	72.937	-50.965	4.34	0.50	$83.11 \pm 4.62$	$0.76 \pm 0.01$	—	$2.81 \pm 0.74$
SPT-CL J0438-4629	69.564	-46.488	4.31	0.50	$41.01 \pm 3.37$	$0.43 \pm 0.01$	—	$3.07 \pm 0.79$
SPT-CL J0456-4531	74.099	-45.523	4.30	0.25	$32.45 \pm 3.18$	$0.29 \pm 0.02$	—	$3.17 \pm 0.81$
SPT-CL J0431-5353	67.970	-53.896	4.22	0.50	$57.23 \pm 4.76$	$0.75 \pm 0.02$	—	$2.74 \pm 0.73$
SPT-CL J0501-4717	75.274	-47.294	4.20	3.00	$19.47 \pm 2.50$	$0.35 \pm 0.02$	—	$3.34 \pm 0.88$
SPT-CL J0518-5740	79.507	-57.670	4.19	0.25	$65.22 \pm 4.82$	$0.82 \pm 0.01$	—	$2.60 \pm 0.70$
SPT-CL J0438-4907	69.655	-49.117	4.19	1.75	$76.20 \pm 4.16$	$0.24 \pm 0.01$	—	$3.13 \pm 0.81$
SPT-CL J0513-5901	78.273	-59.029	4.17	0.25	$33.29 \pm 3.58$	$0.61 \pm 0.01$	—	$2.75 \pm 0.73$
SPT-CL J0451-4910	72.888	-49.178	4.14	0.25	$54.10 \pm 4.10$	$0.73 \pm 0.02$	—	$2.71 \pm 0.73$
SPT-CL J0439-5611	69.978	-56.192	4.14	0.50	$17.82 \pm 2.93$	$0.28 \pm 0.02$	—	$3.10 \pm 0.81$
SPT-CL J0532-5752	83.237	-57.877	4.11	0.50	$48.49 \pm 3.81$	$0.77 \pm 0.02$	—	$2.59 \pm 0.71$
SPT-CL J0449-5908	72.472	-59.142	4.11	1.25	$107.14 \pm 5.29$	$0.77 \pm 0.01$	—	$2.68 \pm 0.73$

range explored by the RM catalog.

In the following subsections we describe the model we use to simultaneously constrain the SZE-mass relation (Section 3.3.1) and the richness-mass relation (Section 3.3.2).

### 3.3.1 The SZE-mass Relation

Following previous SPT papers (Vanderlinde et al. 2010; Benson et al. 2013; Reichardt et al. 2013; Bocquet et al. 2015b, B15), we define the unbiased SZE significance  $\zeta$  as the average signal-to-noise a cluster would produce over many realizations of SPT data, if the cluster position and core radius were perfectly known. This quantity is related to the expectation value of  $\xi$  over many realizations of the SPT data by:

$$\zeta = \sqrt{\langle \xi \rangle^2 - 3}, \quad (3.3)$$

where the bias in  $\langle \xi \rangle$  is due to maximizing the signal-to-noise over three variables (cluster right ascension, declination, and core radius). The scatter of the actual observable  $\xi$  with respect to  $\langle \xi \rangle$  is characterized by a Gaussian of unit width. The SPT observable-mass relation  $P(\zeta|M_{500}, z)$  is modeled as a log-normal distribution of mean

$$\langle \ln \zeta | M_{500}, z \rangle = \ln A_{\text{SZE}} + B_{\text{SZE}} \ln \left( \frac{M_{500}}{3 \times 10^{14} h^{-1} M_\odot} \right) + C_{\text{SZE}} \ln \left( \frac{E(z)}{E(z=0.6)} \right) \quad (3.4)$$

and scatter  $D_{\text{SZE}}$ , and where  $E(z) \equiv H(z)/H_0$ . At low significance  $\zeta \lesssim 2$ , there is a non-negligible chance of multiple low-mass clusters overlapping within the same resolution element of the SPT beam. We account for this by only considering the brightest of these objects per approximate resolution element and we compute  $P(\zeta_{\max}|\zeta)$  following Crawford et al. (2010). The SPT observable-mass relation is therefore expanded to  $P(\zeta_{\max}|\zeta)P(\zeta|M_{500}, z)$  and  $\zeta_{\max}$  is then converted to the observable  $\xi$  as in Eq. 3.

To calibrate the  $\zeta$ - $M$  relation we use the subsample of clusters with  $\xi > 5$  and  $z > 0.25$  from the 2365 deg<sup>2</sup> SPT-SZ catalog (B15). We determine the parameter values by abundance-matching the catalog against our fixed reference cosmology. We predict the expected number of clusters as a function of mass and redshift using the halo mass function (Tinker et al. 2008). We convolve this mass function with the observable-mass relation accounting for its associated uncertainties, and compare the prediction with the data. Our approach here is effectively the opposite of the typical analysis, where cosmological parameters are deduced from the cluster sample using both priors and calibrating information to constrain the scaling relation parameters (e.g. Benson et al. 2013; Bocquet et al. 2015b); here, we assume perfect knowledge of cosmology to calibrate the scaling relation. Note that this method does not depend on any assumptions about hydrostatic equilibrium.

We assume flat priors on  $A_{\text{SZE}}$ ,  $B_{\text{SZE}}$ ,  $C_{\text{SZE}}$  and a Gaussian prior on  $D_{\text{SZE}} = 0.18 \pm 0.07$ ; the latter corresponds to the posterior distribution derived from the cosmological analysis of the full SPT sample (de Haan et al., in preparation). We obtain the following parameters for the  $\zeta$ -mass relation by maximizing the likelihood of obtaining the observed sample in  $\xi$  and redshift under the model derived from Eq. 3-5. The results are

$$\begin{aligned} A_{\text{SZE}} &= 4.02 \pm 0.16, B_{\text{SZE}} = 1.71 \pm 0.09, \\ C_{\text{SZE}} &= 0.49 \pm 0.16, D_{\text{SZE}} = 0.20 \pm 0.07. \end{aligned} \quad (3.5)$$

For every cluster in the sample we also calculate the associated mass distribution, accounting for selection effects:

$$P(M_{500}|\xi, z, \vec{p}) \propto P(\xi|M_{500}, z, \vec{p}) P(M_{500}|z, \vec{p}), \quad (3.6)$$

where the vector  $\vec{p}$  encapsulates cosmological and scaling relation parameters and  $P(\xi|M_{500}, z, \vec{p})$  is obtained from the  $\xi$ -mass scaling relation as described by Eq. 3.3 and 3.4. The halo mass function  $P(M_{500}|z, \vec{p})$  is the prior on the mass distribution at redshift  $z$ .

Masses derived for the matched cluster sample are shown in Table 1. We note that both these masses and the SZE scaling relation parameters quoted here are different from the ones reported in B15. We adopt the same fixed cosmology as in B15, but in this analysis we consider data from the full 2365 deg<sup>2</sup> SPT-SZ survey as opposed to just the sample from the initial 720 deg<sup>2</sup> (Reichardt et al. 2013).

Table 3.2 Best fitting parameters and 68% confidence level of the richness-mass scaling relation parameters described by Equation 3.7 and 3.8.

Catalog	$A_\lambda$	$B_\lambda$	$C_\lambda$	$D_\lambda$
SPT-SZ+RM $\xi > 4.5$	$66.1^{+6.3}_{-5.9}$	$1.14^{+0.21}_{-0.18}$	$0.73^{+0.77}_{-0.75}$	$0.15^{+0.10}_{-0.07}$
SPT-SZ+RM $\xi > 4$	$69.8^{+6.0}_{-4.9}$	$1.17^{+0.19}_{-0.17}$	$1.71^{+0.63}_{-0.57}$	$0.20^{+0.09}_{-0.08}$

### 3.3.2 Richness-mass Relation

As for the SZE-mass relation (Eq.3.4), we assume a power law form for the  $\lambda$ -mass relation:

$$\langle \ln \lambda | M_{500}, z \rangle = \ln A_\lambda + B_\lambda \ln \left( \frac{M_{500}}{3 \times 10^{14} h^{-1} M_\odot} \right) + C_\lambda \ln \left( \frac{E(z)}{E(z=0.6)} \right) \quad (3.7)$$

where  $A_\lambda$  is the normalization,  $B_\lambda$  characterizes the mass dependence, and  $C_\lambda$  characterizes the redshift evolution. An additional parameter  $D_\lambda$  describes the intrinsic scatter in  $\lambda$ , which is assumed to be log-normal and uncorrelated with the SZE scatter, with variance given by:

$$\text{Var}(\ln \lambda | M_{500}) = \exp(-\langle \ln \lambda | M_{500} \rangle) + D_\lambda^2. \quad (3.8)$$

The first term above represents the Poisson noise associated with the number of galaxies in a halo at fixed mass, and therefore we define the intrinsic scatter  $D_\lambda$  as log-normal scatter in addition to Poisson noise. We assume flat priors on the distributions of  $A_\lambda$ ,  $B_\lambda$ ,  $C_\lambda$  and a positive flat prior for  $D_\lambda$ .

The probability that a cluster with SPT-SZ signal-to-noise  $\xi$  is observed to have a richness  $\lambda$  is

$$P(\lambda | \xi, z, \vec{p}) = \int dM_{500} P(\lambda | M_{500}, z, \vec{p}) P(M_{500} | \xi, z, \vec{p}). \quad (3.9)$$

The term  $P(\lambda | M_{500}, z, \vec{p})$  contains the lognormal intrinsic scatter and normal measurement uncertainties in the observable  $\lambda$ . We use the above distribution to evaluate the likelihood of the matched cluster sample defined through our cross-matching procedure. Note that we simultaneously vary both the optical and SZE scaling relation parameters, further including the SZE data set from B15 with  $\xi > 5$ ,  $z > 0.25$  for constraining the SZE-mass relation.

## 3.4 Results

We present here the constraints on the richness-mass relation (Section 3.4.1) and then use these best fit parameters to explore whether the cumulative distribution of the matched samples are consistent with the expectations from the model (Section 3.4.2). Finally, in Section 3.4.3 we analyse the optical-SZE positional offset distribution.

### 3.4.1 redMaPPer Richness-mass Relation

We marginalize over the SZE-mass scaling relation parameters and constrain the posterior distributions for the RM  $\lambda$ -mass scaling relation. Our best fit parameters and 68% confidence level intervals are reported in Table 3.2 and shown in Figure 3.2. We note that the slope of the  $\lambda$ -mass relation is consistent with 1 within  $1\sigma$  and the model is consistent with no redshift evolution within  $1\sigma$  (Andreon & Congdon 2014). Furthermore the resulting  $\lambda$ -mass relation is characterized by a remarkably low asymptotic intrinsic scatter, with  $\sigma_{\ln \lambda | M_{500}} \rightarrow 0.15^{+0.10}_{-0.07}$  as  $\langle \ln \lambda | M_{500} \rangle \rightarrow \infty$  (Eq. 3.8). Following Evrard et al. (2014), we estimate the characteristic scatter in mass at fixed richness to arrive at  $\sigma_{\ln M} = 0.18^{+0.08}_{-0.05}$  at  $\lambda = 70$ ,  $\sim 25\%$  larger than the corresponding characteristic scatter in mass at fixed  $\xi$ . We present in Figure 3.3 the RM richness as a function of the SPT derived masses. Colour

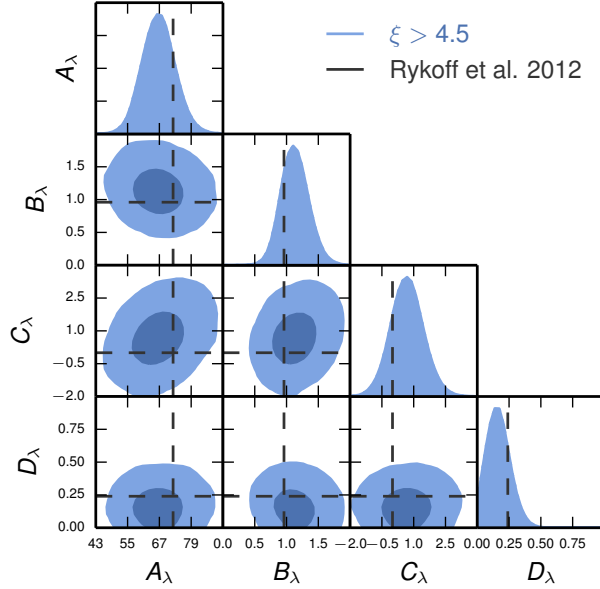


Figure 3.2 Posterior distribution for the four parameters of the  $\lambda$ -mass scaling relation (Equations 3.7 and 3.8). Predictions from the scaling relation of Rykoff et al. (2012) are shown as dashed black lines. Best fitting parameters and associated  $1\sigma$  uncertainties appear in Table 3.2.

coding of the data points is as in the left panel of Figure 3.1. Blue lines describe the best fitting model and intrinsic scatter as derived from this analysis (Table 2) at a pivot point of  $z = 0.6$ .

We have verified that our results are not dominated by uncertainties in the SZE-mass scaling relation by fixing these parameters to their best fit values. Our results are only marginally improved in this case. Consequently, future analyses with larger samples are expected to considerably reduce the uncertainties of the recovered  $\lambda$ -mass scaling relation parameters.

In Figure 3.3, two  $\xi > 4.5$  clusters appear to be obvious outliers: SPT-CL J0417-4725 ( $\xi = 14.2$ ,  $\lambda = 54.2$ ,  $M_{500} = 7.41 \times 10^{14} h_{70}^{-1} M_\odot$ ) and SPT-CL J0516-5435 ( $\xi = 12.4$ ,  $\lambda = 178.9$ ,  $M_{500} = 7.05 \times 10^{14} h_{70}^{-1} M_\odot$ ). SPT-CL J0417-4725 is one of the clusters that we removed from our analysis because of the cluster being highly masked. SPT-CL J0516-5345 is a well-known merger that is elongated in a north-south direction in the plane of the sky with an X-ray mass estimate nearly a factor of two larger than the SZE mass estimate. This cluster was in fact the strongest outlier in the sample of 14 clusters in Andersson et al. (2010). High et al. (2012) made a weak lensing measurement of SPT-CL J0516-5345, and found that there was a significant offset between the brightest central galaxy (BCG) and the weak-lensing center, consistent with the merger hypothesis. Additionally, High et al. (2012) found that the weak-lensing mass was in better agreement with the SZE-mass estimate than the X-ray mass estimate, at a level consistent with elongation observed in the plane of the sky. Therefore, SPT-CL J0516-5345 appears to be an outlier due to true intrinsic scatter in the observable-mass relations, so we leave it in our analysis. We note, however, that whether or not we include SPT-CL J0516-5345 in the fit has a significant impact on our results. Our best fit parameters shift from  $B_\lambda = 1.14^{+0.21}_{-0.18}$  and  $D_\lambda = 0.15^{+0.10}_{-0.07}$  with this cluster, to  $B_\lambda = 1.00^{+0.17}_{-0.15}$  and  $D_\lambda = 0.05^{+0.07}_{-0.03}$  when SPT-CL J0516-5345 is not included in the fit. Whether SPT-CL J0516-5345 represents a rare event in a non-Gaussian tail in the distribution of richness of galaxy clusters or the recovered log-normal scatter obtained when cluster SPT-CL J0516-5349 is included is more correct will thus need to await future analyses with larger samples.

We convert the  $P(M_{500}|\lambda)$  scaling relation derived by Rykoff et al. (2012) using abundance matching and

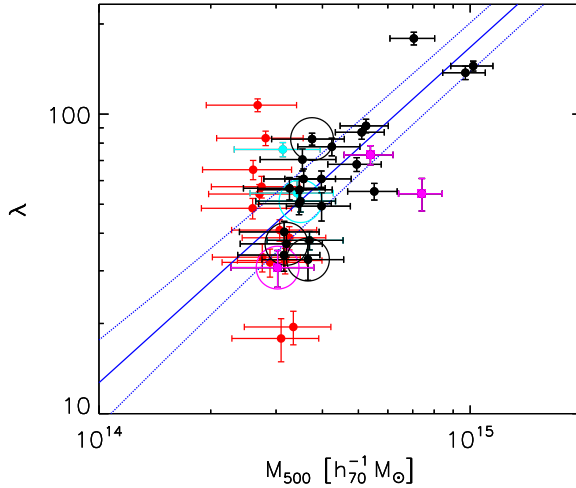


Figure 3.3 Richness as a function of the SPT derived masses. Blue lines show the best fit richness mass relation and  $1\sigma$  intrinsic scatter. Colour coding and symbols are the same as in the left panel of Figure 1.

the SDSS RM catalog to a richness–mass relation so that we can compare it to our results (see also Evrard et al. 2014). The predictions from Rykoff et al. (2012) are shown as dashed lines in Figure 3.2 under the assumption of no redshift evolution in the richness–mass relation. We note that all parameters of our derived RM  $\lambda$ -mass scaling relation for SPT-selected clusters are consistent with the Rykoff et al. (2012) values.

We repeat these analyses extending the sample to include those with  $4 < \xi < 4.5$  and find similar results (Table 3.2). The largest difference is in the redshift evolution term which now has a best fit value  $C_\lambda = 1.71^{+0.63}_{-0.57}$ . While formally this difference does not have large statistical significance ( $1.3\sigma$ ), it is coming from a sample that includes a large fraction of the same clusters, so it is likely statistically significant. A larger redshift evolution term would imply that higher redshift RM clusters are less massive at fixed  $\lambda$ . At the same time the derived scatter is also larger.

Two of the clusters in the  $4 < \xi < 4.5$  range are compatible with false associations. Excluding the two matched clusters with the highest probability of random associations results in a  $\sim 1\sigma$  shift in  $B_\lambda$  (from  $B_\lambda = 1.17$  to  $B_\lambda = 1.04$ ) and in a  $\sim 0.5\sigma$  shift in  $C_\lambda$  (from  $C_\lambda = 1.71$  to  $C_\lambda = 1.42$ ), while the other parameters ( $A_\lambda$  and  $D_\lambda$ ) are almost unchanged. Interestingly, even though we have increased the number of clusters in the SPT-SZ+RM sample by 40%, the constraints on the scaling relation parameters are only mildly tighter. There are two reasons for this. First these lower signal-to-noise SPT-SZ clusters have larger fractional mass uncertainties in  $\xi$  ( $\langle \xi \rangle^{-1} \sim 0.16$  and  $\langle \xi \rangle^{-1} \sim 0.13$  respectively for the  $\xi > 4$  and  $\xi > 4.5$  samples). Second, the richesses are also systematically lower, leading to a larger Poisson variance. Thus, each low  $\xi$  cluster has less constraining power than a high  $\xi$  cluster, reducing the impact of extending the sample to include the lower mass systems.

### 3.4.2 Consistency Test of Model

We also test the consistency of the adopted scaling relation model with the data by examining whether we are finding the expected number of matches with the correct distribution in richness. To do this, we focus on the SPT-E field, which at  $\sim 124.6 \text{ deg}^2$  is the largest contiguous region covered by the DES-SVA1 data. We carry out two different tests.

In the first test, we examine whether we are finding the expected number of SZE-selected clusters and whether these clusters have the expected number of optical matches with the correct  $\lambda$  distribution. We generate  $10^6$  Monte Carlo realizations of cluster samples extracted from the halo mass function above  $M_{500} >$

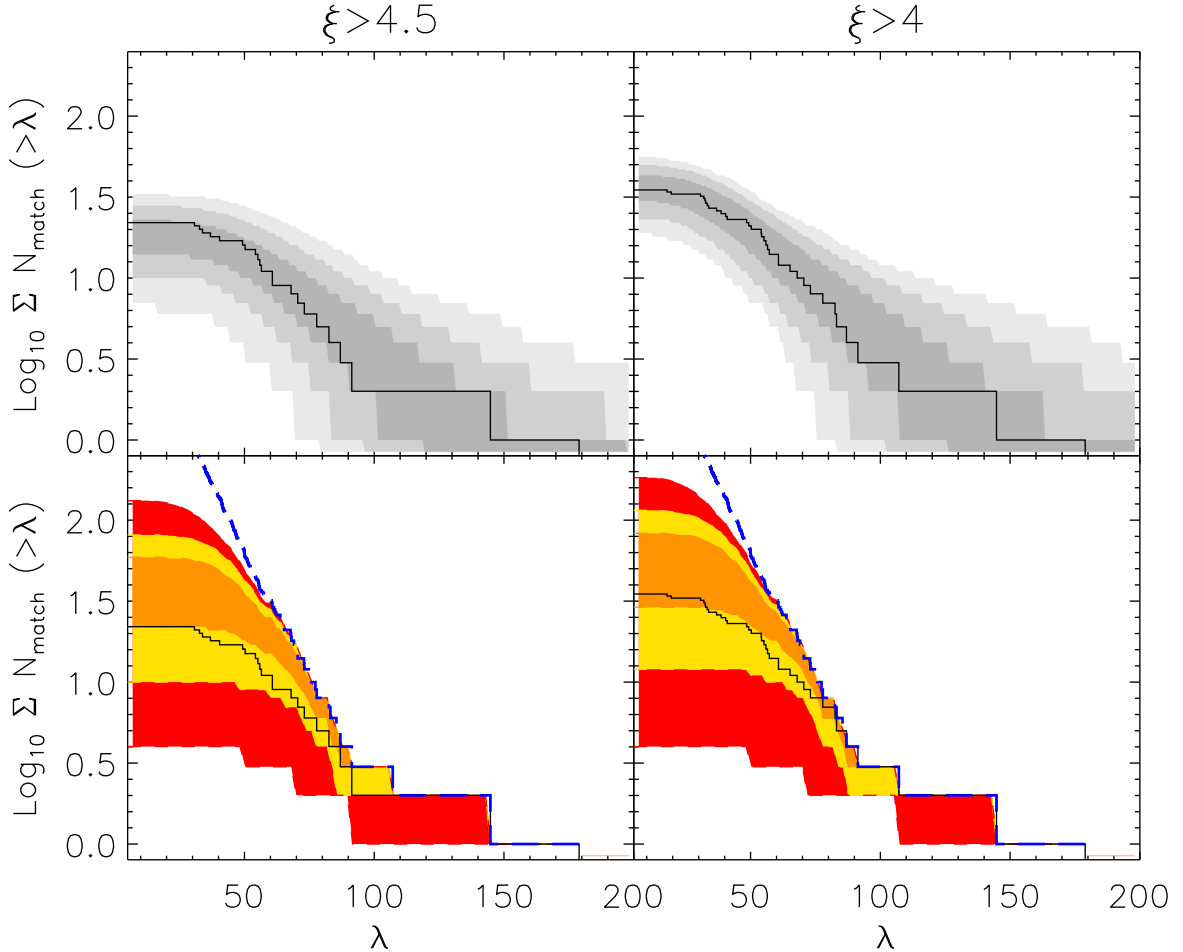


Figure 3.4 Consistency tests of our model (Section 3.3) and the SPT-SZ+RM catalog from the  $\sim 124 \text{ deg}^2$  SPT-E field. The solid black lines show the observed cumulative distribution in richness  $\lambda$  of the  $\xi > 4.5$  (left) and  $\xi > 4$  (right) SZE-selected samples. *Upper panels:* Gray scale regions show 1, 2, and  $3\sigma$  regions predicted by drawing  $10^6$  SZE-selected samples from the mass function and assigning  $\lambda$  according to our scaling relation constraints. There is good agreement with the data. *Lower panels:* Dashed blue lines show the cumulative distribution in  $\lambda$  of the full RM sample. Orange, yellow, and red areas define 1, 2, and  $3\sigma$  regions representing the predicted cumulative distribution of the SPT-SZ+RM catalog using as input (1) the full RM sample and (2) the probability (Eq. 3.10) that each RM cluster will have an SPT-SZ counterpart, given our scaling relation constraints. The data and the model exhibit a  $2\sigma$  tension at  $\lambda > 70$  where fewer than expected RM clusters (10 of 17) have SPT-SZ counterparts.

$10^{13.5} h_{70}^{-1} M_\odot$  and assign richnesses  $\lambda$  and SPT-SZ significance  $\xi$  using the parameters we extract from our analysis of the real matched catalog. These Monte Carlo mocks are generated taking into account the survey area as a function of redshift sampled by RM in the SPT-E field. We then apply the SZE selection—either  $\xi > 4.5$  or  $\xi > 4$ —and measure the cumulative distribution in  $\lambda$  of the SZE-selected samples. We then compare this to the same distribution in the real matched catalog.

Shaded regions in the upper panels of Figure 3.4 show 1, 2, and  $3\sigma$  confidence regions obtained from the mocks after marginalizing over the scaling relation parameters. The solid black line shows the distribution from the real catalog, which is in good agreement with the mocks. The largest observed difference is smaller than  $1\sigma$  indicating that the adopted model provides a consistent description of the observed number and richness distribution of the SZE-selected sample. Similarly, a Kolmogorov-Smirnov (KS) test for the observed cumulative distribution of matched systems as a function of  $\lambda$  and the corresponding median distribution from the Monte Carlo simulations, shows that the null hypothesis of data being drawn from same distributions cannot be excluded and returns  $p$ -values 0.76 and 0.96 for  $\xi > 4.5$  and  $\xi > 4$ , respectively.

The second test is focused on whether the RM cluster catalog (which is significantly larger than the SPT-SZ catalog) has the expected number of SZE matches with the correct  $\lambda$  distribution. Essentially, we take the observed RM catalog as a starting point, and calculate the expected number of systems with SPT-SZ counterparts given the model and parameter constraints from our  $\lambda$ -mass likelihood analysis. This test differs from the first in that it takes the *observed* RM selected cluster sample as a starting point, and such a test should be more sensitive to, for example, contamination in the RM catalog.

We proceed by first computing, for each real RM selected cluster in the SPT-E field, the probability  $P_m$  of that cluster also having  $\xi > 4.5$  and therefore being in the matched sample. We define this probability as:

$$\begin{aligned} P_m &= \int_{4.5}^{\infty} P(\xi|\lambda, z) d\xi \\ &= \int_{4.5}^{\infty} d\xi \int dM_{500} P(\xi|M_{500})P(M_{500}|\lambda, z), \end{aligned} \quad (3.10)$$

where  $P(M_{500}|\lambda, z) \propto P(\lambda|M_{500}, z)P(M_{500}, z)$  and  $P(M_{500}, z)$  is the halo mass function (Tinker et al. 2008).

To predict the expected number of RM clusters with SZE counterparts, we then randomly sample the scaling relation parameters, determining  $P_m$  for all the RM clusters in each case and using those probabilities to produce randomly sampled matched cluster catalogs. We use the results from the ensemble of random matched catalogs to produce a distribution of the expected cumulative distributions in  $\lambda$ . Orange, yellow, and red regions in the bottom panels of in Figure 3.4 show the 1, 2, and  $3\sigma$  confidence regions, respectively, of the expected cumulative distribution in  $\lambda$  for  $\xi > 4.5$  (left) and  $\xi > 4$  (right), given the RM catalog and scaling relation parameter constraints as input. The dashed blue line shows the cumulative distribution of the entire sample of RM clusters in the area, while the solid black line shows the observed cumulative distribution of the real matched catalog.

We note that the predicted number of SPT-SZ+RM matches in this case tends to be higher than that observed for  $\lambda > 35$ , but the tension is weak. Of some concern is the high  $\lambda$  end of the sample ( $\lambda > 70$ ), where only 10 of the 17 RM selected clusters have SPT-SZ counterparts at  $\xi > 4.5$  despite their having large probabilities indicating they should be in the SZE-selected sample. However, the mean expected number of matches at  $\lambda > 70$  is 13.4, providing again no significant tension between the model and the data. A KS test for the observed cumulative distribution of matched systems as a function of  $\lambda$  and the corresponding median distribution from the mocks shows that the null hypothesis of data being drawn from the same parent distribution cannot be excluded and returns  $p$ -values 0.90 and 0.33, respectively, for  $\xi > 4.5$  and  $\xi > 4$ .

The observed cumulative distribution is in tension with expectations at the  $2\sigma$  level, providing some indication of tension between the observed sample and our model. This tendency to observe fewer matches than expected given the size of the RM selected sample could be explained by either contamination within the RM sample, additional incompleteness within the SPT-SZ sample beyond that caused by scatter in the SZE-mass relation, or simply a statistical fluctuation. Future work exploring the SZE properties of the lower mass systems

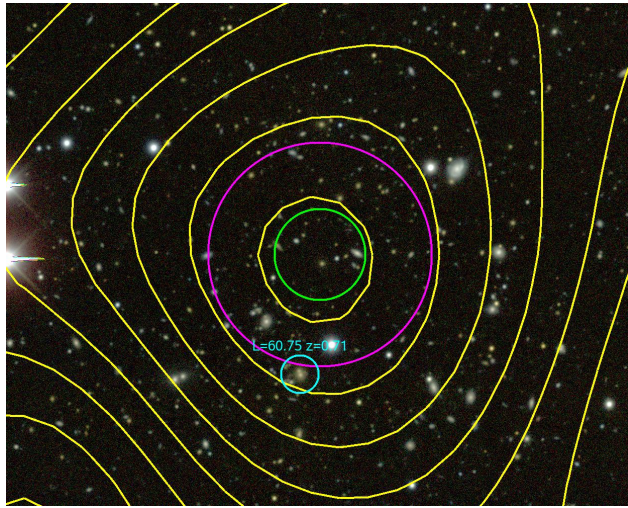


Figure 3.5 SPT-CL J0433-5630: DES-SVA1 *gri* pseudo colour image overplotted with SPT-SZ signal-to-noise contours (in steps  $\Delta\xi=1$ ). The magenta circle shows the projected  $R_{500}/2$  radius at  $z = 0.69$ , while the green circle describes the  $1\sigma$  SPT positional uncertainty (Eq.3.11). The cyan label marks the associated  $\lambda \sim 60$  RM cluster.

along with an extension of the current analysis to the full overlap between DES and the SPT-SZ survey will sharpen this test.

### 3.4.3 Optical-SZE Positional Offset Distribution

It has been shown that the miscentering in the optical can have a significant impact on the derived SZE signature for an optically-selected sample (Biesiadzinski et al. 2012; Sehgal et al. 2013; Rozo & Rykoff 2014; Rozo et al. 2014a,b). We note, however, that in our case the SZE signal has been estimated at the SZE-determined position, so our results are not affected by optical miscentering. In fact, we can now use our data to constrain the distribution of offsets between the SZE-determined and the optically-determined cluster centers.

As an example, we show in Figure 3.5 the DES-SVA1 *gri* pseudo colour image of SPT-CL J0433-5630, an SPT-SZ selected cluster with  $\xi \sim 5.3$  at redshift  $z = 0.69$  (B15). Yellow contours show the SPT-SZ signal-to-noise in steps of  $\Delta\xi = 1$ , while the magenta circle describes the projected radius  $R_{500}/2$ . The cyan label refers to the associated RM cluster centre. This RM cluster has richness  $\lambda \sim 60$ . We note that the most probable central galaxy selected by RM is significantly offset from the SZE defined centre. As a result, the measured SZE signature at the optical position ( $\xi = 4.1$ ) would be significantly underestimated with respect to the derived unbiased quantity  $\zeta = 5$  obtained through Eq. 3. We stress that this effect is not important for the scaling relation results reported in Section 3.4.1, as the sample analyzed here is SZE-selected.

Figure 3.6 contains a normalized histogram of the distribution of cluster positional offsets in units of  $R_{500}$  for the  $\xi > 4.5$  analyzed SPT-SZ sample. Under the assumption that the measurement uncertainty from the optical side is negligible, we model this distribution as an underlying intrinsic positional offset distribution convolved with the SPT-SZ positional uncertainty.

The  $1\sigma$  SPT-SZ positional uncertainty for a cluster with a pressure profile given by a spherical  $\beta$  model with  $\beta = 1$  and core radius  $\theta_c$ , detected with SPT-SZ significance  $\xi$  is described by:

$$\Delta\theta = \xi^{-1} \sqrt{\theta_{\text{beam}}^2 + \theta_c^2}, \quad (3.11)$$

where  $\theta_{\text{beam}} = 1.19$  arcmin is the beam FWHM (see Story et al. 2011 and Song et al. 2012b for more details).

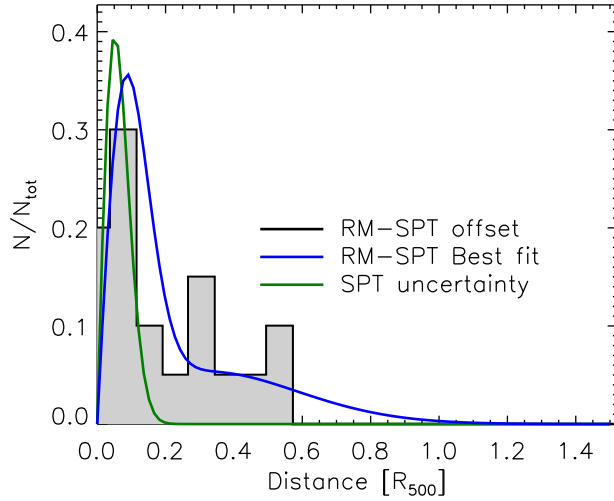


Figure 3.6 Solid histogram shows the measured fraction of clusters as a function of the SPT-SZ+RM optical-SZE positional offset in units of  $R_{500}$ . The green curve shows the SPT-SZ positional uncertainty, and the blue curves shows the best fitting SZE-optical positional offset model.

Table 3.3 Best fitting parameters and 68% confidence level of the optical-SZE positional offset distribution.

Catalog	$\rho_0$	$\sigma_0[R_{500}]$	$\sigma_1[R_{500}]$
RM- $\xi > 4.5$	$0.63^{+0.15}_{-0.25}$	$0.07^{+0.03}_{-0.02}$	$0.25^{+0.07}_{-0.06}$

As a result, the expected distribution of positional offsets in the case in which the intrinsic one is a  $\delta$ -function is shown (arbitrarily rescaled) as a green line.

Song et al. (2012b) have shown that the intrinsic optical-SZE positional offset distribution for an SPT-SZ selected sample is consistent with the optical-X-ray positional offset distribution of X-ray selected clusters (Lin et al. 2004). In both of these studies, the optical position was taken to be the brightest cluster galaxy (BCG) position. The offset distribution can be characterized by a large population of central galaxies with small offsets from the SZE centers and a less populated tail of central galaxies with large offsets (e.g. Lin et al. 2004; Rozo & Rykoff 2014; Lauer et al. 2014). We therefore parametrize the distribution of positional offsets between the RM centre and the SZE centre for  $x$  as:

$$P(x) = 2\pi x \left( \frac{\rho_0}{2\pi\sigma_0^2} e^{-\frac{x^2}{2\sigma_0^2}} + \frac{1-\rho_0}{2\pi\sigma_1^2} e^{-\frac{x^2}{2\sigma_1^2}} \right) \quad (3.12)$$

where  $x = r/R_{500}$ . While this model for the distribution was motivated by the expected intrinsic positional offset distribution, the measured distribution will include both the actual physical SZE-central galaxy offset distribution and the systematics due to failures in identifying the correct cluster center with the RM algorithm. For every cluster and parameter  $\rho_0 \in [0, 1]$ ,  $\sigma_0 \in [0, 1]$ , and  $\sigma_1 \in [\sigma_0, 1]$ , we then compare the predicted offset distribution obtained by convolving the model with the SPT-SZ positional uncertainty of Eq. 3.11 to extract the associated likelihood. Best fit parameters and 68% confidence intervals are shown in Table 3.3 and joint and fully marginalized parameter constraints are shown in Figure 3.7.

We note that the positional offset distribution for the RM sample is consistent with a concentrated dominant population ( $\rho_0 = 0.63^{+0.15}_{-0.25}$ ) of smaller offsets ( $\sigma_0 = 0.07^{+0.03}_{-0.02} R_{500}$ ) and a sub-dominant population characterized by larger offsets ( $\sigma_1 = 0.25^{+0.07}_{-0.06} R_{500}$ ), in good agreement with the observed fraction (33%) of

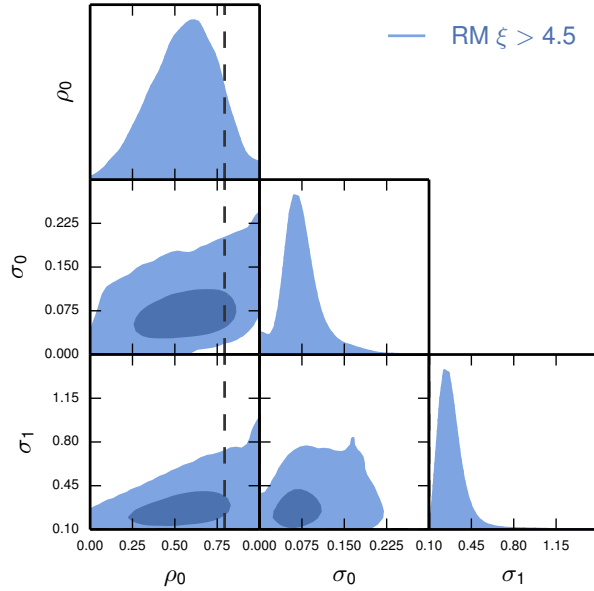


Figure 3.7 Posterior distribution for the 1 and  $2\sigma$  level of the three parameter model describing the positional offset distribution of Equation 3.12. Best fitting parameters are shown in Table 3.3. The RM predicted value of  $\rho_0$  for the adopted sample is shown as a dashed black line.

morphologically disturbed clusters in the X-ray at  $z = 0.6$  (Nurgaliev et al. 2013), which lends support to the hypothesis that the large positional offsets are due to merger activity. For the analyzed sample, the RM code (Rykoff et al. 2012, 2014) adopts the normalization of the centrally peaked distribution to be 0.79 (dashed black line in Figure 3.7), in good agreement with the value obtained here.

### 3.5 Conclusions

In this paper, we cross-match SZE-selected cluster candidates with  $\xi > 4.5$  from the  $2365 \text{ deg}^2$  SPT-SZ survey (B15) with the optically-selected cluster catalog extracted from the DES science verification data DES-SVA1. The optically-selected catalog is created using the RM cluster-finding algorithm. We study the robustness of our matching algorithm by applying it to randomly generated RM catalogs.

Using the adopted matching algorithm in the  $129.1 \text{ deg}^2$  of overlap between the two data sets, we create a matched catalog of 33 clusters. Eight of these clusters are removed as likely chance superpositions that are identified using the randomly generated catalogs. The resulting 25 cluster sample includes all previously known  $z < 0.8$  and  $\xi > 4.5$  SPT-SZ clusters in this area (Song et al. 2012b; Reichardt et al. 2013, B15) in addition to three previously unconfirmed SPT-SZ clusters.

We then study three characteristics of this cross-matched SPT-SZ+RM cluster sample:

1) *The richness mass relation of SPT-SZ selected clusters.* We calibrate the  $\lambda$ -mass relation from SZE measurements by applying the method described in Bocquet et al. (2015b)). In this analysis we assume a fixed fiducial cosmology and marginalize over the simultaneously calibrated SPT-SZ  $\xi$ -mass relation. We adopt flat priors on the richness–mass relation parameters. We find that the RM  $\lambda$ -mass relation for SPT-SZ selected clusters is characterized by a small asymptotic intrinsic scatter  $D = 0.15^{+0.10}_{-0.07}$  and by a slope  $B = 1.14^{+0.21}_{-0.18}$  that is consistent with unity. Our constraints are in good agreement with those of Rykoff et al. (2012) and show that

the scatter in mass at fixed richness at  $\lambda = 70$  for this sample is only 25% larger than the scatter in mass at fixed SPT-SZ observable  $\xi$ .

2) *Consistency test of model and matched catalog.* We carry out two consistency tests to determine whether there is tension between the observed matched sample and the expectations given the scaling relation model we have adopted. Both tests involve creating Monte Carlo generated cluster catalogs with associated richness and SPT-SZ significance derived from the fitted scaling relations. The first test checks whether the correct number of SZE-selected clusters is found and whether those clusters exhibit the correct number of optical matches with the expected  $\lambda$  distribution. As is clear from Figure 3.4, the observations are perfectly consistent with the expectations from the model. In the second test we take the much larger *observed* RM catalog as a starting point and use the model to test whether the expected number of SZE matches with the expected  $\lambda$  distribution is found. Unlike the first test, this one would in principle be sensitive to contamination within the RM sample. Here the agreement is not as good because there is a tendency for there to be fewer observed matches than expected. However, the tension reaches the  $2\sigma$  level at worst, and so there is no convincing evidence that our observed sample is inconsistent with the model. Thus, our analysis shows that the data in our matched SPT-SZ+RM sample are well described by our adopted model.

3) *The SZE-optical positional offset distribution.* We identify optical positional biases associated with 12% of the sample due to the masking in the DES-SVA1 data. We study the optical-SZE positional offset distribution for the matched sample. We model the underlying positional offset distribution as the sum of two Gaussians, while accounting for the SPT-SZ positional uncertainty. We show that the resulting distribution is consistent with being described by a dominant ( $63_{-25}^{+15}\%$ ) centrally peaked distribution with  $(\sigma_0 = 0.07_{-0.02}^{+0.03} R_{500})$  and a sub-dominant ( $\sim 37\%$ ) population characterized by larger separations  $(\sigma_1 = 0.25_{-0.06}^{+0.07} R_{500})$ . For the same population, the RM algorithm assumes that 79% of the clusters will belong to a small-offset population, consistent with our observations.

We also match the SPT-SZ cluster candidates with  $4 < \xi < 4.5$  to the RM optical cluster catalogs from DES-SVA1 to extend the mass range of the SZE-selected clusters. Including the SPT-SZ candidates between  $\xi = 4$  and  $\xi = 4.5$  increases the sample of matched clusters by  $\sim 40\%$  compared to the  $\xi > 4.5$  sample, highlighting the potential synergies of SPT and DES in producing lower mass extensions of SZE-selected cluster samples. We show that this larger sample produces results that are broadly consistent with the  $\xi > 4.5$  results, but only marginally tighter. This is due to the fact that mass constraints from lower signal-to-noise SPT clusters are somewhat weaker on a per cluster basis compared to the higher  $\xi$  sample. Future work benefiting from the larger region of overlap between the DES and SPT surveys will improve our derived constraints and help to better characterize the optical and SZE properties of cluster samples in terms of positional offsets, purity, and completeness. Moreover, the multiwavelength datasets available through DES and SPT enable characterization of the galaxy populations of large SZE-selected cluster samples, calibration of the SZE-selected cluster masses using weak lensing constraints, and many other promising studies.

We acknowledge the support by the DFG Cluster of Excellence “Origin and Structure of the Universe”, the Transregio program TR33 “The Dark Universe” and the Ludwig-Maximilians University. The South Pole Telescope is supported by the National Science Foundation through grant PLR-1248097. Partial support is also provided by the NSF Physics Frontier Center grant PHY-1125897 to the Kavli Institute of Cosmological Physics at the University of Chicago, the Kavli Foundation and the Gordon and Betty Moore Foundation grant GBMF 947. A.A.S. acknowledges a Pell grant from the Smithsonian Institution. This work was partially completed at Fermilab, operated by Fermi Research Alliance, LLC under Contract No. De-AC02-07CH11359 with the United States Department of Energy.

### 3.6 Appendix: Study of mass-richness scatter for clusters found with the VT method

We have used the same framework to analyze a second DES-SVA1 cluster catalog created with the Voronoi Tessellation (VT) cluster finder (Soares-Santos et al. 2011). The VT method uses photometric redshifts to detect clusters in 2+1 dimensions, and is designed to produce a cluster catalog up to  $z \sim 1$  and down to  $M \sim 10^{13.5} M_{\odot}$  without any assumptions about the colours of galaxies in cluster environments. The motivation for its development in DES, in parallel to the development of RM, is the possibility of obtaining two cosmological measurements with different sensitivity to astrophysical systematics. VT has been tested on DES simulations (Soares-Santos et al. 2011) and on SDSS data. The mean mass-richness relation has been calibrated using a stacked weak lensing analysis of the SDSS VT clusters (Wiesner et al. 2015). In this section we describe the first study of the scatter of the mass-richness relation using our analysis framework.

#### 3.6.1 VT method

To detect clusters with the VT method, we build 2D tessellations in each photometric redshift shell and flag galaxies that lie in high-density cells as cluster members. The density threshold is set in a non-parametric way from the 2-point correlation function of that given shell. This takes advantage of the fact that the distribution of VT cell densities can be uniquely predicted for any given point process. The 2-point function is a good description of the point process of the background galaxies on the sky. Clusters cause a small deviation from the predicted distribution, and we take the point where that deviation is maximized as the threshold for detection.

#### 3.6.2 VT catalog for DES SVA1 data

For the DES SVA1 data, the final catalog consists of 12948 clusters with richness  $N_{vt} > 5$  and redshifts in the range  $0.15 < z < 1$ .  $N_{vt}$  is defined as the number of member galaxies. The catalog covers the SPT-E and SPT-W regions of the SVA1 total footprint. We use DESDM data products as inputs, namely the *Gold* galaxy catalog, plus photometric redshifts and mask information. We used a mask to apply magnitude cuts  $10 < \text{mag\_auto\_i} < 23.5$ . The photometric redshift information was obtained using a neural network method (Sánchez et al. 2014).

We match the VT and SPT-SZ catalogs using the same method as described in Section 2.3. We sort the SPT-SZ cluster sample according to decreasing SPT observable  $\xi$  and sort the VT catalogs according to decreasing richness. Then we associate the SPT cluster candidate with the richest cluster candidate whose centre lies within  $1.5 R_{500}$  of the SPT-SZ centre. We finally remove the associated optical cluster from the list of possible counterparts when matching the remaining SPT-selected clusters. This procedure results in 42 VT clusters matched to  $\xi > 4.5$  SPT-SZ clusters.

#### 3.6.3 Results

In Figure 3.8 we show the optical richness  $N_{vt}$  as a function of  $\xi$  (left panel) for the 42 matched clusters. The scatter in the richness- $\xi$  plot indicates that the VT richness performs poorly as a mass indicator. Improvements to the method are being developed based on these findings. Specifically, future work will explore using the galaxy magnitudes to calculate total stellar masses, which can then be used as a mass proxy.

Figure 3.8 also shows the VT estimated redshifts versus the redshifts determined in SPT follow-up observations (right panel). There is good agreement for  $z > 0.35$ . Deviations at lower  $z$  are found to arise from problems in the calculation of the 2-point function predictions at  $z < 0.35$ , and a fix is underway.

We also obtained the best fit parameters, and the corresponding 68% c.l. uncertainties, for the richness-mass

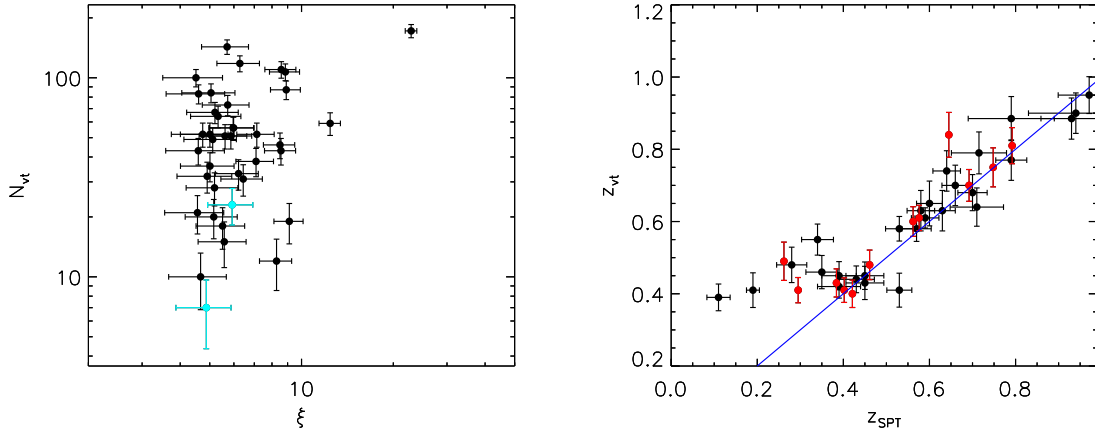


Figure 3.8 *Left panel*: Richness as a function of the SPT-SZ significance  $\xi$  for the SPT-SZ+VT cluster sample. Clusters at  $z < 0.25$  are not used for the richness-mass fit and are shown in cyan. *Right panel*: The estimated redshift for the VT sample as a function of SPT-SZ redshifts as presented in B15. SPT-SZ candidates with spectroscopic redshift are shown in red.

scaling relation described by Equations 3.7 and 3.8:

$$\begin{aligned} A_{VT} &= 48.1^{+6.9}_{-6.3}, & B_{VT} &= 0.56^{+0.51}_{-0.25}, \\ C_{VT} &= -0.51^{+1.82}_{-1.48}, & D_{VT} &= 0.64^{+0.29}_{-0.14}. \end{aligned} \quad (3.13)$$

This result is consistent with the calibration for the mean relation obtained with weak lensing (Wiesner et al. 2015). The uncertainties, however, are larger than those obtained for RM. We expect that improvements to the richness estimator will result in better performance in future applications of the VT method. VT is not a mature cluster finder method as RM but the complementarity of the two techniques argues for further development of this alternative. This study allowed us to identify a key area for improvement and establishes a framework for future assessment of the mass-richness scatter for VT clusters.



## Chapter 4

# The Growth of Cosmic Structure Measured with Galaxy Clusters in the South Pole Telescope SPT-SZ Survey

S. Bocquet and the South Pole Telescope collaboration, in preparation  
to be submitted to *The Astrophysical Journal Letters (ApJL)*

### ABSTRACT

We measure the growth rate of structure as parametrized with the growth index  $\gamma$  using galaxy clusters from the 2500 deg<sup>2</sup> SPT-SZ survey. We uniformly select a sample of 377 cluster candidates with Sunyaev-Zel'dovich effect (SZE) detection significance  $\xi > 5$  and redshift  $z > 0.25$ . Of these, 82 also have deep *Chandra* X-ray data that is used for calibrating the mass-observable relation adopting a normalization that is based on weak lensing. We assume a flat  $\Lambda$ CDM background cosmology with the additional degree of freedom  $\gamma$  describing the growth rate. Using our cluster data set with  $H_0$  and BBN priors we constrain  $\gamma = 0.44 \pm 0.13$ , in agreement with the prediction by General Relativity of  $\gamma_{\text{GR}} = 0.55$ . This is the most precise measurement from clusters to date, and it is limited by the uncertainty on the redshift evolution of the SZE mass-observable scaling relation. Additionally allowing for the dark energy equation of state parameter  $w$  to vary, we simultaneously constrain the growth and expansion histories of the Universe. We find  $\gamma = 0.53 \pm 0.15$  and  $w = -1.30 \pm 0.30$ , in agreement with the  $\Lambda$ CDM model. The combination of these constraints with cosmic microwave background anisotropy constraints will enable even more precise constraints.

**Key words:** cosmic background radiation — cosmology: observations — galaxies: clusters: individual — large-scale structure of universe

## 4.1 Introduction

Measurements of the abundance of galaxy clusters are a unique cosmological tool because their formation is affected both by the geometry of the Universe and the rate at which the large-scale structure grows. Their sensitivity to growth makes cluster analyses particularly complementary to constraints from geometry-based probes such as measurements of the anisotropies in the cosmic microwave background (CMB) radiation and distance measurements using type Ia supernovae (SNIa) or baryon acoustic oscillations (BAO) (e.g., Vikhlinin et al. 2009b; Mantz et al. 2010a; Rozo et al. 2010; Benson et al. 2013; Hasselfield et al. 2013; Reichardt et al. 2013; Planck Collaboration et al. 2014c; Bocquet et al. 2015b; Planck Collaboration et al. 2015b).

One of the biggest challenges in cosmology is to understand and characterize the accelerated expansion that started when dark energy became the dominant component in the late Universe at  $z < 1$ . Various models of dark energy that differ from a simple cosmological constant  $\Lambda$  are proposed and tested. None of these tests that really probe the geometry of the Universe have provided evidence that dark energy cannot accurately be described by a cosmological constant  $\Lambda$ . Another approach to tackle this question is to consider deviations from General Relativity (GR) on large scales, as this could potentially mimic an accelerating expansion. One particular aspect within this approach is to measure the growth rate of structure. Note that different modified gravity models predict different growth rates, and so it is convenient to constrain a parametric, phenomenological growth model, which can then be compared to theoretical predictions. In an identical fashion, the parametrized model can be used to challenge the standard  $\Lambda$ CDM model.

Such an approach has been applied using X-ray selected cluster samples (Rapetti et al. 2010, 2013; Mantz et al. 2015). However, to challenge the dark energy paradigm and the standard model of structure growth, one does ideally want to probe the cosmic evolution over a larger redshift range. A cluster sample selected by the Sunyaev-Zel'dovich effect (SZE, Sunyaev & Zel'dovich 1972) in high-resolution mm-wave data is ideally suited as clusters are detected in a nearly redshift-independent way up to the highest redshifts at which clusters exist. The SZE arises when CMB photons passing through the hot intra-cluster medium of a massive galaxy cluster scatter off thermal electrons, introducing a characteristic spectral distortion.

The South Pole Telescope (SPT, Carlstrom et al. 2011) collaboration has previously presented constraints on the growth rate of structure using an SZE-selected cluster sample (Bocquet et al. 2015b). However, this study was restricted to data from the first  $720 \text{ deg}^2$  of survey data, and the constraints obtained from clusters were weak. By now, the cluster data from the full  $2500 \text{ deg}^2$  survey have been published (Bleem et al. 2015), and the cosmology sample contains 377 cluster candidates. Of these, 82 also have high-quality X-ray data, which can be used for calibrating the SZE mass-observable scaling relation. The collaboration is currently preparing a cluster cosmology analysis of that combined sample (de Haan et al., in prep., hereafter dH15). In the present work, we use this same data and focus on cosmological questions related to structure growth. This paper is organized as follows. In Section 4.2, we present the cosmological model and the parametrization of growth that we consider. A brief overview over the SPT-SZ data and the analysis method appears in Section 4.3. We present and discuss our results in Section 4.4. We conclude with a summary in Section 4.5.

## 4.2 Cosmological Model and Parametrized Growth

The assumed base-line model is the spatially flat  $\Lambda$ CDM model with a single massive neutrino of mass  $m_\nu = 0.06 \text{ eV}$ . We extend this model through a purely phenomenological parametrization of structure growth. Note that this particular parametrization does not have any profound theoretical motivation; it can, however, be used as a consistency test to challenge the standard cosmological model. Following e.g., Peebles (1980); Wang & Steinhardt (1998), we parametrize the growth rate

$$f(a) \equiv \frac{d \ln \delta}{d \ln a} \equiv \Omega_m(a)^\gamma, \quad (4.1)$$

where  $\delta$  is the density contrast,  $a$  the scale factor, and  $\Omega_m$  the matter density parameter. The parameter  $\gamma$  is the growth index, governing the growth evolution. Since we are interested in possible departures from the standard model at late times, when dark energy is not negligible, we assume the standard evolution of the Universe up until a redshift  $z_{\text{ini}} = 10$ . At later times, the growth factor  $D$  evolves as

$$D_{\text{ini}}(z) \equiv \frac{\delta(z)}{\delta(z_{\text{ini}})} = \delta(z_{\text{ini}})^{-1} \exp\left(\int_{z_{\text{ini}}}^z d\ln a \Omega_m(a)^\gamma\right). \quad (4.2)$$

Note that this definition implies that the growth factor is independent of wavenumber  $k$ . The matter power spectrum at redshift  $z < z_{\text{ini}}$  can now be expressed as the product of the  $\Lambda$ CDM power spectrum  $P(k, z_{\text{ini}})$  with the growth factor at late times:

$$P(k, z) = P(k, z_{\text{ini}}) D_{\text{ini}}^2(z). \quad (4.3)$$

GR predicts a growth index  $\gamma_{\text{GR}} \simeq 0.55$ . Letting  $\gamma$  vary in a cosmological fit allows one to perform a consistency test of GR based on structure growth. In a second state, we will also allow for an extension of the dark energy sector by letting the dark energy equation of state parameter  $w$  vary.

## 4.3 Data and Analysis

### 4.3.1 Galaxy Cluster Data

We use a cluster sample selected via the SZE in the  $2500 \text{ deg}^2$  SPT-SZ survey data. Details of the survey and the cluster detection and confirmation can be found elsewhere (Bleem et al. 2015). Briefly, from 2008 to 2011 the SPT collaboration used the telescope to conduct a contiguous survey in the southern sky down to depths of approximately 40, 18, and 70  $\mu\text{K}$ -arcmin and with beam sizes of roughly  $1.6'$ ,  $1.1'$ , and  $1.0'$  in the 95, 150, and 220 GHz bands, respectively. Clusters are then extracted from the 95 and 150 GHz maps using a multi-scale matched filter (Melin et al. 2006). Differences between the observed field depths are accounted for by rescaling the amplitude of the mass-observable relation in Equation 4.5 (see Table 1 in dH15).

As in previous SPT analyses, the detection significance  $\xi$  is used as the SZE mass proxy (Vanderlinde et al. 2010; Benson et al. 2013; Reichardt et al. 2013; Bocquet et al. 2015b). It has a Gaussian measurement error of unit width and it is related to the unbiased SZE significance  $\zeta$  by

$$\zeta = \sqrt{\langle \xi \rangle^2 - 3}. \quad (4.4)$$

The SZE mass-observable relation is assumed to follow a log-normal distribution with mean

$$\zeta = A_{\text{SZ}} \left( \frac{M_{500}}{3 \times 10^{14} h^{-1} M_\odot} \right)^{B_{\text{SZ}}} \left( \frac{E(z)}{E(0.6)} \right)^{C_{\text{SZ}}} \quad (4.5)$$

and scatter  $D_{\text{SZ}}$ . The parameters of this scaling relation are simultaneously fitted for while conducting the cosmological analysis. We follow previous SPT cluster analyses and apply Gaussian priors, although with updated values from the hydrodynamic cosmo-OWLS simulations  $A_{\text{SZ}} = 5.38 \pm 1.61$ ,  $B_{\text{SZ}} = 1.340 \pm 0.268$ ,  $C_{\text{SZ}} = 0.49 \pm 0.49$ , and  $D_{\text{SZ}} = 0.13 \pm 0.13$  (Le Brun et al. 2014).

The cosmology sample is selected with thresholds  $\xi > 5$  and  $z > 0.25$ , and contains 377 cluster candidates. Of these, 82 confirmed clusters have high-quality X-ray follow-up data from *Chandra* with typically 2000 source photons. These data were part of a *Chandra* X-ray Visionary Project project (PI:Benson) and were initially presented and analyzed in McDonald et al. (2013). For this work, we focus on the low-scatter mass proxy  $Y_X \equiv M_g T_X$  which is the product of the gas mass  $M_g$  with the X-ray temperature  $T_X$ . The X-ray mass-observable relation is

$$\frac{M_{500}}{10^{14} M_\odot} = A_X h^{1/2} \left( \frac{h}{0.72} \right)^{\frac{5}{2} B_X - \frac{3}{2}} \left( \frac{Y_X}{3 \times 10^{14} M_\odot \text{ keV}} \right)^{B_X} E(z)^{C_X}, \quad (4.6)$$

with lognormal scatter  $D_X$ . As in previous SPT analyses, we apply Gaussian priors on  $B_X = 0.57 \pm 0.03$ ,  $C_X = -0.4 \pm 0.2$ , and  $D_X = 0.12 \pm 0.08$ . Accounting for recent calibration of the  $Y_X$ -mass relation (Hoekstra et al. 2015), we follow dH15 and update the normalization to  $A_X = 7.27 \pm 1.02$ .

Throughout the following, we will refer to the SPT-SZ clusters with their follow-up data as the SPT<sub>CL</sub> dataset.

### 4.3.2 Cluster Abundance and Likelihood Function

The expected number density of clusters is computed from the matter power spectrum (Equation 4.3) through the halo mass function (HMF). In practice, we use CAMB<sup>1</sup> (Lewis et al. 2000) to compute the matter power spectrum and apply the HMF presented in Tinker et al. (2008). To account for the impact of non-zero neutrino masses on the HMF, we only take the matter power spectrum for dark matter + baryons (no neutrinos) into account when calculating the cluster abundance<sup>2</sup> (Costanzi et al. 2013). As in previous SPT analyses, the likelihood function for the cluster abundance measurement is

$$\ln \mathcal{L} = - \int d\xi dz \frac{dN(\xi, z)}{d\xi dz} + \sum_i \frac{dN(\xi_i, Y_{X,i}, z_i)}{d\xi dY_X dz} \quad (4.7)$$

up to a constant, and where the sum runs over all clusters  $i$  in the sample. The first term is independent of  $Y_X$  because the sample was selected according to  $\xi$  and  $z$  only. In practice, we evaluate the likelihood using the method developed and presented in Bocquet et al. (2015b), except that we additionally allow for correlated scatter between  $\zeta$  and  $Y_X$ . The correlation coefficient  $\rho_{\text{SZ-X}}$  is allowed to vary uniformly in the range  $[-1, 1]$ .

### 4.3.3 External Cosmological Datasets and Priors and the Likelihood Sampling Algorithm

In addition to our cluster data we also use external cosmological probes. We use a prior on the Hubble constant  $H_0 = 73.8 \pm 2.4 \text{ km s}^{-1} \text{ Mpc}^{-1}$  (Riess et al. 2011). We use measurements of the CMB anisotropy using *Planck* data from the 2013 release combined with WMAP9 polarization anisotropy data (Hinshaw et al. 2013; Planck Collaboration et al. 2014a,b).

Cluster data alone are not sensitive to every cosmological parameter. Therefore, when not including CMB anisotropy data, we fix the reionization optical depth to  $\tau$  and the scalar spectral index  $n_s$  to the CMB-preferred values (Planck Collaboration et al. 2015a). We also apply a Gaussian prior on the baryon density  $\Omega_b h^2 = 0.022 \pm 0.002$  from big-bang nucleosynthesis (BBN, Kirkman et al. 2003).

The parameter fits are performed using the affine invariant Markov chain Monte Carlo ensemble sampler emcee<sup>3</sup> (Foreman-Mackey et al. 2013). Apart from possible personal preferences for Python, the main benefit of emcee is that it can be run in parallel on hundreds of CPU cores. Given that a typical call of the likelihood function takes or order 10 sec, the parallel execution of this step is highly appreciable. In addition to extensive self-consistent tests of the analysis pipeline used in this work we also confirmed that we recover results that are compatible with the ones presented in dH15.

## 4.4 Results and Discussion

We discuss the results we obtain from the SPT<sub>CL</sub>+BBN+ $H_0$  data combination for the  $\Lambda$ CDM model with parametrized growth of structure ( $\gamma+\Lambda$ CDM) and for the same model but additionally allowing for the dark energy equation of state parameter to vary ( $\gamma+w$ CDM). The marginalized parameter constraints on the relevant

<sup>1</sup><http://camb.info/>

<sup>2</sup>The variance in the matter field  $\sigma_8$  is calculated in the usual way from the power spectrum for dark matter + baryons + neutrinos.

<sup>3</sup><http://dan.iel.fm/emcee/current/>

Table 4.1 Marginalized results from  $SPT_{CL} + H_0 + BBN$ . The constraint on the growth index  $\gamma$  only mildly degrades when  $w$  is allowed as an additional free parameter.

Parameter	$\Lambda\text{CDM}$	$\gamma+\Lambda\text{CDM}$	$w\text{CDM}$	$\gamma+w\text{CDM}$
$\Omega_m$	$0.291 \pm 0.039$	$0.293 \pm 0.036$	$0.271 \pm 0.041$	$0.257 \pm 0.046$
$\sigma_8$	$0.779 \pm 0.036$	$0.819 \pm 0.043$	$0.792 \pm 0.032$	$0.808 \pm 0.046$
$w$	(-1)	(-1)	$-1.19 \pm 0.24$	$-1.30 \pm 0.30$
$\gamma$	(0.55)	$0.44 \pm 0.13$	(0.55)	$0.53 \pm 0.15$

parameters are summarized in Table 4.1 where we also show the constraints on the base-line  $\Lambda\text{CDM}$  and  $w\text{CDM}$  models for reference. For a detailed discussion of these  $\Lambda\text{CDM}$  constraints, and of constraints on dark energy and neutrino masses we refer the reader to dH15.

#### 4.4.1 $\gamma+\Lambda\text{CDM}$

We consider a first extension of the standard  $\Lambda\text{CDM}$  model by adding the growth index  $\gamma$  as another free parameter. We measure

$$\gamma = 0.44 \pm 0.13, \quad (4.8)$$

in agreement with the GR value  $\gamma_{GR} = 0.55$ .

In our initial analysis on structure growth using the first 720 deg<sup>2</sup> of SPT-SZ survey data,  $\gamma$  was not constrained from cluster data alone (Bocquet et al. 2015b). Together with CMB anisotropy data, we obtained a constraint that was about twice as broad as the one presented above. Using a sample of 224 X-ray selected clusters and weak gravitational lensing follow-up of 50 of these, the Weighing the Giants (WtG) team constrained  $\gamma$  with an uncertainty of  $\sigma(\gamma_{WtG}) = 0.19$  (Mantz et al. 2015). Our measurement is significantly tighter, which is largely due to the increased leverage on  $\gamma$  afforded by the broader redshift range of the SPT sample. While the WtG sample is restricted to low redshifts  $0 < z < 0.5$ , our SZE-selected sample spans a redshift range  $0.25 < z \lesssim 1.5$ . The measurement of the growth index is really a measurement of cosmic evolution and therefore a broad redshift range is favorable.

In Figure 4.1, we show the joint constraints on  $\gamma$  and the normalization of the power spectrum  $\sigma_8$  from our cluster sample  $SPT_{CL}$  and from *Planck*+WP (as shown in Mantz et al. 2015). The contours overlap at  $\sigma_8 \sim 0.8$  and  $\gamma \sim 0.55$ , but it is clear that clusters perform much better in this parameter space. The fact that the cluster degeneracy is only weak indicates that the cluster abundance at different redshifts is measured well enough to distinguish between evolution and changes in the overall amplitude. The most pronounced degeneracy between  $\gamma$  and parameters of the scaling relations is with  $C_{SZ}$ , the redshift evolution, where systematic uncertainty still limits the constraints on  $\gamma$ . Note that our constraints on the  $\gamma+\Lambda\text{CDM}$  model are not limited by the systematic uncertainty on the overall mass normalization  $A_{SZ}$ , as it is the case for  $\Lambda\text{CDM}$  (dH15).

#### 4.4.2 $\gamma+w\text{CDM}$

We go one step further and also allow the dark energy equation of state parameter  $w$  to vary. This test is particularly interesting because it allows one to differentiate between potential departures from  $\Lambda\text{CDM}$  both with respect to expansion and growth. Using the  $SPT_{CL}$  data we simultaneously constrain

$$\gamma = 0.53 \pm 0.15 \quad (4.9)$$

$$w = -1.30 \pm 0.30, \quad (4.10)$$

in agreement with the fiducial values  $\gamma_{GR} = 0.55$  and  $w_{\Lambda\text{CDM}} = -1$ . However, we note that the constraint on  $w$  is only consistent with a cosmological constant at the  $1\sigma$  level. The joint constraint on both parameters is shown

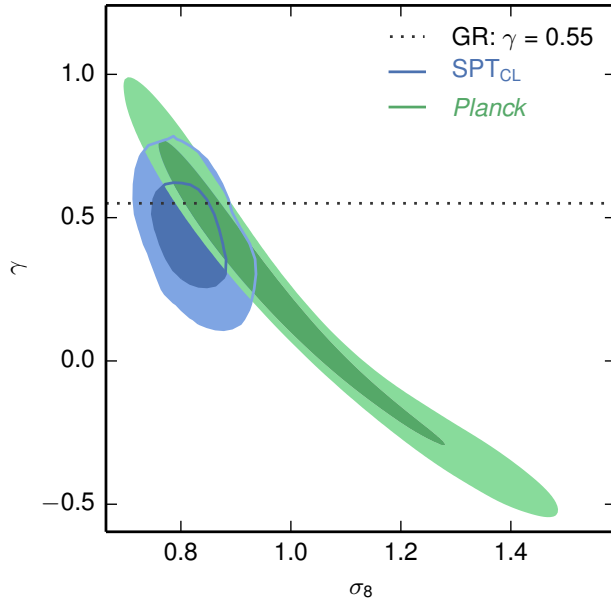


Figure 4.1 Likelihood contours (68% and 95%) in the  $\gamma$ - $\sigma_8$ -plane from clusters and CMB measurements. The dotted line indicates the growth rate predicted by GR, which is fully consistent with the data. Both datasets provide a consistent measurement of  $\gamma$ , but it is clear that clusters perform much better in this parameter plane.

in Figure 4.2, which provides no evidence for any parameter degeneracy. This means that our cluster data is allowing us to disentangle the impact of a change in expansion and in growth rate. Note that the constraints on other cosmological parameters in Table 4.1 do not significantly degrade after allowing for the additional freedom in the model.

## 4.5 Summary

We used the latest SPT-SZ cluster dataset to measure the growth rate of structure. To the SPT-SZ cluster sample of 377 candidates we add 82 X-ray  $Y_X$  measurements which serve as mass calibration data. The normalization of the  $Y_X$ -mass relation is calibrated against weak lensing measurements (Hoekstra et al. 2015); the other parameters of the scaling relation are deduced from numerical simulations. In our analysis method, we simultaneously fit for the parameters of the SZE-mass and  $Y_X$ -mass relations, for correlated scatter among both observables, and for cosmology. We use a highly parallelized likelihood sampler. Our analysis closely follows previous SPT work.

First, we assume a spatially flat  $\Lambda$ CDM background cosmology with the additional parameter  $\gamma$  describing structure growth. This additional degree of freedom hardly degrades the constraints on  $\Omega_m$  and  $\sigma_8$ , and we measure  $\gamma = 0.44 \pm 0.13$ . This value is lower than, but in agreement with the prediction of  $\gamma_{\text{GR}} = 0.55$ . We note that a smaller value for  $\gamma$  corresponds to faster growth. In Figure 4.1 we showed that measuring the cluster abundance outperforms measurements of CMB anisotropy for this particular cosmological model.

In a next step, we additionally allow the dark energy equation of state parameter  $w$  to vary and fit for a  $w$ CDM+ $\gamma$  cosmology. The constraints do not significantly degrade compared to the  $\Lambda$ CDM+ $\gamma$  case, and we can place constraints on both the growth and expansion histories of the Universe. Our measurements

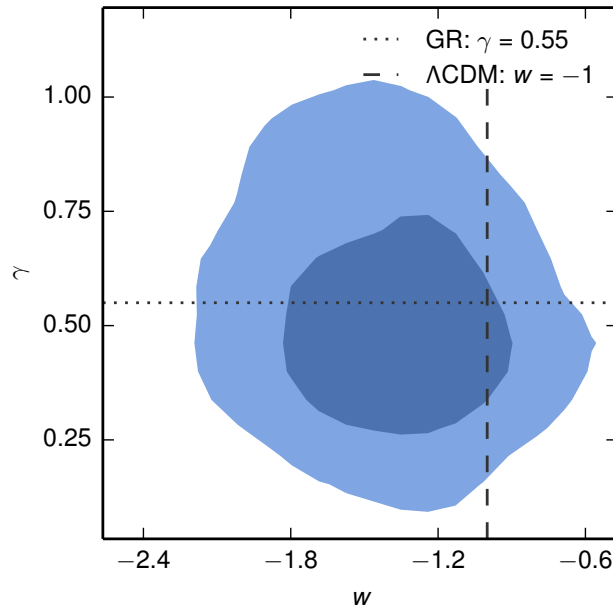


Figure 4.2 Likelihood contours (68% and 95%) in the  $\gamma$ - $w$ -plane. There is no evidence for departure from the standard growth and expansion histories as predicted by the  $\Lambda$ CDM model. For cluster data these two parameters exhibit no clear degeneracy.

$\gamma = 0.53 \pm 0.15$  and  $w = -1.30 \pm 0.30$  do not show evidence for tension with the  $\Lambda$ CDM model, although the recovered value of  $w$  is low by about  $1\sigma$ .

Our constraints on structure growth are tighter than those obtained by the Weighing the Giants team (Mantz et al. 2015). We explain this by the fact that the SPT-SZ sample probes a much broader redshift range out to redshift  $z \sim 1.5$ . Given that we are effectively probing the evolution of structure growth, it is expected that this enhanced leverage on redshift is reflected in tighter constraints. An interesting improvement upon the work presented here would be the inclusion of a low-redshift sample. With this, we could indeed cover the full range in redshift that is sensitive to possibly modified growth of structure as considered here.

We acknowledge the support of the DFG Cluster of Excellence “Origin and Structure of the Universe” and the Transregio program TR33 “The Dark Universe”. The calculations have partially been carried out on the computing facilities of the Computational Center for Particle and Astrophysics (C2PAP) at the Leibniz Supercomputer Center (LRZ). The South Pole Telescope is supported by the National Science Foundation through grant PLR-1248097. Partial support is also provided by the NSF Physics Frontier Center grant PHY-1125897 to the Kavli Institute of Cosmological Physics at the University of Chicago, the Kavli Foundation and the Gordon and Betty Moore Foundation grant GBMF 947.



# Calibration of the Cluster Mass Function

In the following, an analysis of numerical simulation data is presented. The aim is to calibrate the cluster mass function taking halo baryons into account and to discuss the cosmological implications of the recovered fit. The following study is shown as submitted to MNRAS (Bocquet et al. 2015a).



## Chapter 5

# Baryon impact on the halo mass function: Fitting formulae and implications for cluster cosmology

S. Bocquet, A. Saro, K. Dolag, and J. J. Mohr 2015  
submitted to *Monthly Notices of the Royal Astronomical Society*, ArXiv:1502.07357

### ABSTRACT

We calibrate the halo mass function accounting for halo baryons and present fitting formulae for spherical overdensity masses  $M_{500c}$ ,  $M_{200c}$ , and  $M_{200m}$ . We use the hydrodynamical *Magneticum* simulations, which are well suited because of their high resolution and large cosmological volumes of up to  $\sim 2 \text{ Gpc}^3$ . Baryonic effects globally decrease the masses of galaxy clusters, which, at given mass, results in a decrease of their number density. This effect vanishes at high redshift  $z \sim 2$  and for high masses  $\gtrsim 5 \times 10^{14} M_\odot$ . We perform cosmological analyses of three idealized approximations to the cluster surveys by the South Pole Telescope (SPT), *Planck*, and eROSITA. For the SPT-like and the *Planck*-like samples, we find that the impact of baryons on the cosmological results is negligible. In the eROSITA-like case, we find that neglecting the baryonic impact leads to an underestimate of  $\Omega_m$  by about 0.01, which is comparable to the expected uncertainty from eROSITA. We compare our mass function fits with the literature. In particular, in the analysis of our *Planck*-like sample, results obtained using our mass function are shifted by  $\Delta(\sigma_8) \simeq 0.05$  with respect to results obtained using the Tinker et al. (2008) fit. This shift represents a large fraction of the observed difference between the latest results from *Planck* clusters and CMB anisotropies, and the tension is essentially removed. We discuss biases that can be introduced through inadequate mass function parametrizations that introduce false cosmological sensitivity. Additional work to calibrate the halo mass function is therefore crucial for progress in cluster cosmology.

**Key words:** cosmology: theory – cosmological parameters – dark matter – large-scale structure of the Universe – methods: numerical; statistical – galaxy clusters: general

## 5.1 Introduction

Galaxy clusters are the largest collapsed objects in the Universe. Their distribution in mass and redshift is highly sensitive to key cosmological parameters such as the matter density  $\Omega_m$ , or the amount of matter fluctuations in the Universe  $\sigma_8$  (e.g. Henry & Arnaud 1991; White et al. 1993). Furthermore, they can be used to constrain models of dark energy, the cosmic growth rate, and the neutrino sector (Wang & Steinhardt 1998; Haiman et al. 2001). Catalogues from different cluster surveys have proven to be useful cosmological probes (e.g. Vikhlinin et al. 2009b; Mantz et al. 2010a; Rozo et al. 2010; Benson et al. 2013; Hasselfield et al. 2013; Planck Collaboration et al. 2014c; Bocquet et al. 2015b; Mantz et al. 2015).

The predicted abundance of galaxy clusters is linked to the linear matter power spectrum through the halo mass function, which was first estimated analytically (Press & Schechter 1974). Since then, numerical  $N$ -body simulations have been used to calibrate fitting functions (e.g. Jenkins et al. 2001; Sheth et al. 2001; White et al. 2002; Reed et al. 2003; Warren et al. 2006; Lukić et al. 2007; Reed et al. 2007; Tinker et al. 2008; Crocce et al. 2010; Bhattacharya et al. 2011; Courtin et al. 2011; Angulo et al. 2012; Watson et al. 2013). Most of the above studies focus on the friends-of-friends (FoF) halo definition (Davis et al. 1985). However, real cluster samples are typically defined in terms of spherical overdensity masses. Only very few mass functions exist for different overdensity definitions (e.g. Tinker et al. 2008; Watson et al. 2013), and the parametrization in Tinker et al. (2008) has developed into the standard reference used in most cluster cosmology analyses.

For a particular mass function parametrization to be useful in cosmological studies, it is crucially important that it correctly captures the variation in the mass function with redshift, and the sensitivity to cosmological parameters of interest such as the matter density  $\Omega_m$ , the dark energy density  $\Omega_\Lambda$ , the dark energy equation of state parameter  $w$ , and  $\sigma_8$ . An ideal situation would be for the mass function shape parametrization to be universal, where the variation with cosmology would be entirely captured by the cosmological sensitivity of the linear power spectrum of density fluctuations. For a FoF halo definition with linking length  $b = 0.2$ , or spherical overdensity  $\Delta_{180, \text{mean}}$ , the mass function was found to be approximately universal over a wide range of redshifts and cosmologies (Jenkins et al. 2001). More recently, Bhattacharya et al. (2011) used a set of  $\Lambda\text{CDM}$  and  $w\text{CDM}$  simulations to investigate the dependence of the FoF mass function with cosmology. Their fit is accurate to 2% for  $\Lambda\text{CDM}$ , and it describes the  $w\text{CDM}$  mass function to within 10%. Similar results are also reported in Courtin et al. (2011), although with slightly larger uncertainties.

Any mass function obtained from  $N$ -body dark matter only simulations potentially suffers from some bias introduced by neglecting the baryonic component of the clusters. Recently, various authors have investigated the baryonic impact on the halo mass function using hydrodynamic simulations (e.g. Cui et al. 2012, 2014; Cusworth et al. 2014; Martizzi et al. 2014; Schaller et al. 2014; Velliscig et al. 2014; Vogelsberger et al. 2014). Their conclusions are highly sensitive to the details of the treatment of the baryonic component. For example, models without feedback from active galactic nuclei (AGN) lead to higher cluster masses (or higher abundance at fixed mass) than dark matter only simulations. Adding AGN feedback, however, leads to fits that are up to 20% lower than, or about equal to the dark matter only prediction. Also, these baryonic effects are stronger for low cluster masses, and hardly affect the high-mass population. These shifts in the predicted mass functions nearly correspond to the level of uncertainty from current cluster abundance measurements. Therefore, studies of the baryonic impact on the halo mass function are extremely important for progress in cluster cosmology.

In this work, we analyse haloes extracted from the *Magneticum* simulations (Dolag et al., in prep.; see also Hirschmann et al. 2014; Saro et al. 2014). These are a set of hydrodynamical simulations covering large cosmological volumes at a variety of resolutions. We use these data to calibrate a cluster mass function that takes into account baryonic effects. This paper is organized as follows: In Section 5.2 we present the *Magneticum* simulations and describe how the cluster sample is extracted. We discuss theoretical aspects of the mass function in Section 5.3, where we also introduce the analysis method used to perform the fits. We present our mass function fits in Section 5.4, and discuss the cosmological impact in Section 5.5. We summarize and discuss our results in Section 5.6, where we also present step-by-step instructions on how to use our mass function fitting formulae.

We consider the following spherical overdensity mass definitions: (1) “mean overdensity” mass  $M_{200m}$ , which is the mass enclosed within a sphere of radius  $r_{200m}$ , in which the mean matter density is equal to 200 times the Universe’s mean matter density  $\bar{\rho}_m(z)$  at the cluster’s redshift, and (2) “critical overdensity” masses  $M_{500c}$  ( $M_{200c}$ ), which are analogous to (1) but enclosed within  $r_{500c}$  ( $r_{200c}$ ), and defined with respect to the critical density  $\rho_{\text{crit}}(z)$ . The corresponding overdensities are  $\Delta_{200m}$ ,  $\Delta_{500c}$  and  $\Delta_{200c}$ . The critical density is  $\rho_{\text{crit}}(z) = 3H^2(z)/8\pi G$ , where  $H(z)$  is the Hubble parameter. The mean matter density is  $\bar{\rho}_m(z) = \Omega_m(z)\rho_{\text{crit}}(z)$  with  $\Omega_m(z) = \Omega_m(1+z)^3/E^2(z)$ , and where  $E(z) \equiv H(z)/H_0$ .

## 5.2 Simulations and Cluster selection

We will refer to our hydrodynamical simulations as “Hydro”, and to our dark matter only simulations as “DMonly”.

### 5.2.1 The *Magneticum* simulations

In this work, we analyse a subset of cosmological boxes from the *Magneticum* Pathfinder simulation set (Box1/mr, Box3/hr, Box4/uhr; Dolag et al., in prep.). The simulations are based on the parallel cosmological TreePM-SPH code P-GADGET3 (Springel 2005). We use an entropy-conserving formulation of SPH (Springel & Hernquist 2002) and a higher order kernel based on the bias-corrected, sixth-order Wendland kernel (Dehnen & Aly 2012) with 295 neighbours, which together with a low-viscosity SPH scheme allows us to properly track turbulence within galaxy clusters (Dolag et al. 2005; Donnert et al. 2013).

We also allow for isotropic thermal conduction with 1/20 of the classical Spitzer value (Dolag et al. 2004). The simulation code includes a treatment of radiative cooling, heating from a uniform, time-dependent ultra-violet background and star formation with the associated feedback processes. The latter is based on a sub-resolution model for the multiphase structure of the interstellar medium (Springel & Hernquist 2003).

We compute radiative cooling rates following the same procedure as presented by Wiersma et al. (2009), and account for the presence of an evolving ultraviolet background (Haardt & Madau 2001). Contributions to cooling from each element have been pre-computed using the publicly available CLOUDY photo-ionisation code (Ferland et al. 1998) for an optically thin gas in (photo-)ionisation equilibrium.

Our simulations also incorporate a detailed treatment of stellar evolution and chemical enrichment following Tornatore et al. (2007), a multiphase model for star-formation (Springel & Hernquist 2003), and feedback processes associated with supernovae driven galactic winds and AGN (Springel & Hernquist 2003; Di Matteo et al. 2008; Fabian 2010). Additional details about the simulation code are available elsewhere (Hirschmann et al. 2014).

Initial conditions are created from a spatially flat  $\Lambda$ CDM cosmology with matter density  $\Omega_m = 0.272$ , baryon density  $\Omega_b = 0.0456$ , variance in the matter field<sup>1</sup>  $\sigma_8 = 0.809$ , and Hubble constant  $H_0 = 70.4 \text{ km s}^{-1} \text{ Mpc}^{-1}$ . The simulations cover a cosmological volume with periodic boundary conditions initially occupied by an equal number of gas and dark matter particles. Their relative masses reflect the global baryon fraction  $\Omega_b/\Omega_m$ . To minimize numerical differences between the Hydro and the DMonly set of simulations, we set up the DMonly simulations with an equal number of two types of collisionless particles, whose masses are equal to the mass of the dark matter and of the gas particles, respectively, of the corresponding Hydro runs.

### 5.2.2 Halo selection

The set of cosmological boxes used in this analysis is highlighted in Table 5.1. Haloes are initially identified through a parallel FoF algorithm with linking length  $b = 0.16$ . The FoF links over dark matter particles only. We then compute spherical overdensity masses (for overdensities  $\Delta_{200m}$ ,  $\Delta_{200c}$  and  $\Delta_{500c}$ ) of each halo centered at the deepest potential point with the parallel SUBFIND algorithm (Springel et al. 2001; Dolag et al. 2009).

<sup>1</sup>See Equation 5.2 for the definition.

Table 5.1 Boxes of the *Magneticum* simulations used in this work. The number of haloes  $N(z = 0)$  refer to the DMonly runs, and  $M_{200m}$ .

Box	Size $L_{\text{box}}$ (Mpc)	$m_{\text{DMparticle}}$ ( $M_{\odot}$ )	$M_{\text{Halo, min}}$ ( $M_{\odot}$ )	$N(z = 0)$
4/uhr	68.1 Mpc	$5.3 \times 10^7$	$6.2 \times 10^{11}$	835
3/hr	181.8 Mpc	$9.8 \times 10^8$	$1.1 \times 10^{13}$	1049
1/mr	1274 Mpc	$1.9 \times 10^{10}$	$2.2 \times 10^{14}$	8824

To ensure that haloes extracted from the Hydro simulations are not affected by issues related to resolution and numerical artefacts, we apply very conservative convergence criteria. For each box, and for each overdensity  $\Delta$ , we only consider haloes that contain more than  $10^4$  dark matter particles within  $r_{\Delta}$ . We then construct catalogues applying the lower mass limits shown in Table 5.1. We further apply an upper mass limit that corresponds to the lower limit of the next larger box, or to  $10^{16} M_{\odot}$  for the largest boxes (see also Figure 5.1). We extract cluster catalogues at seven redshifts<sup>2</sup> that are roughly equally spaced in cosmic time with  $\Delta t \sim 1.6$  Gyr. This time step is chosen to be larger than the typical dynamic time of a cluster, and we therefore work under the assumption that there is no correlation between the different snapshots.

## 5.3 Analysis Method

We provide the theoretical background on the halo mass function and introduce the fitting form we will adopt. We also present the method used to perform the multi-dimensional fits when analysing the cluster catalogues extracted from our simulations.

### 5.3.1 The halo mass function

The comoving number density of haloes of mass  $M$  is

$$\frac{dn}{dM} = f(\sigma) \frac{\bar{\rho}_m}{M} \frac{d \ln \sigma^{-1}}{dM}, \quad (5.1)$$

with the mean matter density  $\bar{\rho}_m$  (at redshift  $z = 0$ ), and

$$\sigma^2(M, z) \equiv \frac{1}{2\pi^2} \int P(k, z) \hat{W}^2(kR) k^2 dk, \quad (5.2)$$

which is the variance of the matter density field  $P(k, z)$  smoothed with the Fourier transform  $\hat{W}$  of the real-space top-hat window function of radius  $R = (3M/4\pi\bar{\rho}_m)^{1/3}$ . The function  $f(\sigma)$  is commonly parametrized as

$$f(\sigma) = A \left[ \left( \frac{\sigma}{b} \right)^{-a} + 1 \right] \exp \left( -\frac{c}{\sigma^2} \right) \quad (5.3)$$

with four parameters  $A, a, b, c$  that need to be calibrated (e.g. Jenkins et al. 2001). Here,  $A$  sets the overall normalization,  $a$  and  $b$  are the slope and normalization of the low-mass power law, and  $c$  sets the scale of a high-mass exponential cutoff. The function  $f(\sigma)$  has been shown to be approximately universal (Jenkins et al. 2001), meaning that it is only weakly dependent on redshift and cosmology.

In this work we allow departures from universality by parametrizing a possible redshift dependence as a

<sup>2</sup>For the Hydro runs, we use Box4/uhr for redshifts  $z \geq 0.13$ .

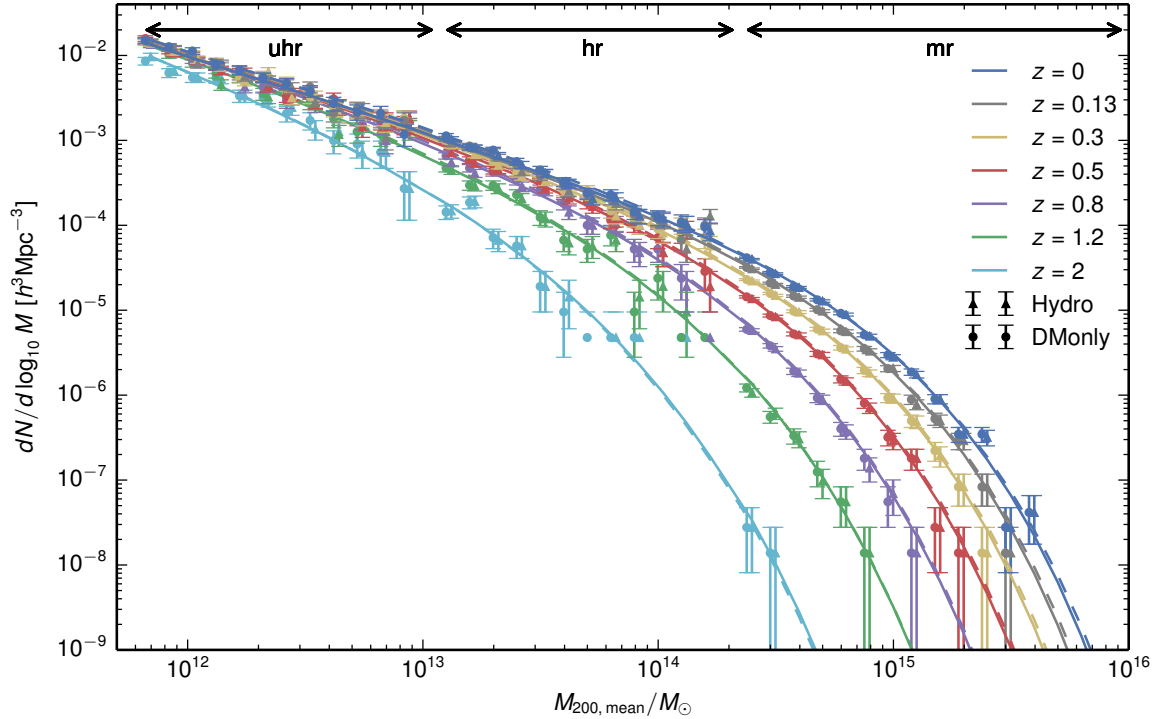


Figure 5.1 Mass function  $dN/d \log_{10} M$  from our Hydro and DMonly simulations. The data points are slightly offset in mass for better readability. We also show the best-fitting functions for Hydro (solid lines) and DMonly (dashed lines) which, however, are hardly distinguishable in this figure given its dynamic range.

power law of  $1 + z$ :

$$\begin{aligned} A(z) &= A_0(1+z)^{A_z} \\ a(z) &= a_0(1+z)^{a_z} \\ b(z) &= b_0(1+z)^{b_z} \\ c(z) &= c_0(1+z)^{c_z} \end{aligned} \quad (5.4)$$

where the subscript 0 denotes the values at redshift  $z = 0$ , and where  $A_z, a_z, b_z, c_z$  are additional fit parameters. Note that many authors assume the cutoff scale  $c$  to be constant under the assumption of self-similarity (e.g. Tinker et al. 2008; Watson et al. 2013).

### 5.3.2 Mass function for spherical overdensity masses

Many studies of the halo mass function are performed using the FoF technique. For a linking length  $b \simeq 0.2$ , the resulting mass function is very close to being universal (Jenkins et al. 2001). However, for observational reasons, real cluster masses are measured in terms of spherical overdensity masses. When using a suitable spherical overdensity  $\Delta_{\text{mean}} \sim 180$ , the above mass function fitting formula is still close to being universal (Jenkins et al. 2001). Similarly, Tinker et al. (2008) use  $\Delta_{200m}$  as their universal mass definition, and Watson et al. (2013) argue for  $\Delta_{178m}$ . These overdensity definitions are all very similar; we adopt  $\Delta_{200m}$  in this work.

We also want to calibrate the mass function for  $M_{500c}$ , which is a convenient mass definition within X-ray studies of clusters where the emission cannot easily be traced beyond  $r_{500c}$ , and for  $M_{200c}$ , which is used for

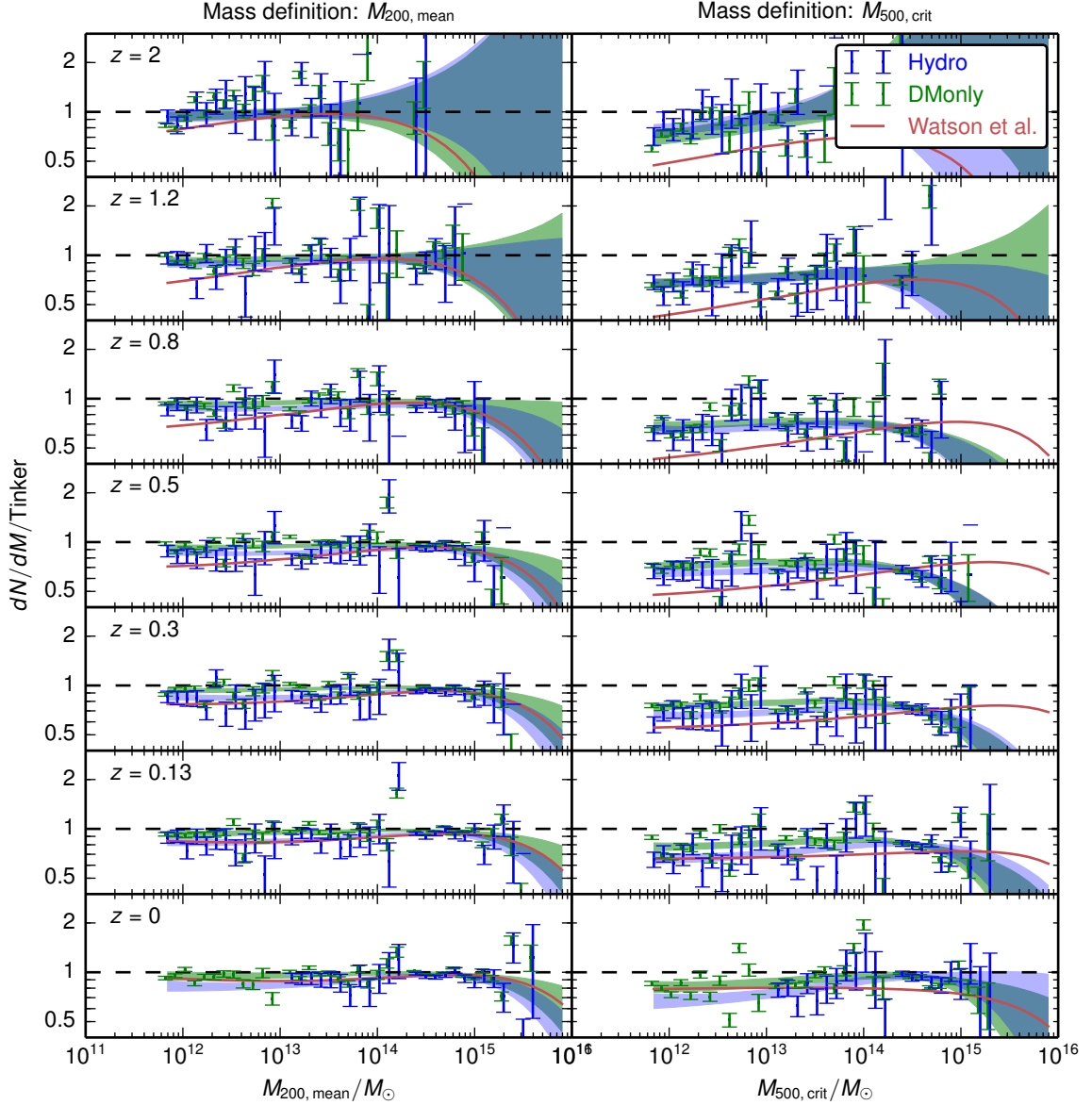


Figure 5.2 Number density of clusters from our simulations relative to the fit by Tinker et al. (2008) for overdensity masses  $M_{200m}$  (left panels) and  $M_{500c}$  (right panels). The coloured regions correspond to the  $2\sigma$  allowed regions of our fits, and the data points are slightly offset in mass for better readability. The red line shows the fit by Watson et al. (2013), which for  $M_{200m}$  exhibits a similar high-mass behavior as ours, predicting less clusters than Tinker et al. (2008).

measurements of cluster galaxy velocity dispersions and of weak gravitational lensing shear profiles. It is not a priori clear that one can simply use the same form of the fitting function that is valid for  $M_{200m}$ , as one might miss some redshift and cosmology dependent behavior. Remember, for example, the very different redshift evolutions of  $\bar{\rho}_m(z)$  and  $\rho_{\text{crit}}(z)$ .

Tinker et al. (2008) provide the mass function for a range of different  $\Delta_{\text{mean}}$ , and one uses  $\Delta_{\text{mean}}(z) = \Delta_{\text{crit}}/\Omega_m(z)$  to convert from critical to mean density as a function of redshift. Their approach relies on the implicit assumption that the fitting function correctly captures the behavior for every  $\Delta_{\text{mean}}$ . Watson et al. (2013) provide a correction to their  $\Delta_{178m}$  mass function that depends on  $\Delta_{\text{mean}}(z)$ .

For now, we focus on  $\Delta_{500c}$ , and we choose the following approach: Assuming that the mass function  $dn/dM_{200m}$  is universal, the mass function in  $M_{500c}$  can be expressed as

$$\frac{dn}{dM_{500c}} = \frac{dn}{dM_{200m}} \frac{dM_{200m}}{dM_{500c}} = f(\sigma) \frac{\bar{\rho}_m}{M_{500c}} \frac{d \ln \sigma^{-1}}{dM_{500c}} \times \frac{M_{500c}}{M_{200m}}. \quad (5.5)$$

This mass function should have the same universal properties as the mass function in  $M_{200m}$ .

The crucial, evolving part is now captured in the factor  $M_{500c}/M_{200m}$ . These masses can be converted from one to the other assuming a cluster density profile (e.g. Navarro et al. 1997) and a mass-concentration relation (e.g. Duffy et al. 2008). Therefore, the conversion depends on mass, redshift, and  $\Omega_m$  (which is involved in the overdensity conversion). The following prescription is a good fit at the few percent level in the range  $0 < z < 2$ ,  $10^{13} < M_{500c}/M_\odot < 2 \times 10^{16}$ , and  $0.1 < \Omega_m < 0.5$ :

$$\frac{M_{500c}}{M_{200m}} \equiv \alpha + \beta \ln M_{500c}. \quad (5.6)$$

The parameters  $\alpha$  and  $\beta$  are functions of  $\Omega_m$  and redshift:

$$\begin{aligned} \beta(\Omega_m) &= -1.70 \times 10^{-2} + \Omega_m 3.74 \times 10^{-3} \\ \alpha(\Omega_m, z) &= \alpha_0 \frac{\alpha_1 z + \alpha_2}{z + \alpha_2} \\ \alpha_0(\Omega_m) &= 0.880 + 0.329 \Omega_m \\ \alpha_1(\Omega_m) &= 1.00 + 4.31 \times 10^{-2}/\Omega_m \\ \alpha_2(\Omega_m) &= -0.365 + 0.254/\Omega_m. \end{aligned} \quad (5.7)$$

Note that the fit relies on cluster density profiles and a mass-concentration relation that were calibrated against (dark matter only)  $N$ -body simulations. Also, one should expect the presence of some scatter in these relations. For these reasons, we do not expect that simply applying Equation 5.5 to the  $M_{200m}$  mass function is sufficient to fully describe the mass function in  $M_{500c}$ . Therefore, in addition to applying the  $M_{500c}/M_{200m}$  fit and Equation 5.5, we also fit for all 8 free parameters of Equations 5.3 and 5.4.

In an analogous way, we establish the mass function for  $\Delta_{200c}$ . It is presented in the Appendix.

### 5.3.3 Finite volume correction

Throughout this work, we use cluster samples produced by simulations to understand the mass function observed in the real Universe. However, there is one subtle difference that needs to be accounted for: in contrast to the Universe, every simulation box is finite in size. Therefore, we can only capture modes in the density field that are smaller than  $L_{\text{box}}$ . This means that there is an upper mass limit corresponding to the longest modes, beyond which the simulations will systematically underestimate the number of objects.

We correct for this effect following the approach of previous analyses (Lukić et al. 2007; Bhattacharya et al. 2011; Watson et al. 2013). Briefly, the variance of fluctuations  $\sigma(M)$  is corrected by subtracting the variance at scales corresponding to the box size  $\sigma(R_{\text{box}})$ :

$$\sigma_{\text{corrected}}^2(M) = \sigma_{\text{theory}}^2(M) - \sigma^2(R_{\text{box}}), \quad (5.8)$$

Table 5.2 Best-fitting mass function parameters for DMonly and Hydro simulations. The covariance matrix for Hydro  $M_{500c}$  is shown in Table 5.3. The mass functions for  $M_{500c}$  and  $M_{200c}$  are calculated from Equations 5.5 and 5.10, respectively.

Parameter	$\chi^2/\nu(N > 10)$	A	a	b	c	$A_z$	$a_z$	$b_z$	$c_z$
$M_{200m}$									
DMonly	0.84	0.216	1.87	2.02	1.31	0.018	-0.0748	-0.215	-0.0689
Hydro	1.09	0.240	2.43	1.65	1.41	0.365	-0.129	-0.453	-0.138
$M_{200c}$									
DMonly	1.06	0.256	2.01	1.97	1.59	0.218	0.290	-0.518	-0.174
Hydro	1.11	0.290	2.69	1.58	1.70	0.216	0.027	-0.352	-0.226
$M_{500c}$									
DMonly	0.87	0.390	3.05	1.72	2.32	-0.924	-0.421	0.190	-0.509
Hydro	0.81	0.322	3.24	1.71	2.29	0.0142	-0.219	-0.275	-0.428

Table 5.3 Covariance matrix for our Hydro mass function in  $M_{500c}$ . The corresponding best-fitting values are shown in Table 5.2.

	A	a	b	c	$A_z$	$a_z$	$b_z$	$c_z$
A	$1.77 \times 10^{-3}$	$8.29 \times 10^{-3}$	$-4.77 \times 10^{-3}$	$2.20 \times 10^{-3}$	$-7.42 \times 10^{-3}$	$-2.38 \times 10^{-3}$	$3.45 \times 10^{-3}$	$-9.54 \times 10^{-4}$
a		$7.52 \times 10^{-2}$	$-2.26 \times 10^{-2}$	$2.47 \times 10^{-2}$	$-2.25 \times 10^{-2}$	$-2.25 \times 10^{-2}$	$9.89 \times 10^{-3}$	$-1.27 \times 10^{-2}$
b			$1.45 \times 10^{-2}$	$-4.89 \times 10^{-3}$	$2.15 \times 10^{-2}$	$7.75 \times 10^{-3}$	$-1.14 \times 10^{-2}$	$2.14 \times 10^{-3}$
c				$9.64 \times 10^{-3}$	$-3.37 \times 10^{-3}$	$-6.38 \times 10^{-3}$	$7.88 \times 10^{-5}$	$-5.03 \times 10^{-3}$
$A_z$					$1.17 \times 10^{-1}$	$3.96 \times 10^{-2}$	$-6.64 \times 10^{-2}$	$6.91 \times 10^{-3}$
$a_z$						$3.26 \times 10^{-2}$	$-2.34 \times 10^{-2}$	$1.12 \times 10^{-2}$
$b_z$							$4.09 \times 10^{-2}$	$-2.50 \times 10^{-3}$
$c_z$								$5.98 \times 10^{-3}$

where, for simplicity, we equate the spherical volume  $4/3\pi R_{\text{box}}^3$  to the cubical simulation volume  $L_{\text{box}}^3$ . However, as we apply upper mass limits to the cluster samples (see Section 5.2.2), the correction has negligible impact on our analysis. In fact, for each box size, the correction would become important at masses that are about 2 orders of magnitude larger than the corresponding upper mass limit we apply. We test these finite volume effects by reproducing the results presented in Section 5.4 without the correction; in this case, the results do not significantly change. Nevertheless, we apply the correction to each of our boxes.

### 5.3.4 Parameter estimation

We use a Bayesian likelihood approach, which allows us to correctly capture the Poisson errors on the measured number of clusters as a function of their mass and redshift. This choice differs from using (Gaussian)  $\chi^2$  statistics (e.g. Tinker et al. 2008), or corrections to  $\chi^2$  statistics to account for the Poisson errors (e.g. Watson et al. 2013).

The likelihood at each point  $\mathbf{p}$  in parameter space is calculated in the following way: We calculate the matter power spectrum using the transfer function of Eisenstein & Hu (1998, 1999), taking baryonic effects into account. This is the same prescription used to set up the initial conditions of the *Magneticum* simulations. We evaluate the likelihood  $\mathcal{L}$  by applying Poisson statistics in log-spaced mass bins of size  $\Delta \log_{10} M = 0.1$  (Cash 1979):

$$\ln \mathcal{L} = \sum_i \ln \frac{dn(M_i|\mathbf{p}, z_i)}{dM} - \int \frac{dn(M|\mathbf{p}, z)}{dM} dM, \quad (5.9)$$

up to an arbitrary constant, and where  $i$  runs over all clusters in the sample. The second term equals the total number of expected clusters. We have checked that decreasing the bin size does not change our results.

In practice, given a set of parameters  $\mathbf{p}$ , we perform the above calculation for each redshift and for each of the simulation boxes, and sum the log-likelihoods. When fitting for the mass function in this way, we are

facing a problem with moderately large dimensionality (8 free parameters); we utilize the `emcee`<sup>3</sup> code for efficient exploration of parameter space (Foreman-Mackey et al. 2013). We test our fitting procedure against several mock catalogues that contain a factor 100 times more clusters than our simulation data. In these tests we recover the input values within the statistical uncertainties and conclude that our fitting method is unbiased to a level that is much smaller than the uncertainties we report.

## 5.4 *Magneticum* mass functions

In Figure 5.1, we show the number density of haloes from our Hydro and DMonly simulations at seven different redshifts. The error bars show the Poisson uncertainty on the measured numbers. We also show the best-fitting functions for both data sets. Note that the differences in shape and amplitude of the mass function that we are going to discuss throughout this work are on the order of  $\sim 10\%$  and are therefore hardly visible in this figure given its large dynamic range.

### 5.4.1 Impact of baryons

The impact of baryons can be seen in Figure 5.2. We show the number density of clusters from our simulations relative to the Tinker et al. (2008) fitting function. The colored bands correspond to the allowed  $2\sigma$  region of our fits. For reference, the red line shows another dark matter only fitting function (Watson et al. 2013).

The left panels of Figure 5.2 show the mass function for spherical overdensity masses  $M_{200m}$ . Overall, our DMonly results agree well with the literature studies. On the high-mass end, the Tinker et al. (2008) fit shows some differences with both our simulations and Watson et al. (2013), and seems to overestimate the abundance of these objects by  $\sim 30\%$ . However, this is for large masses greater than  $\sim 2 \times 10^{15} M_\odot$ , which is just outside of the mass range  $M \lesssim 10^{15} h^{-1} M_\odot$  of the fit by Tinker et al. (2008). Our samples also start to run out of objects at  $\sim 2 - 3 \times 10^{15} M_\odot$  but our fit agrees pretty well with Watson et al. (2013) who trust their fit up to nearly  $10^{16} M_\odot$ .

The comparison of our DMonly and Hydro simulations tells an interesting story: At  $z = 2$ , the highest redshift we consider, there is essentially no difference between our DMonly and Hydro mass functions. As time goes by and structure formation continues, baryonic effects become important. At redshift  $z \sim 1$ , we observe that baryon depletion is important for low-mass clusters up to  $\sim 10^{14} M_\odot$ . At fixed mass, this reduces the number density of clusters by  $\sim 10\%$ . Further following the redshift evolution, we observe that the effects of baryon depletion propagate up to more massive clusters. For low redshifts  $z \lesssim 0.3$ , our Hydro mass function is low by about 10% compared to the DMonly case.

The right panels of Figure 5.2 show the mass functions for  $M_{500c}$ . The differences between our Hydro and DMonly data follow the discussion above, with the Hydro abundance being about  $\sim 10\%$  low compared to DMonly. Again, we observe that our simulations predict significantly less high-mass clusters  $M \gtrsim 10^{15} M_\odot$  than Tinker et al. (2008). This time however, our mass functions also prefer an overall lower abundance by about  $\sim 20\%$  than Tinker et al. (2008). The fitting function by Watson et al. (2013) predicts even lower abundances that are typically 20% to 40% lower than the Tinker et al. (2008) mass function over the full mass range.

The fact that all mass functions considered here agree quite well for  $M_{200m}$ , and much less for  $M_{500c}$  might provide a hint for systematic differences in the analysis methods employed. We propose two effects that could (at least partially) explain these differences. First,  $M_{500c}$  probes a more central, and much smaller part of a cluster than  $M_{200m}$ . Therefore, care must be taken to prevent resolution effects from becoming important. We use a minimum number of  $10^4$  dark matter particles enclosed within  $r_\Delta$  for all values of  $\Delta$  we consider. Tinker et al. (2008) use a mass re-scaling for overdensities larger than  $\Delta_{600m}$ . Watson et al. (2013) fit for overdensities up to  $\Delta_{1600m}$ , corresponding only to  $\Delta_{432c}$  at redshift 0. Second, in all cases the fitting function for  $\Delta_{200m}$  is given by Equations 5.1–5.4, which leaves little room for differences in the analysis method. For  $\Delta_{500c}$ , however, the situation is different. We follow the method described in Section 5.3.2, Tinker et al. (2008)

<sup>3</sup><http://dan.iel.fm/emcee/current>

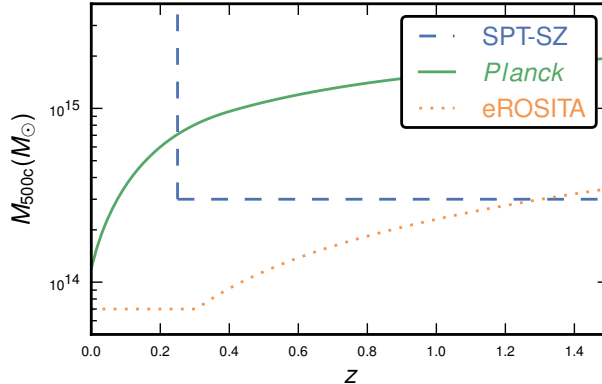


Figure 5.3 Selection functions we use to generate idealized representations of the SPT, *Planck* and eROSITA cluster catalogues.

present their fit parameters for a range of values for  $\Delta_m$ , and Watson et al. (2013) provide a fitting function for different overdensities  $\Delta_m \leq 1600$ . These different approaches could indeed lead to different results, and we will come back to this later in Section 5.5.

#### 5.4.2 Mass function fits

In Table 5.2, we present the parameters that maximize the likelihood for the data obtained from our DMonly and Hydro simulations. For reference, we estimate the  $\chi^2$  per degree of freedom  $v$  at the best-fitting location, assuming Poisson errors on the number of objects in each bin. We therefore only take bins with more than 10 haloes into account. The values of  $\chi^2/v$  obtained in this way all lie between 0.8 – 1.1.

The parameters for  $\Delta_{200m}$  can be directly compared with the literature, and as expected from Figure 5.2, there is reasonably good agreement. In particular, for DMonly, we find a value of the exponential cut-off scale  $c = 1.31 \pm 0.04$  that is in very good agreement with Watson et al. (2013), but significantly larger than  $c = 1.19$  in Tinker et al. (2008). Note that a large value of  $c$  corresponds to a low cut-off scale in mass (see Equation 5.3), in agreement with the behavior shown in Figure 5.2. Finally, in the DMonly case, we find mild evidence for redshift-evolution of the cut-off scale,  $c_z = -0.07 \pm 0.05$ ; this evolution is stronger for Hydro, where  $c_z = -0.14 \pm 0.03$ .

The parameters for  $\Delta_{200c}$  and  $\Delta_{500c}$  are relevant for observational studies. For the latter, we also show the covariance matrix for the Hydro mass function parameters in Table 5.3. It should be used with the best-fitting parameters from Table 5.2 to capture the uncertainties related to our mass function. For reference, the uncertainty on the normalization  $A$  is about 13%.

### 5.5 Cosmological impact

There are differences between the mass functions extracted from our Hydro and DMonly simulations, and fits from the literature. When used to interpret real cluster samples, the different mass functions will ultimately lead to different cosmological results. In the following, we quantify and discuss this effect. To this end, we create simulated cluster catalogues using our best-fitting Hydro mass function, and use either the Hydro, the DMonly, or literature fits to perform cosmological analyses. Because the baryonic impact on the mass function depends on mass and redshift, we expect qualitatively different shifts when using different mass functions depending on the specific properties of a cluster survey. Therefore, we create and analyse three sets of simulated catalogues,

Table 5.4 Mean recovered cosmological parameter values from different mass functions for simulated cluster samples. We do not show errors because we are interested in absolute shifts only.

Parameter	$\Omega_m$	$\sigma_8$	$\sigma_8(\Omega_m/0.27)^{0.3}$
Input	0.272	0.809	(0.8108)
<b>SPT-like sample</b>			
Hydro	0.278	0.805	0.813
DMonly	0.283	0.802	0.814
Tinker08	0.252	0.785	0.769
<b>eROSITA-like sample</b>			
Hydro	0.272	0.810	0.811
DMonly	0.261	0.813	0.805
Tinker08	0.252	0.784	0.768
<b>Planck-like sample</b>			
Input	0.316	0.83	(0.8701)
Hydro	0.323	0.824	0.870
DMonly	0.321	0.827	0.871
Tinker08	0.335	0.773	0.825

whose properties approximately match real samples from the South Pole Telescope (SPT; Carlstrom et al. 2011), the *Planck* satellite (Tauber et al. 2010) and eROSITA (Predehl et al. 2014). The selection functions we assume are shown in Figure 5.3 and will be discussed in more detail. All samples are defined with respect to  $M_{500c}$ .

We use the fit method described in Section 5.3, but we now fit for the cosmological parameters, and keep the mass function parameters fixed. Since no covariance matrix is available for the literature mass functions we compare to, we use our best-fitting parameters without uncertainties, too, in order to make a comparison on equal footing. However, we also show how using the covariance matrix mildly degrades the results. We restrict this analysis to the parameters  $\Omega_m$  and  $\sigma_8$ , which strongly affect the measured cluster abundance. Remember that these parameters enter the mass function calculation in Equation 5.1 through their impact on the matter power spectrum  $P(k, z)$  and the matter density  $\bar{\rho}_m$ . The  $\Omega_m$ - $\sigma_8$  likelihood contours from the cluster number counts experiment exhibit a characteristic, elongated degeneracy in the  $\Omega_m$ - $\sigma_8$  plane (see Figures 5.4 & 5.5(b)). The parameter combination  $\sigma_8(\Omega_m/0.27)^{0.3}$  is interesting because it reflects the width of this degeneracy, i.e. the direction in  $\Omega_m$ - $\sigma_8$  space which is best constrained using clusters. We show the constraints we recover on this parameter combination, too.

In this test, we directly use the simulated cluster masses. That is, we do not include any systematic uncertainties and measurement errors related to mass estimations as one would have to do for a real cluster sample. This also means that the uncertainties we present represent the statistical uncertainties related to the sample size, and cannot be compared directly with actual results from real data. The aim of this analysis is to investigate and quantify offsets related to the mass function, which justifies this simplified approach. For this same reason, we choose not to quote the errors on the recovered parameters.

The typical uncertainties on the cosmological parameters from current cluster samples are  $\sigma(\Omega_m) \sim \sigma(\sigma_8) \sim \sigma(\sigma_8(\Omega_m/0.27)^{0.3}) \sim 0.03$  (e.g. Planck Collaboration et al. 2014c; Mantz et al. 2015). We will refer to these characteristic numbers in the following.

### 5.5.1 Cosmological analysis of an SPT-like cluster sample

While the SPT sample is selected through the cluster Sunyaev–Zel’dovich effect (SZE; Sunyaev & Zel’dovich 1972) signature, we approximate the catalogue as mass-selected with  $M > 3 \times 10^{14} M_\odot$ , and restrict to redshifts  $z > 0.25$  (see Figure 5.3 and cf. Bleem et al. 2015). For the SPT survey of size  $2500 \text{ deg}^2$ , our simulated catalogue contains  $\sim 700$  systems. We consider three different input cosmologies with different values of  $\Omega_m = 0.22, 0.272, 0.4$  with the same  $\sigma_8 = 0.809$  in each case. A subset of the results appear in Table 5.4 and Figure 5.4.

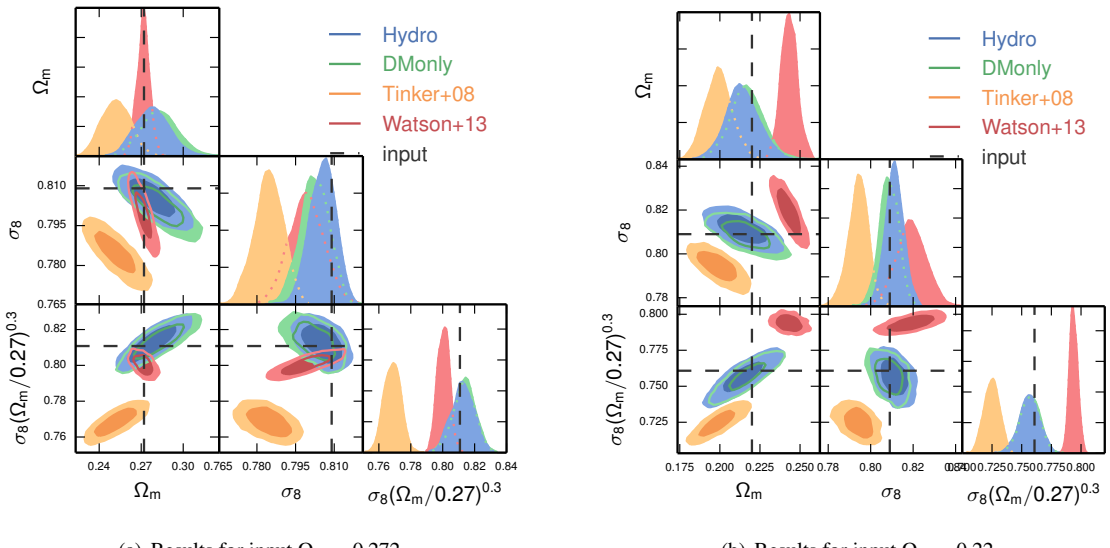
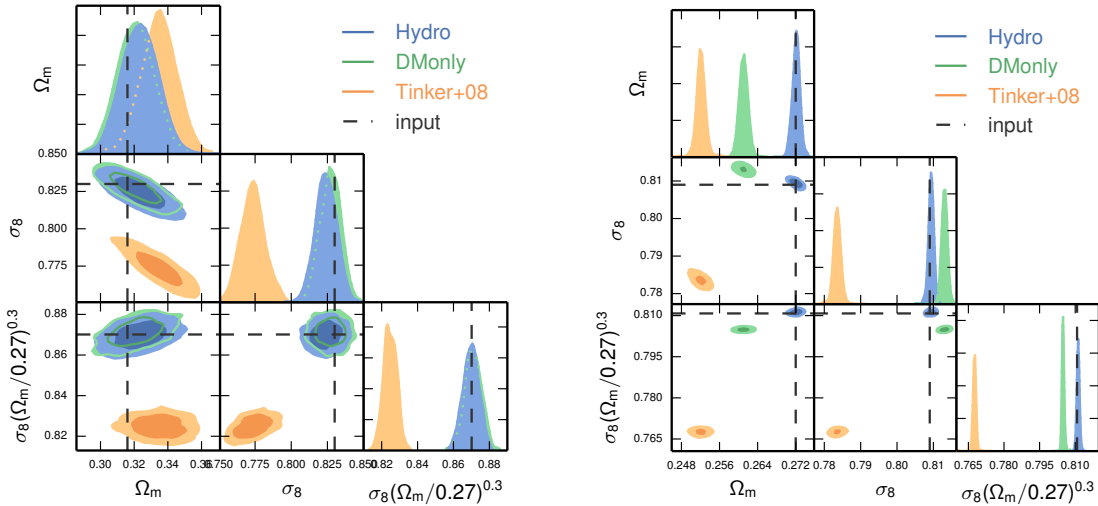


Figure 5.4 Cosmological results from simulated SPT-like cluster samples, created using our Hydro mass function. The two different input cosmologies are marked by the dashed lines, in both cases  $\sigma_8 = 0.809$ . We show likelihood contours (68% and 95% confidence) in  $\Omega_m$ - $\sigma_8$ - $\sigma_8(\Omega_m/0.27)^{0.3}$  space. Results obtained from different mass functions are colour-coded. The baryonic impact of the halo mass function is negligible for this high-mass and high-redshift sample. In both cases there is a shift toward larger values of  $\Omega_m$  and  $\sigma_8$  compared to when using Tinker et al. (2008). The constraints obtained from Watson et al. (2013) are tighter, but seem to be biased towards  $\Omega_m \sim 0.27$ . See discussion in the text for more details.



(a) Results for a simulated *Planck*-like cluster sample. The input cosmology is chosen to match the *Planck* CMB constraints. Given the large mass limit of the sample there is little difference between the results from our Hydro or DMonly mass functions. Using the Tinker et al. (2008) fit, however, leads to a measurement of  $\sigma_8$  that is low by  $\Delta(\sigma_8) \sim 0.05$ .

(b) Result for a simulated eROSITA-like cluster sample. For this sample, there is a difference between the results from the Hydro and the DMonly mass functions, which is due to the impact of baryons. Neglecting the baryonic impact on the mass function leads to an underestimate of  $\Delta(\Omega_m) \sim -0.01$ . We also observe an offset between DMonly and Tinker et al. (2008).

Figure 5.5 Cosmological results from simulated realizations of approximations to the *Planck* and eROSITA cluster samples, created using our Hydro mass function. The input cosmologies are marked by the dashed lines. We show likelihood contours (68% and 95% confidence) in  $\Omega_m$ - $\sigma_8$ - $\sigma_8(\Omega_m/0.27)^{0.3}$  space. Results obtained from different mass functions are colour-coded.

The results from both our Hydro and DMonly mass functions show nearly perfect agreement, indicating that the effect of baryons on the halo mass function is negligible in this case. This is expected, because, as previously noted, the impact of baryons is most important for low-mass clusters at low redshifts (see Section 5.4.1). The SPT-like survey does not probe this mass and redshift regime.

The constraints we obtain using the Tinker et al. (2008) fit are somewhat off, with  $\Delta(\Omega_m) \simeq -0.03$  and  $\Delta(\sigma_8) \simeq -0.02$  compared to the Hydro. These shifts are roughly consistent throughout the range of input cosmologies, and can be interpreted as the systematic offset between the mass functions. Note that they are of the same order as the typical uncertainties from current cluster surveys.

The constraints obtained from the Watson et al. (2013) fit are slightly tighter than the ones just discussed. However, these results seem to be biased toward  $\Omega_m \sim 0.27$ . For example, the preferred value recovered for the sample with input  $\Omega_m = 0.22$  is  $\Omega_m(\text{Watson}) = 0.243$ , and we further obtain  $\Omega_m(\text{Watson}) = 0.309$  for an input value  $\Omega_m = 0.4$ . Their assumed form of the redshift dependence of the fit parameters (Equation 5.4 in this work, Equations 13–15 in Watson et al. 2013) involves  $\Omega_m(z)$ . We suspect that this parametrization introduces an implicit and spurious preference for  $\Omega_m \sim 0.27$ , which is their simulation input value. We will not consider the Watson et al. (2013) for the rest of this work.

We presented the covariance matrix for the Hydro mass function parameters in Table 5.3. We repeat the cosmological analysis using the Hydro mass function and its parameter covariances, and infer the additional systematic uncertainties  $\sigma_{\text{MF}}$  using quadrature addition. We find  $\sigma_{\text{MF}}(\Omega_m) = 0.013$  and  $\sigma_{\text{MF}}(\sigma_8) = 0.0071$ , and conclude that the systematic uncertainties on our mass function are small compared to the total uncertainties from current, real cluster samples.

### 5.5.2 Cosmological analysis of a *Planck*-like cluster sample

The *Planck* cluster sample is selected using the SZE, too, and extends down to redshift  $z = 0$ . However, the satellite's beam is larger than the SPT beam, and the survey mass limit varies significantly with redshift. We mimic the *Planck* selection function following the sample mass-redshift distribution shown in Figure 1 in Planck Collaboration et al. (2015b). We further assume a hydrostatic bias of  $1 - b \simeq 0.8$ , which then leads to the selection function we show in Figure 5.3. For this exercise, we choose our input cosmology to match the values preferred by the *Planck* CMB anisotropy measurement ( $\Omega_m = 0.316$ ,  $\sigma_8 = 0.83$ ,  $H_0 = 67.3 \text{ km s}^{-1} \text{ Mpc}^{-1}$ ; Planck Collaboration et al. 2015a). Assuming a sky coverage of 65%, the simulated catalogue contains  $\sim 600$  clusters.

The results are shown in Table 5.4 and Figure 5.5(a). We recover very similar constraints on  $\Omega_m$  using either mass function, even though the result from Tinker et al. (2008) is slightly high by 0.01. We recover identical constraints on  $\sigma_8$  using either the Hydro or DMonly mass functions, but the result obtained from Tinker et al. (2008) is significantly lower by  $\Delta(\sigma_8) \simeq -0.05$ . The parameter  $\sigma_8(\Omega_m/0.27)^{0.3}$  is low by a similar amount. This offset is qualitatively similar to – but larger than – the offset in our analysis of the SPT-like sample.

In their cluster cosmology analysis, the *Planck* collaboration has reported an apparent disagreement with parameters preferred by the CMB anisotropy measurements. This tension can be alleviated to some extent by adopting a more realistic treatment of the hydrostatic bias (Planck Collaboration et al. 2014c). In their latest analysis, the *Planck* collaboration considers measurements of the bias from several different authors; still all results have in common that the recovered value of  $\sigma_8$  is low by roughly 0.05–0.13 (Planck Collaboration et al. 2015b). Using our mass function instead of Tinker et al. (2008) would lead to a shift in  $\sigma_8$  by about +0.05, which would remove the difference between the *Planck* clusters and the CMB constraints.

### 5.5.3 Cosmological analysis of an eROSITA-like cluster sample

The eROSITA cluster sample will be X-ray flux selected and extend from redshift  $z = 0$ . For the present test, we assume a detection limit of 50 photons in the  $0.5 - 2.0 \text{ keV}$  band with a typical exposure time of 1.6 ks. We model this selection as a combination of a redshift-dependent mass threshold  $M > 2.3 z \times 10^{14} M_\odot$ , with an additional mass cut  $M > 7 \times 10^{13} M_\odot$  (see Figure 5.3 and compare with Figure 2 in Pillepich et al. (2012), and also Merloni et al. (2012); Borm et al. (2014)). The eROSITA full-sky catalogue simulated in this way contains  $\sim 1.5 \times 10^5$  clusters.

The results of the analysis of this sample appear in Table 5.4 and Figure 5.5(b). The recovered constraints are very tight due to the large cluster sample and the fact that we do not include mass measurement uncertainties. Once again, there is an offset between the results from Hydro and Tinker et al. (2008). However, while the constraints on  $\sigma_8$  from Hydro and DMonly are very similar, we now recover different values of  $\Omega_m$ . This is an indication that baryonic effects are indeed important for this sample. As previously discussed, baryons have their strongest impact on the halo mass function at low redshifts and for low masses, which is a regime that is well probed by eROSITA. Therefore, neglecting the baryonic impact and using the DMonly mass function would lead to an underestimate of  $\Delta\Omega_m \simeq -0.01$ . This bias is of the same order as the expected constraints from eROSITA  $\sigma(\Omega_m) \simeq 0.012$  (Pillepich et al. 2012), meaning that the impact of baryons on the mass function will have to be accounted for in the cosmology analysis.

## 5.6 Discussion and Conclusions

We investigate the impact of baryons on the halo mass function using the hydrodynamic *Magneticum* simulations together with dark matter only counterparts. Our simulations and the halo selection are characterized by (1) a treatment of the baryonic component and of AGN feedback that correctly reproduces several observations such as AGN luminosity functions (Hirschmann et al. 2014) and cluster pressure profiles (Planck Collaboration et al. 2013; McDonald et al. 2014), (2) large cosmological volumes probed by boxes of up to  $\sim 2 \text{ Gpc}^3$ ,

which allow us to track cluster masses up to a few  $\times 10^{15} M_{\odot}$  (e.g. Saro et al. 2014), and (3) a conservative halo selection with  $> 10^4$  dark matter particles within  $r_{\Delta}$ , minimizing potential biases related to numerical resolution. To avoid a different sampling of the initial density fluctuations, all DMonly simulations were run using two species of dark matter with masses corresponding to those of the dark matter and baryonic particles in the Hydro simulations.

We find that the presence of baryons tends to decrease the cluster masses, which – given the shape of the halo mass function – leads to a decrease of the expected number of objects for a given mass (see Figures 5.1 and 5.2). The number density of haloes decreases by up to  $\sim 15\%$  for low masses  $\lesssim \text{few} \times 10^{14} M_{\odot}$  and at low redshifts  $z \lesssim 0.5$ . At higher masses and redshifts, the Hydro mass functions agree very well with our DMonly results. Qualitatively similar results have been recently presented in other publications (Cusworth et al. 2014; Schaller et al. 2014; Velliscig et al. 2014; Vogelsberger et al. 2014). In contrast to these results, Cui et al. (2014) report that their hydro mass function is  $\sim 20\%$  below their DMonly counterpart with no significant mass or redshift dependence, and Martizzi et al. (2014) find a mild increase of the mass function due to baryons.

Comparing both our Hydro and DMonly mass functions with the most commonly used DMonly fit (Tinker et al. 2008), we find that our fits predict significantly fewer objects at high mass ( $\gtrsim 10^{15} M_{\odot}$ ). A similar observation has been made by Watson et al. (2013), who further argue that these high masses are beyond the range of validity of the Tinker et al. (2008) analysis.

Real cluster samples selected in the X-ray or SZE are typically defined using  $M_{500c}$  and  $M_{200c}$  masses. However, the mass function shape varies only weakly with redshift *and* cosmology when masses are defined either by FoF with  $b \simeq 0.2$ , or for spherical overdensity  $\Delta_{\text{mean}} \sim 200$ . Therefore, we introduce a mapping between  $M_{500c}$  ( $M_{200c}$ ) and  $M_{200m}$  as a function of mass, redshift, and  $\Omega_m$ , and argue that this allows us to use the universal properties of  $\Delta_{200m}$  also for masses defined by  $\Delta_{500c}$  ( $\Delta_{200c}$ ). In practice, our mass function fits are used as follows:

- Calculate  $\sigma(M, z)$  using Equation 5.2.
- Calculate  $f(\sigma, z)$  from Equations 5.3 & 5.4, using the parameters from Table 5.2.
- For  $\Delta_{200m}$ : The mass function is given by Equation 5.1.
- For  $\Delta_{500c}$ : Calculate  $M_{500c}/M_{200m}$  from Equations 5.6 & 5.7, and obtain the mass function from Equation 5.5.
- For  $\Delta_{200c}$ : Calculate  $M_{200c}/M_{200m}$  from Equations 5.11 – 5.13, and obtain the mass function using Equation 5.10.

Note that the same approach could be used to propagate the universal behavior of the  $\Delta_{200m}$  mass function to any overdensity  $\Delta$ .

We investigate how the differences among our Hydro, DMonly and some previously published mass functions affect cosmological results from cluster abundance measurements. To this end, we simulate idealized representations of the SPT, *Planck*, and eROSITA surveys, assuming simplified selection schemes as shown in Figure 5.3. We assume perfect knowledge of cluster masses  $M_{500c}$ , and do not account for any uncertainties or systematics related to mass-observable relations. Therefore, the cosmological parameter uncertainties we recover here are tighter than the actual constraints that would be obtained in a comprehensive analysis of real data. Moreover, neglecting the conversion from observable to mass would likely remove some cosmological dependencies. However, this test can be used as guidance in understanding the impact of mass function differences.

The results of these analyses can be summarized as follows (see also Figures 5.4 & 5.5 and Table 5.4):

- For the SPT-like sample, the impact of baryons is negligible, and we obtain identical cosmological results using either our Hydro or DMonly mass functions. The fit by Tinker et al. (2008) leads to slightly lower values of  $\Omega_m$  and  $\sigma_8$ .

- The mass function by Watson et al. (2013) seems to bias results toward  $\Omega_m \sim 0.27$ . This may be due to their parametrization of the redshift evolution of the mass function shape parameters using  $\Omega_m(z)$ , which results in a heightened and likely artificial cosmological sensitivity.
- The baryonic impact is negligible for the *Planck*-like sample, too. However, using our mass function instead of Tinker et al. (2008) shifts the results by  $\Delta(\sigma_8) \simeq 0.05$ . This shift is comparable to the observed difference between the latest *Planck* clusters and CMB constraints; using our mass function should therefore lead to good agreement between the two probes.
- The eROSITA sample extends to lower masses than the SPT and *Planck* catalogues. We observe an offset in the results from Hydro and DMonly, which we identify as the impact of baryons. Neglecting this effect leads to an underestimate of the matter density parameter  $\Delta\Omega_m \simeq -0.01$ .

Part of the differences between the cosmological results recovered using our mass functions and using the Tinker et al. (2008) mass function could be due to different parametrizations of the mass function for  $\Delta_{500c}$ . In Tinker et al. (2008), the mass function is fit for 9 different values in a range of overdensities  $\Delta_{\text{mean}}$  from 200 – 3200. When working with critical overdensities, one must interpolate to the corresponding  $\Delta_{\text{mean}}(z) = \Delta_{\text{crit}}/\Omega_m(z)$ . Therefore, when calculating the mass function for  $\Delta_{500c}$ , one interpolates to mean overdensities from  $\sim 500$  to  $\sim 1700$ , depending on redshift and matter density. As stated previously, there are indications that the mass function is approximately universal only for  $\Delta_{\text{mean}} \sim 200$ . Therefore, it is not clear that the approach chosen for the Tinker et al. (2008) mass function fit would also provide universal mass functions. To avoid this issue, we pursue a different approach in which we propagate the universal properties of the  $\Delta_{200m}$  mass function to the overdensity definition of interest.

More work, both on the theoretical and on the numerical aspects of calibrating the mass function is needed to be able to fully extract the cosmological information from near-future cluster samples. It is important to better understand the cosmological dependencies of the fitting function, and to construct an analytic formula whose universality – or indeed departure from universality – is well understood. Finally, a careful comparison of cluster catalogues generated from different sets of numerical simulations would be helpful to better understand the systematic uncertainties on the mass function.

We acknowledge the support of the DFG Cluster of Excellence “Origin and Structure of the Universe” and the Transregio program TR33 “The Dark Universe”. The calculations have partially been carried out on the computing facilities of the Computational Center for Particle and Astrophysics (C2PAP) and of the Leibniz Supercomputer Center (LRZ) under the project IDs pr83li and pr86re.

## Appendix: Spherical overdensity $\Delta_{200c}$

Applying the method described in Section 5.3.2, we also present the mass function for  $M_{200c}$

$$\frac{dn}{dM_{200c}} = f(\sigma) \frac{\bar{\rho}_m}{M_{200c}} \frac{d \ln \sigma^{-1}}{dM_{200c}} \times \frac{M_{200c}}{M_{200m}}. \quad (5.10)$$

We establish a mass-dependent fit for  $M_{200c}/M_{200m}$

$$\frac{M_{200c}}{M_{200m}} \equiv \gamma + \delta \ln M_{200c}, \quad (5.11)$$

where  $\gamma$  and  $\delta$  depend on  $\Omega_m$  and redshift as

$$\begin{aligned} \gamma(\Omega_m, z) &= \gamma_0 + \gamma_1 \exp\left(-\left(\frac{\gamma_2 - z}{\gamma_3}\right)^2\right) \\ \delta(\Omega_m, z) &= \delta_0 + \delta_1 z \end{aligned} \quad (5.12)$$

and

$$\begin{aligned}
 \gamma_0(\Omega_m) &= 3.54 \times 10^{-2} + \Omega_m^{0.09} \\
 \gamma_1(\Omega_m) &= 4.56 \times 10^{-2} + 2.68 \times 10^{-2}/\Omega_m \\
 \gamma_2(\Omega_m) &= 0.721 + 3.50 \times 10^{-2}/\Omega_m \\
 \gamma_3(\Omega_m) &= 0.628 + 0.164/\Omega_m \\
 \delta_0(\Omega_m) &= -1.67 \times 10^{-2} + 2.18 \times 10^{-2} \Omega_m \\
 \delta_1(\Omega_m) &= 6.52 \times 10^{-3} - 6.86 \times 10^{-3} \Omega_m.
 \end{aligned} \tag{5.13}$$

This fit is accurate at the few percent level in the range  $0 < z < 2$ ,  $10^{13} < M_{200c}/M_\odot < 2 \times 10^{16}$ , and  $0.15 < \Omega_m < 0.5$ .



# Chapter 6

## Final remarks

After having presented the essence of my work conducted over the last few years, I would like to use this last chapter to summarize what we have learned. Within the next years and decades a tremendous amount of multi-wavelength cluster data will be gathered. Exploiting these data in an optimal way will only be possible if we know how these different datasets interact, and how they compare, each with their strengths and weaknesses. This will be a challenging task that comprises both the astrophysical and cosmological aspects of cluster physics. Hopefully, this thesis contributes a set of analysis methods and results to this endeavor.

We will start by summarizing the scientific results presented in this thesis. Then, we summarize the key methodological features we developed and discussed. This summary naturally leads to a set of interesting questions that still remain open, and to interesting analyses that are worth considering in the future.

### 6.1 Summary

We discussed a series of four studies in the area of cluster cosmology. The main scientific results of each analysis are summarized in the following.

- In Chapter 2, we present a cosmological analysis using an SZE-selected galaxy cluster sample from the first 720 deg<sup>2</sup> of SPT-SZ survey data. The sample is combined with follow-up data from X-ray  $Y_X$  and optical spectroscopy  $\sigma_v$ , observations to carry out a calibration of the SPT mass-observable relation. The cosmological fit is performed while simultaneously fitting for the parameters of the mass-observable scaling relations, accounting for cluster selection effects.

We compare the constraints on the normalization of the SZE  $\zeta$ -mass relation we obtain from the X-ray and  $\sigma_v$  calibrations. Both agree at the  $0.6\sigma$  level, which we argue is an important systematic cross-check given the different calibration schemes. Using both calibration datasets jointly leads to modest improvements on the normalization  $A_{\text{SZ}}$  and the combination of cosmological parameters  $\sigma_8(\Omega_m/0.27)^{0.3}$ . We compare our cluster-based results with constraints from CMB anisotropy measurements in the  $\Omega_m$ - $\sigma_8$ -plane. Assuming massless neutrinos, the cluster+ $H_0$ +BBN data differ from constraints from WMAP9 (*Planck*) at the  $1.3\sigma$  ( $1.9\sigma$ ) levels. Changing our baseline assumption to account for one massive neutrino ( $m_\nu = 0.06$  eV) reduces these differences to  $1.0\sigma$  ( $1.5\sigma$ ).

Each data combination prefers a different value of the normalization of the SZE mass-observable relation  $A_{\text{SZ}}$ , which implies different overall cluster mass scales. The calibration from  $Y_X$  leads to masses that are about 44% of the value estimated from the combination with CMB anisotropy data. The calibration from  $\sigma_v$  corresponds to  $\sim 23\%$ . These shifts correspond to  $1.9\sigma$  and  $0.8\sigma$  differences, respectively. We perform a series of cosmological tests and analyze different models. In particular, we allow for a varying dark energy equation of state parameter  $w$  and for a modified growth of cosmic structure parametrized by  $\gamma$ . Our simultaneous constraints on both parameters ( $\gamma = 0.73 \pm 0.28$  and  $w = -1.007 \pm 0.065$  using clusters, CMB anisotropy measurements, BAO, and SNIa) are consistent with the predictions of the standard  $\Lambda$ CDM model.

- In Chapter 3, we cross-match SZE-selected cluster candidates from the full 2500 deg<sup>2</sup> SPT-SZ survey (Bleem et al. 2015) with an optically selected catalog extracted with the redMaPPer algorithm from the DES science verification data DES-SVA1. The overlap between both surveys is 129.1 deg<sup>2</sup>, in which we confirm 25 matches with SPT detection significances  $\xi > 4.5$ .

We present a calibration of the optical richness  $\lambda$ -mass scaling relation using mass estimates derived from the SZE. The SZE mass-observable relation is determined by abundance matching the SPT catalog within a fixed reference cosmology, and the richness-mass calibration is performed simultaneously. We marginalize over the parameters of the SZE-mass relation. The redMaPPer  $\lambda$ -mass relation for SPT-SZ selected clusters has small asymptotic intrinsic scatter  $D = 0.15^{+0.10}_{-0.07}$  and a slope  $B = 1.14^{+0.21}_{-0.18}$ , consistent with unity. Our constraints are in agreement with those of Rykoff et al. (2012).

Interestingly, a consistency test in which we take the large optical sample and evaluate the number of expected SZE matches reveals a mild  $2\sigma$  tension between the optical and SZE data. Future work benefiting from the large region of overlap between the DES and SPT surveys will improve our constraints and allow us to better characterize the optical and SZE properties of both cluster samples.

- In Chapter 4, we use a cluster sample extracted from the full 2500 deg<sup>2</sup> SPT-SZ survey data to constrain the growth of cosmic structure. The SZE-selected catalog contains 377 candidates, of which 82 have additional X-ray  $Y_X$  measurements that are used for mass calibration. The mass calibration and cosmological analysis method closely follows the detailed descriptions in Chapter 2.

First, we consider a flat  $\Lambda$ CDM background cosmology, but describe the growth of structure with a phenomenological parametrization involving the growth index  $\gamma$ . The prediction by GR is  $\gamma_{\text{GR}} = 0.55$ . Our cluster sample, in combination with  $H_0$  and BBN priors, leads to a measurement of  $\gamma = 0.44 \pm 0.13$  which is lower than, but in agreement with, the theoretical expectation. A comparison with constraints from CMB anisotropy data shows good agreement, too. It is worth noting that galaxy clusters provide less degenerate constraints on this model than the CMB. In a final test, we also allow for the dark energy equation of state parameter  $w$  to vary. Using our cluster and BBN+ $H_0$  data combination, we simultaneously constrain  $\gamma = 0.53 \pm 0.15$  and  $w = -1.30 \pm 0.30$ . These measurements show no evidence for tension with the  $\Lambda$ CDM model, although our recovered value for  $w$  is about  $1\sigma$  low.

Our results are tighter than the ones obtained from other cluster samples (e.g., Mantz et al. 2015, who used X-ray selected samples), and this is due to the greater redshift range covered by the SPT sample. We argue that future studies, in which the SPT sample is combined with a low-redshift sample similar to that in the Mantz et al. (2015) analysis will provide tighter and thus even more interesting results.

- In Chapter 5, we use the largest hydrodynamic simulations available to date to calibrate the halo mass function (HMF) accounting for the effects of halo baryons. The simulations and our halo selection are characterized by 1) treatment of the baryonic component and of AGN feedback that correctly reproduces several observations such as cluster pressure profiles (Planck Collaboration et al. 2013; McDonald et al. 2014) and AGN luminosity functions (Hirschmann et al. 2014), 2) simulation boxes of up to  $\sim 2$  Gpc<sup>3</sup> covering large cosmological volumes, and 3) a conservative halo selection with at least  $10^4$  dark matter particles within the considered halo volume, minimizing potential biases related to numerical resolution. Compared to our dark matter-only control simulations, we find that the presence of baryons decreases the cluster masses. Conversely, at fixed mass, the number density of haloes decreases by up to  $\sim 15\%$  for low-mass clusters  $\lesssim \text{few} \times 10^{14} M_\odot$  and at low redshift  $z \lesssim 0.5$ . At higher masses and redshift, the difference vanishes. We establish fitting formulae for different cluster mass definitions. We argue that each mass definition implies a slightly different shape of the fitting function to preserve universality of the fit with respect to redshift and cosmology.

Finally, we use idealized simulated representations of the SPT, *Planck*, and eROSITA cluster surveys to discuss the impact of our HMF fits. We confirm that baryons have a negligible impact for current surveys such as SPT and *Planck*, which essentially probe the high mass end of the cluster population. However, baryonic effects will for sure be important for future surveys such as eROSITA, which will detect clusters down to  $5 \times 10^{13} M_\odot/h$ . In such a survey, neglecting the baryonic effects could lead to

biases on cosmological parameters that are of the same order as the expected overall error budget. More work on both the numerical and theoretical aspects of the HMF is therefore needed to be able to extract all cosmological information from such near-future cluster catalogs.

## 6.2 Discussion and Outlook

In this thesis, besides producing interesting and new cosmological constraints, we develop and implement a range of different analysis methods. They mark a path toward conducting new studies that are less subject to systematic biases with existing or new data.

**Firstly**, we develop a framework for conducting cosmological analyses. While this essentially builds upon existing work, there are still individual contributions that are worth mentioning. The wall clock run time of any cosmological fit is a key measure of the productivity during the time of a project. To start with, it has proven useful to test any code against sets of simulated data that are at least an order of magnitude larger than the real sample to be studied to eliminate statistical noise. Then, in order to get a good sense of the reliability of any result, and to test different modifications of the analysis method, or to consider different data combinations, one ideally wants to run any analysis several times before producing the final, publication-ready results. Therefore, since the beginning of my PhD project, we have used state-of-the-art, efficient likelihood sampling algorithms. The obvious downside of this approach is that we cannot not take advantage of existing common samplers. However, we believe that the gain in computational efficiency is worth the additional time invested in implementing faster, parallel algorithms. Finally, there is also some benefit in better understanding the employed techniques and getting familiar with some of their technical aspects.

**Secondly**, we gain a lot of experience with multi-wavelength mass calibration of galaxy clusters. In a first stage, we design a framework that allows us to jointly use two or more follow-up mass measurement techniques, while properly accounting for selection effects. Then, while implementing this method, we keep an eye on the numerical execution speed. For the latest project, we expand our mass calibration method to allow for correlated scatter among different observables. By now, we have successfully worked on SZE data from SPT, X-ray  $Y_X$ , galaxy velocity dispersions, and optical richnesses. In ongoing projects, we expand these methods to also implement mass calibration from weak gravitational lensing (e.g., Dietrich, Bocquet, et al. in prep.; Gangkofner, Bocquet, et al. in prep.).

**Thirdly**, we use the cluster data in a cosmological context. Besides constraining common extensions beyond  $\Lambda$ CDM such as  $w$ CDM or allowing for varying neutrino masses, we also investigate possible departures from the growth rate of structure as predicted by General Relativity. While our results show no evidence of a departure from the fiducial model, this kind of test will be crucial as cosmological cluster datasets improve in quality.

**Fourthly**, we work on the modeling of the HMF using large cosmological hydrodynamic simulations. This project stands out as being a little different because it focuses on a more theoretical aspect of cluster cosmology. We argue that the functional form of the fitting function depends on the choice of cluster mass definition and provide fitting functions for some common definitions. Applying our fitting function to simulated cluster survey data, we show that current cluster samples are basically not affected by baryonic effects on the HMF, simply because the mass threshold is typically quite large. However, samples that will be available in the near future could very well be significantly affected, and neglecting halo baryons could then lead to significantly biased cosmological constraints.

By the end of this thesis, we have come up with a very powerful and flexible set of cosmological analysis methods and tools. These can be applied to existing data to conduct other very interesting multi-wavelength mass calibration and cross-calibration studies. In particular, our experience on SPT data allows for a lot of science cases given the overlap with the optical Dark Energy Survey (DES). For example, we are actively working on constraining cluster masses through weak gravitational lensing of SPT clusters using DES. These mass measurements can then be used to constrain the SPT mass-observable relation (Gangkofner, Bocquet, et al., in prep.). This will ultimately allow for tight and robust cosmological constraints. While the DES survey

data increases, a more detailed joint analysis of the SPT  $\xi$ -mass and the DES richness-mass relations can be performed (Saro et al., in prep.). Besides producing scientific results on existing data, our framework can also be used to help design upcoming or future cluster surveys as eROSITA or Euclid. Because mass calibration is the most important systematic limit, it is crucial to quantify the specific needs for follow-up campaigns well in advance.

Given the effort to obtain high-quality survey and mass calibration data, it is also important to continue developing phenomenological tests of the cosmological model that can be challenged by the data. In this thesis, we have considered various extensions of the standard flat  $\Lambda$ CDM model and argued that clusters are uniquely sensitive to some of these extensions. It is of primary importance to continue pushing in this direction to fully exploit the huge potential of current and future cluster data.

The future of cluster cosmology is bright, with several high-quality surveys being conducted or coming up. It is our task to continue improving analysis methods, understand the data, and design the framework to exploit the full power of these data sets. I am looking forward to seeing the field evolve and working on solving the challenges that we will have to face!

# Bibliography

- Abell, G. O. 1958, ApJS, 3, 211
- Aihara, H., et al. 2011, ApJS, 193, 29
- Allen, S. W., Evrard, A. E., & Mantz, A. B. 2011, ARA&A, 49, 409
- Anderson, L., et al. 2012, MNRAS, 427, 3435
- Andersson, K., et al. 2011, ApJ, 738, 48
- . 2010, submitted to apj, arXiv:1006.3068
- Andreon, S., & Congdon, P. 2014, A&A, 568, A23
- Angulo, R. E., Springel, V., White, S. D. M., Jenkins, A., Baugh, C. M., & Frenk, C. S. 2012, MNRAS, 426, 2046
- Annis, J., et al. 2014, ApJ, 794, 120
- Appenzeller, I., et al. 1998, The Messenger, 94, 1
- Applegate, D. E., et al. 2014, MNRAS, 439, 48
- Ascaso, B., Wittman, D., & Dawson, W. 2014, MNRAS, 439, 1980
- Banerji, M., et al. 2015, MNRAS, 446, 2523
- Barbosa, D., Bartlett, J., Blanchard, A., & Oukbir, J. 1996, A&A, 314, 13
- Barrena, R., Biviano, A., Ramella, M., Falco, E. E., & Seitz, S. 2002, A&A, 386, 816
- Bartlett, J. G., & Silk, J. 1994, ApJ, 423, 12
- Battye, R. A., & Weller, J. 2003, Phys. Rev. D, 68, 083506
- Becker, M. R., & Kravtsov, A. V. 2011, ApJ, 740, 25
- Benson, B. A., et al. 2013, ApJ, 763, 147
- Beutler, F., et al. 2011, MNRAS, 416, 3017
- Bhattacharya, S., Heitmann, K., White, M., Lukić, Z., Wagner, C., & Habib, S. 2011, ApJ, 732, 122
- Biesiadzinski, T., McMahon, J. J., Miller, C. J., Nord, B., & Shaw, L. 2012, ArXiv e-prints, 1201.1282
- Biviano, A., Murante, G., Borgani, S., Diaferio, A., Dolag, K., & Girardi, M. 2006, A&A, 456, 23
- Bleem, L. E., Stalder, B., Brodwin, M., Busha, M. T., Gladders, M. D., High, F. W., Rest, A., & Wechsler, R. H. 2014, ArXiv e-prints, 1403.7186
- Bleem, L. E., et al. 2015, ApJS, 216, 27
- Bocquet, S., Saro, A., Dolag, K., & Mohr, J. J. 2015a, ArXiv e-prints, 1502.07357

- Bocquet, S., et al. 2015b, ApJ, 799, 214
- Böhringer, H., et al. 2000, ApJS, 129, 435
- Borgani, S., et al. 2004, MNRAS, 348, 1078
- . 2001, ApJ, 561, 13
- Borm, K., Reiprich, T. H., Mohammed, I., & Lovisari, L. 2014, A&A, 567, A65
- Buckley-Geer, E. J., et al. 2011, ApJ, 742, 48
- Carlstrom, J. E., et al. 2011, PASP, 123, 568
- Carlstrom, J. E., Holder, G. P., & Reese, E. D. 2002, ARA&A, 40, 643
- Cash, W. 1979, ApJ, 228, 939
- Cavaliere, A., & Fusco-Femiano, R. 1976, A&A, 49, 137
- Cayón, L., Gordon, C., & Silk, J. 2011, MNRAS, 415, 849
- Costanzi, M., Villaescusa-Navarro, F., Viel, M., Xia, J.-Q., Borgani, S., Castorina, E., & Sefusatti, E. 2013, J. Cosmology Astropart. Phys., 12, 12
- Courtin, J., Rasera, Y., Alimi, J.-M., Corasaniti, P.-S., Boucher, V., & Füzfa, A. 2011, MNRAS, 410, 1911
- Crawford, T. M., Switzer, E. R., Holzapfel, W. L., Reichardt, C. L., Marrone, D. P., & Vieira, J. D. 2010, ApJ, 718, 513
- Crocce, M., Fosalba, P., Castander, F. J., & Gaztañaga, E. 2010, MNRAS, 403, 1353
- Cui, W., Borgani, S., Dolag, K., Murante, G., & Tornatore, L. 2012, MNRAS, 423, 2279
- Cui, W., Borgani, S., & Murante, G. 2014, MNRAS, 441, 1769
- Cusworth, S. J., Kay, S. T., Battye, R. A., & Thomas, P. A. 2014, MNRAS, 439, 2485
- Dalal, N., Doré, O., Huterer, D., & Shirokov, A. 2008, Phys. Rev. D, 77, 123514
- Davis, M., Efstathiou, G., Frenk, C. S., & White, S. D. M. 1985, ApJ, 292, 371
- de Jong, J. T. A., Verdoes Kleijn, G. A., Kuijken, K. H., & Valentijn, E. A. 2013, Experimental Astronomy, 35, 25
- De Lucia, G., & Blaizot, J. 2007, MNRAS, 375, 2
- Dehnen, W., & Aly, H. 2012, MNRAS, 425, 1068
- Desai, S., et al. 2012, ApJ, 757, 83
- Di Matteo, T., Colberg, J., Springel, V., Hernquist, L., & Sijacki, D. 2008, ApJ, 676, 33
- Diehl, T., & For Dark Energy Survey Collaboration. 2012, Physics Procedia, 37, 1332
- Dolag, K., Borgani, S., Murante, G., & Springel, V. 2009, MNRAS, 399, 497
- Dolag, K., Jubelgas, M., Springel, V., Borgani, S., & Rasia, E. 2004, ApJ, 606, L97
- Dolag, K., Vazza, F., Brunetti, G., & Tormen, G. 2005, MNRAS, 364, 753

- Donnert, J., Dolag, K., Brunetti, G., & Cassano, R. 2013, MNRAS, 429, 3564
- Duffy, A. R., Schaye, J., Kay, S. T., & Dalla Vecchia, C. 2008, MNRAS, 390, L64
- Eadie, W. T., & Frederick, J. 1983, Statistical Methods in Experimental Physics (Elsevier Science Ltd.)
- Eisenhardt, P. R. M., et al. 2008, ApJ, 684, 905
- Eisenstein, D. J., & Hu, W. 1998, ApJ, 496, 605
- . 1999, ApJ, 511, 5
- Eke, V. R., Cole, S., Frenk, C. S., & Patrick Henry, J. 1998, MNRAS, 298, 1145
- Evrard, A. E., Arnault, P., Huterer, D., & Farahi, A. 2014, MNRAS, 441, 3562
- Evrard, A. E., et al. 2008, ApJ, 672, 122
- Fabian, A. C. 2010, in IAU Symposium, Vol. 267, IAU Symposium, ed. B. M. Peterson, R. S. Somerville, & T. Storchi-Bergmann, 341–349
- Faltenbacher, A., & Diemand, J. 2006, MNRAS, 369, 1698
- Ferland, G. J., Korista, K. T., Verner, D. A., Ferguson, J. W., Kingdon, J. B., & Verner, E. M. 1998, PASP, 110, 761
- Flaughher, B., et al. 2015, ArXiv e-prints, 1504.02900
- Flaughher, B. L., et al. 2012, in Society of Photo-Optical Instrumentation Engineers (SPIE) Conference Series, Vol. 8446, Society of Photo-Optical Instrumentation Engineers (SPIE) Conference Series, 11
- Foley, R. J., et al. 2011, ApJ, 731, 86
- Foreman-Mackey, D., Hogg, D. W., Lang, D., & Goodman, J. 2013, PASP, 125, 306
- Fowler, J. W., et al. 2007, Appl. Opt., 46, 3444
- Gifford, D., Miller, C., & Kern, N. 2013, ApJ, 773, 116
- Gioia, I. M., Maccacaro, T., Schild, R. E., Wolter, A., Stocke, J. T., Morris, S. L., & Henry, J. P. 1990, ApJS, 72, 567
- Gladders, M. D., & Yee, H. K. C. 2000, AJ, 120, 2148
- Gonzalez-Garcia, M. C., Maltoni, M., Salvado, J., & Schwetz, T. 2012, Journal of High Energy Physics, 12, 123
- Haardt, F., & Madau, P. 2001, in Clusters of Galaxies and the High Redshift Universe Observed in X-rays, ed. D. M. Neumann & J. T. V. Tran, 64
- Haehnelt, M. G., & Tegmark, M. 1996, MNRAS, 279, 545+
- Haiman, Z., Mohr, J. J., & Holder, G. P. 2001, ApJ, 553, 545
- Hao, J., et al. 2010, ApJS, 191, 254
- Hasselfield, M., et al. 2013, J. Cosmology Astropart. Phys., 7, 8
- Henry, J. P., & Arnaud, K. A. 1991, ApJ, 372, 410

- High, F. W., et al. 2012, ArXiv e-prints, 1205.3103
- Hinshaw, G., et al. 2013, ApJS, 208, 19
- Hirschmann, M., Dolag, K., Saro, A., Bachmann, L., Borgani, S., & Burkert, A. 2014, MNRAS, 442, 2304
- Hoekstra, H. 2007, MNRAS, 379, 317
- Hoekstra, H., Herbonnet, R., Muzzin, A., Babul, A., Mahdavi, A., Viola, M., & Cacciato, M. 2015, MNRAS, 449, 685
- Hogg, D. W. 1999, ArXiv Astrophysics e-prints
- Holder, G., Haiman, Z., & Mohr, J. J. 2001, ApJ, 560, L111
- Jenkins, A., Frenk, C. S., White, S. D. M., Colberg, J. M., Cole, S., Evrard, A. E., Couchman, H. M. P., & Yoshida, N. 2001, MNRAS, 321, 372
- Keisler, R., et al. 2011, ApJ, 743, 28
- Kilbinger, M., et al. 2011, ArXiv e-prints, 1101.0950
- Kirkman, D., Tytler, D., Suzuki, N., O'Meara, J. M., & Lubin, D. 2003, ApJS, 149, 1
- Koester, B. P., et al. 2007, ApJ, 660, 239
- Komatsu, E., et al. 2009, ApJS, 180, 330
- . 2011, ApJS, 192, 18
- Kravtsov, A. V., Vikhlinin, A., & Nagai, D. 2006, ApJ, 650, 128
- Lauer, T. R., Postman, M., Strauss, M. A., Graves, G. J., & Chisari, N. E. 2014, ApJ, 797, 82
- Laureijs, R., et al. 2011, ArXiv e-prints, 1110.3193
- Le Brun, A. M. C., McCarthy, I. G., Schaye, J., & Ponman, T. J. 2014, MNRAS, 441, 1270
- Lewis, A., Challinor, A., & Lasenby, A. 2000, ApJ, 538, 473
- Lima, M., & Hu, W. 2005, Phys. Rev. D, 72, 043006
- . 2007, Phys. Rev. D, 76, 123013
- Lin, Y., Mohr, J. J., & Stanford, S. A. 2004, ApJ, 610, 745
- Liu, J., et al. 2015, MNRAS, 448, 2085
- LSST Dark Energy Science Collaboration. 2012, ArXiv e-prints, 1211.0310
- Lukić, Z., Heitmann, K., Habib, S., Bashinsky, S., & Ricker, P. M. 2007, ApJ, 671, 1160
- Lyons, L. 1989, Statistics for Nuclear and Particle Physicists (Cambridge University Press)
- Lyth, D. H., & Liddle, A. R. 2009, The Primordial Density Perturbation (Cambridge University Press)
- Mantz, A., Allen, S. W., Ebeling, H., Rapetti, D., & Drlica-Wagner, A. 2010a, MNRAS, 406, 1773
- Mantz, A., Allen, S. W., Rapetti, D., & Ebeling, H. 2010b, MNRAS, 406, 1759

- Mantz, A. B., et al. 2015, MNRAS, 446, 2205
- Martizzi, D., Mohammed, I., Teyssier, R., & Moore, B. 2014, MNRAS, 440, 2290
- McDonald, M., et al. 2014, ApJ, 794, 67
- . 2013, ApJ, 774, 23
- Mei, S., et al. 2009, ApJ, 690, 42
- Melchior, P., et al. 2014, ArXiv e-prints, 1405.4285
- Melin, J.-B., Bartlett, J. G., & Delabrouille, J. 2006, A&A, 459, 341
- Menanteau, F., et al. 2010, ApJS, 191, 340
- Merloni, A., et al. 2012, ArXiv e-prints, 1209.3114
- Meszaros, P. 1974, A&A, 37, 225
- Mohr, J. J., et al. 2008, in Society of Photo-Optical Instrumentation Engineers (SPIE) Conference Series, Vol. 7016, Society of Photo-Optical Instrumentation Engineers (SPIE) Conference Series
- Mohr, J. J., et al. 2012, in Society of Photo-Optical Instrumentation Engineers (SPIE) Conference Series, Vol. 8451, Society of Photo-Optical Instrumentation Engineers (SPIE) Conference Series, 0
- Molnar, S. M., Haiman, Z., Birkinshaw, M., & Mushotzky, R. F. 2004, ApJ, 601, 22
- Motl, P. M., Hallman, E. J., Burns, J. O., & Norman, M. L. 2005, apjl, 623, L63
- Munari, E., Biviano, A., Borgani, S., Murante, G., & Fabjan, D. 2013, Mon.Not.Roy.Astron.Soc., 430, 2638
- Muzzin, A., et al. 2012, ApJ, 746, 188
- Nagai, D., Kravtsov, A. V., & Vikhlinin, A. 2007, ApJ, 668, 1
- Navarro, J. F., Frenk, C. S., & White, S. D. M. 1997, ApJ, 490, 493
- Ngeow, C., et al. 2006, in Society of Photo-Optical Instrumentation Engineers (SPIE) Conference Series, Vol. 6270, Society of Photo-Optical Instrumentation Engineers (SPIE) Conference Series
- Nurgaliev, D., McDonald, M., Benson, B. A., Miller, E. D., Stubbs, C. W., & Vikhlinin, A. 2013, ApJ, 779, 112
- Pacaud, F., et al. 2007, MNRAS, 382, 1289
- Padmanabhan, N., Xu, X., Eisenstein, D. J., Scalzo, R., Cuesta, A. J., Mehta, K. T., & Kazin, E. 2012, MNRAS, 427, 2132
- Park, C.-G., Hwang, J.-c., & Noh, H. 2012, Phys. Rev. D, 86, 083535
- Peebles, P. 1980, The Large Scale Structure of the Universe (Princeton: Princeton University Press)
- Percival, W. J., et al. 2010, MNRAS, 401, 2148
- Perlmutter, S., et al. 1999, ApJ, 517, 565
- Pillepich, A., Porciani, C., & Reiprich, T. H. 2012, MNRAS, 422, 44

- Planck Collaboration, et al. 2011, A&A, 536, A13  
———. 2014a, A&A, 571, A15  
———. 2014b, A&A, 571, A16  
———. 2014c, A&A, 571, A20  
———. 2013, A&A, 550, A131  
———. 2015a, ArXiv e-prints, 1502.01589  
———. 2015b, ArXiv e-prints, 1502.01597
- Predehl, P., et al. 2014, in Society of Photo-Optical Instrumentation Engineers (SPIE) Conference Series, Vol. 9144, Society of Photo-Optical Instrumentation Engineers (SPIE) Conference Series, 1
- Press, W., & Schechter, P. 1974, ApJ, 187, 425
- Press, W. H., Teukolsky, S. A., Vetterling, W. T., & Flannery, B. P. 1992, Numerical recipes in C. The art of scientific computing (Cambridge: University Press, —c1992, 2nd ed.)
- Rapetti, D., Allen, S. W., Mantz, A., & Ebeling, H. 2010, MNRAS, 406, 1796
- Rapetti, D., Blake, C., Allen, S. W., Mantz, A., Parkinson, D., & Beutler, F. 2013, MNRAS, 432, 973
- Reed, D., Gardner, J., Quinn, T., Stadel, J., Fardal, M., Lake, G., & Governato, F. 2003, MNRAS, 346, 565
- Reed, D. S., Bower, R., Frenk, C. S., Jenkins, A., & Theuns, T. 2007, MNRAS, 374, 2
- Reichardt, C. L., et al. 2013, ApJ, 763, 127
- Riess, A. G., et al. 1998, AJ, 116, 1009
- Riess, A. G., et al. 2011, ApJ, 730, 119
- Rozo, E., Bartlett, J. G., Evrard, A. E., & Rykoff, E. S. 2014a, MNRAS, 438, 78
- Rozo, E., Evrard, A. E., Rykoff, E. S., & Bartlett, J. G. 2014b, MNRAS, 438, 62
- Rozo, E., & Rykoff, E. S. 2014, ApJ, 783, 80
- Rozo, E., Rykoff, E. S., Bartlett, J. G., & Melin, J. B. 2014c, ArXiv e-prints, 1401.7716
- Rozo, E., et al. 2010, ApJ, 708, 645
- Rozo et al. 2015, In Preparation
- Ruel, J., et al. 2014, ApJ, 792, 45
- Rykoff, E. S., et al. 2012, ApJ, 746, 178  
———. 2014, ApJ, 785, 104
- Rykoff et al. 2015, In Preparation
- Sánchez, C., et al. 2014, MNRAS, 445, 1482
- Saro, A., et al. 2014, MNRAS, 440, 2610

- Saro, A., Mohr, J. J., Bazin, G., & Dolag, K. 2013, ApJ, 772, 47
- Schaffer, K. K., et al. 2011, ApJ, 743, 90
- Schaller, M., et al. 2014, ArXiv e-prints, 1409.8617
- Schellenberger, G., Reiprich, T. H., Lovisari, L., Nevalainen, J., & David, L. 2014, ArXiv e-prints, 1404.7130
- Sehgal, N., et al. 2013, ApJ, 767, 38
- . 2011, ApJ, 732, 44
- Sheth, R. K., Mo, H. J., & Tormen, G. 2001, MNRAS, 323, 1
- Sifón, C., et al. 2013, ApJ, 772, 25
- Soares-Santos, M., et al. 2011, ApJ, 727, 45
- Song, J., et al. 2012a, ApJ, 761, 22
- . 2012b, ApJ, 761, 22
- Springel, V. 2005, MNRAS, 364, 1105
- Springel, V., & Hernquist, L. 2002, MNRAS, 333, 649
- . 2003, MNRAS, 339, 289
- Springel, V., et al. 2005, Nature, 435, 629
- Springel, V., White, S. D. M., Tormen, G., & Kauffmann, G. 2001, MNRAS, 328, 726
- Stanek, R., Rasia, E., Evrard, A. E., Pearce, F., & Gazzola, L. 2010, ApJ, 715, 1508
- Staniszewski, Z., et al. 2009, ApJ, 701, 32
- Story, K., et al. 2011, ApJ, 735, L36
- Sullivan, M., et al. 2011, ApJ, 737, 102
- Sun, M., Voit, G. M., Donahue, M., Jones, C., Forman, W., & Vikhlinin, A. 2009, ApJ, 693, 1142
- Sunyaev, R. A., & Zel'dovich, Y. B. 1972, Comments on Astrophysics and Space Physics, 4, 173
- Suzuki, N., et al. 2012, ApJ, 746, 85
- Tauber, J. A., et al. 2010, A&A, 520, A1
- The Dark Energy Survey Collaboration. 2005, ArXiv Astrophysics e-prints
- Tinker, J., Kravtsov, A. V., Klypin, A., Abazajian, K., Warren, M., Yepes, G., Gottlöber, S., & Holz, D. E. 2008, ApJ, 688, 709
- Tornatore, L., Borgani, S., Dolag, K., & Matteucci, F. 2007, MNRAS, 382, 1050
- Šuhada, R., et al. 2012, A&A, 537, A39
- Vanderlinde, K., et al. 2010, ApJ, 722, 1180

- Velliscig, M., van Daalen, M. P., Schaye, J., McCarthy, I. G., Cacciato, M., Le Brun, A. M. C., & Dalla Vecchia, C. 2014, MNRAS, 442, 2641
- Viana, P., & Liddle, A. 1999, MNRAS, 303, 535
- Vikhlinin, A., et al. 2009a, ApJ, 692, 1033
- . 2009b, ApJ, 692, 1060
- Vikhlinin, A., McNamara, B. R., Forman, W., Jones, C., Quintana, H., & Hornstrup, A. 1998, ApJ, 502, 558
- Vogelsberger, M., et al. 2014, MNRAS, 444, 1518
- Wang, L., & Steinhardt, P. J. 1998, ApJ, 508, 483
- Wang, S., Khouri, J., Haiman, Z., & May, M. 2004, Phys. Rev. D, 70, 123008
- Warren, M. S., Abazajian, K., Holz, D. E., & Teodoro, L. 2006, ApJ, 646, 881
- Watson, W. A., Iliev, I. T., D'Aloisio, A., Knebe, A., Shapiro, P. R., & Yepes, G. 2013, MNRAS, 433, 1230
- Weinberg, D. H., Mortonson, M. J., Eisenstein, D. J., Hirata, C., Riess, A. G., & Rozo, E. 2013, Phys. Rep., 530, 87
- Wen, Z. L., Han, J. L., & Liu, F. S. 2012, ApJS, 199, 34
- White, M., Cohn, J. D., & Smit, R. 2010, MNRAS, 408, 1818
- White, M., Hernquist, L., & Springel, V. 2002, ApJ, 579, 16
- White, S. D. M., Efstathiou, G., & Frenk, C. S. 1993, MNRAS, 262, 1023
- Wiersma, R. P. C., Schaye, J., & Smith, B. D. 2009, MNRAS, 393, 99
- Wiesner, M. P., Lin, H., & Soares-Santos, M. 2015, ArXiv e-prints, 1501.06893
- Williamson, R., et al. 2011, ApJ, 738, 139
- Wraith, D., Kilbinger, M., Benabed, K., Cappe, O., Cardoso, J.-F., et al. 2009, Phys.Rev., D80, 023507
- Wu, H.-Y., Hahn, O., Evrard, A. E., Wechsler, R. H., & Dolag, K. 2013, MNRAS, 436, 460
- Zenteno, A., et al. 2011, ApJ, 734, 3
- Zwicky, F., Herzog, E., & Wild, P. 1968, Catalogue of galaxies and of clusters of galaxies

# List of scientific publications and talks

## First author articles

- **S. Bocquet**, A. Saro, K. Dolag, J. Mohr, “Baryon impact on the halo mass function: Fitting formulae and implications for cluster cosmology”, 2015, *MNRAS* (submitted, arXiv:1502.07357)
- **S. Bocquet** et al., “Mass Calibration and Cosmological Analysis of the SPT-SZ Galaxy Cluster Sample Using Velocity Dispersion  $\sigma_v$  and X-ray  $Y_X$  Measurements”, 2015, *ApJ*, 799, 214

## Articles in preparation

- **S. Bocquet** and the South Pole Telescope collaboration, “The Growth of Cosmic Structure Measured with Galaxy Clusters in the South Pole Telescope SPT-SZ Survey”, in prep.
- A. Saro, **S. Bocquet**, et al., “The richness-mass relation and optical-SZE positional offsets for SPT selected clusters”, in prep.
- J. Dietrich, **S. Bocquet**, et al., “Weak lensing measurements of galaxy clusters in the South Pole Telescope survey, and robust X-ray scaling relations”, in prep.
- C. Gangkofner, **S. Bocquet**, et al., “Calibration of the SPT mass-observable relation through weak lensing data from the Dark Energy Survey”, in prep.

## Published co-authored articles

- E. J. Baxter, R. Keisler, S. Dodelson, et al. (including **S. Bocquet**); “A Measurement of Gravitational Lensing of the Cosmic Microwave Background by Galaxy Clusters Using Data from the South Pole Telescope”, 2014, *ApJ* (accepted for publication, arXiv:1412.7521)
- J. Liu, J. Mohr, A. Saro, et al. (including **S. Bocquet**), “Analysis of Sunyaev-Zel’dovich effect mass-observable relations using South Pole Telescope observations of an X-ray selected sample of low mass galaxy clusters and groups”, 2015, *MNRAS*, 448, 2085
- L. Bleem, B. Stalder, T. de Haan, et al. (including **S. Bocquet**), “Galaxy Clusters Discovered via the Sunyaev-Zel’dovich Effect in the 2500-square-degree SPT-SZ Survey”, 2015, *ApJS*, 216, 27
- B. Saliwanchik, T. Montroy, et al. (including **S. Bocquet**), “Measurement of Galaxy Cluster Integrated Comptonization and Mass Scaling Relations with the South Pole Telescope”, 2015, *ApJ*, 799, 137
- M. McDonald, B. Benson, A. Vikhlinin, et al. (including **S. Bocquet**), “The Redshift Evolution of the Mean Temperature, Pressure, and Entropy Profiles in 80 SPT-Selected Galaxy Clusters”, 2014, *ApJ*, 794, 67
- M. Bayliss, M. Ashby, J. Ruel, M. Brodwin, et al. (including **S. Bocquet**), “SPT-CL J2040-4451: An SZ-Selected Galaxy Cluster at  $z = 1.478$  With Significant Ongoing Star Formation”, 2014, *ApJ*, 794, 12
- J. Ruel et al. (including **S. Bocquet**), “Optical Spectroscopy and Velocity Dispersions of Galaxy Clusters from the SPT-SZ Survey”, 2014, *ApJ*, 792, 45

- A. Saro, J. Liu, J. Mohr, et al. (including **S. Bocquet**), “Constraints on the CMB Temperature Evolution using Multi-Band Measurements of the Sunyaev-Zel’dovich Effect with the South Pole Telescope”, 2014, *MNRAS*, 440, 2610
- M. McDonald et al. (including **S. Bocquet**), “The Growth of Cool Cores and Evolution of Cooling Properties in a Sample of 83 Galaxy Clusters at  $0.3 < z < 1.2$  Selected from the SPT-SZ Survey”, 2013, *ApJ*, 774, 23
- D. Semler et al. (including **S. Bocquet**), “High-Redshift Cool-Core Galaxy Clusters Detected via the Sunyaev-Zel’dovich Effect in the South Pole Telescope Survey”, 2012, *ApJ*, 761, 183

#### Submitted co-authored articles

- I. Chiu, J. Mohr, M. McDonald, **S. Bocquet**, et al. “Baryon content of massive galaxy clusters ( $0.57 < z < 1.33$ )”, 2014, *MNRAS* (submitted, arXiv:1412.7823)
- J. Hlavacek-Larrondo, M. McDonald, B. Benson, et al. (including **S. Bocquet**); “X-ray cavities in a sample of 83 SPT-selected clusters of galaxies: Tracing the evolution of AGN feedback in clusters of galaxies out to  $z = 1.2$ ”, 2014, *ApJ* (submitted, arXiv:1410.0025)

#### Talks at conferences and workshops

- Mar 2015: SnowCluster 2015, Snowbird Utah, “Baryon impact on the halo mass function and implications for cluster cosmology”
- Mar 2015: eROSITA cluster working group meeting, Bonn, “Baryon impact on the halo mass function and cosmological implications for eROSITA”
- Feb 2015: MPA high energy seminar, Garching, “Galaxy cluster cosmology with the South Pole Telescope” and “Baryon impact on the halo mass function”
- Feb 2015: MPE OPINAS seminar, Garching, “Galaxy cluster cosmology with SPT” and “Baryon impact on the halo mass function”
- Nov 2014: Cosmology with galaxy clusters in the XXI century, Madrid, “Galaxy cluster cosmology with SPT: Mass calibration from velocity dispersions  $\sigma_v$  and X-ray  $Y_X$ ”
- Oct 2014: SPT collaboration meeting, Chicago, “Weak lensing mass calibration”
- Sept 2014: eROSITA consortium meeting, Potsdam, “Weak lensing calibration of X-ray scaling relations within SPT and prospects for eROSITA”
- Mar 2014: eROSITA cluster working group meeting, Munich, “Comments on galaxy cluster cosmology with SPT”
- Oct 2013: Return of de Sitter II, Garching, “Galaxy cluster cosmology with SPT: Mass calibration from velocity dispersion  $\sigma_v$  and X-ray  $Y_X$ ”
- July 2013: SPT collaboration meeting, Chicago, “Cluster mass calibration”
- July 2013: LMU cosmology seminar, “The cluster mass function”
- June 2013: Excellence cluster science week, Garching, “Galaxy cluster cosmology with SPT”
- June 2013: eROSITA cluster working group meeting, Bonn, “Galaxy cluster cosmology and mass calibration”
- Feb 2013: Workshop on galaxy clusters, Munich, “Galaxy cluster cosmology with SPT”

# Acknowledgments

I would like to thank my supervisor Joe Mohr. You invited me to your research group even though I did not have any experience in astronomy or computing, and patiently gave me the time I needed to learn how things work. You have trusted me and gave me a lot of freedom, but you were always there to defend our projects. You have made it possible to travel to countless conferences and collaboration meetings, and you gave me great opportunities to give talks and present my work. Thank you for giving me the opportunity to discover our exciting research field and thank you for all your support!

Then, I wish to thank everybody who I met in the group throughout the years: Alex, Alfredo, Charitarth, Christina, Clio, Corvin, Gurvan, I-Non, Jiayi, Jörg, Kerstin, Martin, Maurilio, Nikhel, Raffaella, Robert, Shantanu, and Veronica. It was a real pleasure to work, discuss, travel, suffer, have coffee or beer or lunch or dinner, debug code, laugh, cry, publish papers, discuss physics in hot tubs, (did I forget anything?) with you. My special gratitude goes to Alex, with whom I closely worked for every paper presented here. Thanks to everyone for all your support; I would not have achieved any of my research without you!

Then of course there is everybody else at USM I wish to thank, in particular: Klaus, for your cooperation for the mass function paper, Uta, for all your help with administrative challenges and nice chats, Alex (A.), Judith, Luiz, Phil, Rhea, and Wolfi who I also shared the office with, Alex (B.) and Ralf for unforgettable table soccer games (before things got serious), Barbara for chatting about climbing, Alex (B.) for everything including .tex files (guess which ones), the USM choir, the cookie monster, and everybody else who I might have forgotten to mention.

Finally, I thank my friends, my family, and my wonderful girlfriend for the love, help, and support during all these years at university. It's not over yet!